STARS

Electronic Theses and Dissertations, 2020-

2023

High-Dynamic-Range and High-Efficiency Near-Eye Display Systems

En-Lin Hsiang
University of Central Florida

Showcase of Text, Archives, Research & Scholarship

HIGH-DYNAMIC-RANGE AND HIGH-EFFICIENCY NEAR-EYE DISPLAY SYSTEMS

by

EN-LIN HSIANG
B.S. National Chiao Tung University, 2014
M.S. National Chiao Tung University, 2016

A dissertation submitted in partial fulfillment of the requirements
for the degree of Doctor of Philosophy
in the College of Optics and Photonics
at the University of Central Florida
Orlando, Florida

Spring Term
2023

Major Professor: Shin-Tson Wu

ABSTRACT

Near-eye display systems, which project digital information directly into the human visual system, are expected to revolutionize the interface between digital information and physical world. However, the image quality of most near-eye displays is still far inferior to that of direct-view displays. Both light engine and imaging optics of near-eye display systems play important roles to the degraded image quality. In addition, near-eye displays also suffer from a relatively low optical efficiency, which severely limits the device operation time. Such an efficiency loss originates from both light engines and projection processes. This dissertation is devoted to addressing these two critical issues from the entire system perspective.

In Chapter 2, we propose useful design guidelines for the miniature light-emitting diode (mLED) backlit liquid crystal displays (LCDs) to mitigate halo artifacts. After developing a high dynamic range (HDR) light engine in Chapter 3, we establish a systematic image quality evaluation model for virtual reality (VR) devices and analyze the requirements for light engines. Our guidelines for mLED backlit LCDs have been widely practiced in direct-view displays. Similarly, the newly established criteria for light engines will shed new light to guide future VR display development.

To improve the optical efficiency of near eye displays, we must optimize each component. For the light engine, we focus on color-converted micro-LED microdisplays. We fabricate a pixelated cholesteric liquid crystal film on top of a pixelated QD array to recycle the leaked blue light, which in turn doubles the optical efficiency and widens the color gamut. In Chapter 5, we tailor the radiation pattern of the light engine to match the etendue of the imaging systems, as a result, the power loss in the projection process is greatly reduced. The system efficiency is

enhanced by over one-third for both organic light-emitting diode (OLED) displays and LCDs while maintaining indistinguishable image nonuniformity. In Chapter 6, we briefly summarize our major accomplishments.

To my beloved family.

ACKNOWLEDGEMENTS

First of all, I would like to thank my thesis advisor, Dr. Shin-Tson Wu, for his encouragement, enlightened guidance and meticulous care. He always encouraged me to do research that had broad, profound, and lasting impact to the world. His vision and experience led me to a worthy topic and direction. He has been my most trusted source of support in pursuing my research goals. He will be my lifelong friend and best role model, both as a scientist and as a teacher. In addition, I would also like to thank Prof. Wu's better half, Cho-Yan Hiseh, for her love and care over the past five years. She is a loving mother in our extended family. I feel so blessed to be a part of this family.

I would like to thank my committee members, Dr. M. G. Moharam, Dr. Patrick L. LiKamWa, and Dr. Yajie Dong. They were very kind in advising and supervising me during my candidacy, proposal, and dissertation preparation. Also, they became my support, writing recommendation letters when I applied society awards, scholarships, and jobs.

My lab partners and collaborators are my great treasures. We work together day and night to solve many problems in our research. Without their selfless help, I would not have been able to complete my doctoral program. Here, I would like to thank past and present team members, especially Dr. Yun-Han Lee, Dr. Guanjun Tan, Dr. Juan He, Dr. Yuge Huang, Dr. Md Javed Rouf Talukder, Dr. Fangwang Gou, Dr. Tao Zhan, Dr. Ziqian He, Dr. Jianghao Xiong, Dr. Kun Yin, Junyu Zou, Yannanqi Li, Qian Yang, Zhiyong Yang, Zhenyi Luo, Yizhou Qian, Yuqiang Ding, John Semmen, Jason Adams, and Kevin Nilsen. I would also like to thank Prof. Chih-Lung Lin, Dr. Ming-Yang Deng, Dr. Po-Cheng Lai and Chia-Lun Lee from National Cheng Kung University for their valuable advice and fruitful discussions on display driving circuit and power consumption evaluation. In addition, the internship at Meta is also a wonderful experience in my life journey.

TABLE OF CONTENT

LIST OF FIGURES

LIST OF TABLES

CHAPTER1: INTRODUCTION

With rapid development of information technology, advanced display systems are becoming increasingly critical. All digital information needs to be displayed to the viewer. Flat panel displays have traditionally been used to show digital information, and nowadays they are ubiquitous in our daily lives [1–3]. Despite their widespread applications, there are still several hurdles for the display devices to overcome: 1. Limited immersion experience. An immersive experience requires a field of view (FOV) greater than 120 degrees, but for flat panel displays, the FOV is proportional to the display panel size. Therefore, to achieve an immersive experience (120º FOV), the display panel size should be very large. 2. Opaque devices. Flat panel displays are typically opaque and thus obstruct the objects behind them, creating a clear separation between the digital and physical worlds. Consequently, this makes it challenging to seamlessly integrate digital information into our environment. 3. Handheld devices. Portable or wearable displays typically require users to hold or strap them to their hands or arms, restricting their ability to operate in the real world.

1.1 Basics of near-eye display

Near-eye displays have gained significant attention as a promising solution to the above-mentioned obstacles. These displays use imaging optics to project a magnified virtual image to the viewer, allowing for a large FOV without requiring a large display panel. Additionally, since the displayed digital information is integrated into the physical world, near-eye displays offer a seamless user experience. Moreover, the compact form factor allows these devices to be worn on the head, freeing up the user's hands for other tasks. As a result, near-eye displays are expected to revolutionize the interface between digital information and the physical world [4–6]. In general,

near-eye displays can be classified into two types: virtual reality (VR) displays, and augmented reality (AR) displays [7]. VR displays create a digital virtual world that immerses the user and blocks the scenes from the real world. On the other hand, AR displays allow the user to overlay the digital information with the surrounding environment. A near-eye display typically consists of two main components: light engines and imaging optics. The image from light engine is first magnified by the imaging optics and then perceived by the viewer [8,9]. Figure 1-1 illustrates the different types of light engines [10]: 1) Light-modulating displays consisting of a light source for uniform illumination and a pixelated light-modulating layer for modulating the intensity of each pixel. The most typical one is a transmissive liquid crystal display (LCD) [11], where the backlight system provides uniform illumination, and the LCD panel controls the transmittance of each pixel to display the target image. Liquid-Crystal-on-Silicon (LCoS) is also a kind of light-modulating display, but it is reflection type [12]. 2) An emissive display consists of millions of self-emissive pixels, where the brightness of each emitter can be individually modulated by the driver circuit. Such a self-emissive light source can be an organic light-emitting diode (OLED) [13], quantum-dot light emitting diode (QLED) [14], or micro-LED [15]. 3) Light scanning display. The laser beam scanner (LBS) display consists of a laser module and a fast-response microelectromechanical system (MEMS). The MEMS steers the beam to the target pixel position while the laser module controls the intensity to display the target image content [16].

Transmissive LCD and OLED are presently the two primary display technologies used in VR displays, which do not require see-through properties. As a result, LCDs and OLED displays ranging from two to three inches are placed in front of the user's eyes. On the other hand, AR displays require see-through capabilities, so the opaque display panel cannot be placed in front of

the user's eyes, but instead, it needs to be placed sidewise. Therefore, light engines less than one

inch in size are necessary. Different display technologies, including LCoS, LBS, micro-OLED,

and micro-LED, have their own advantages and disadvantages [10].
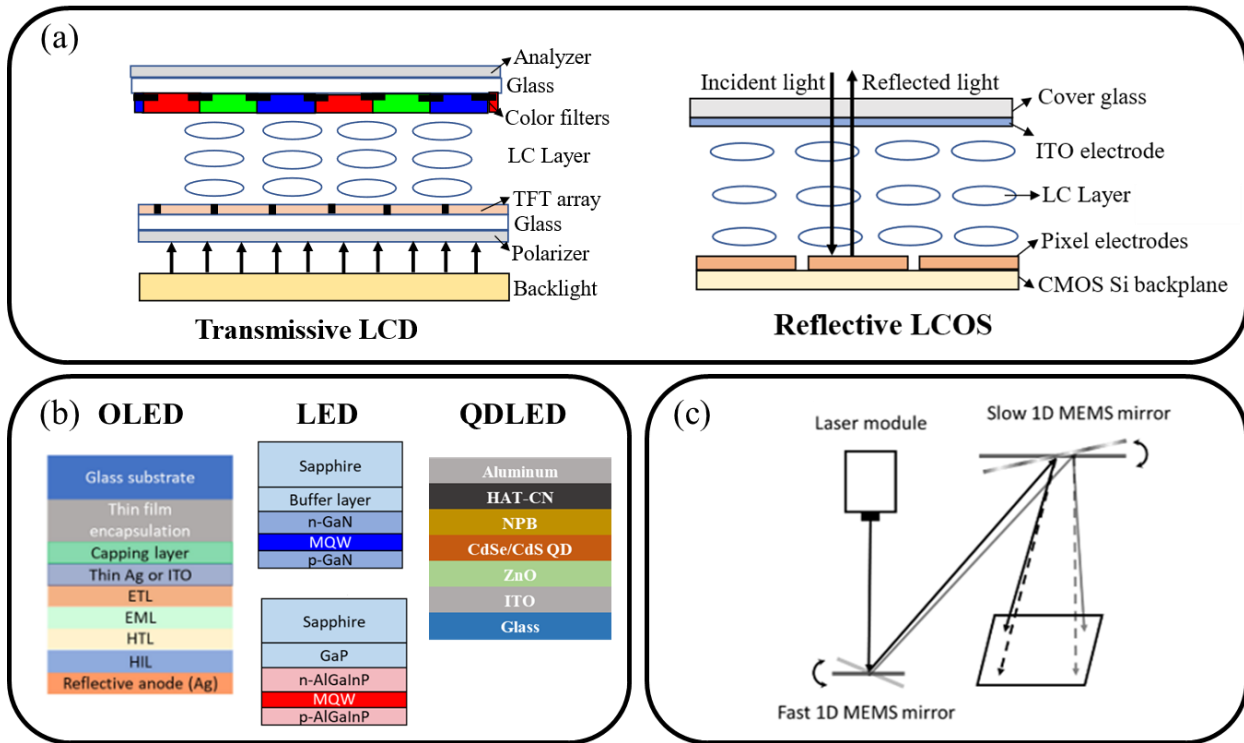
Figure 1-1 Schematic layout of different types of display light engines. (a) Light-modulating display; (b) Self-emissive displays; (c) Light scanning display.

The imaging optics plays a crucial role in converting spatial information of the light engine

into angular information, as depicted in Figure 1-2. In other words, the imaging optics projects

light from a specific pixel of the microdisplay to a ray from a specific viewing angle. In VR

systems, the viewer's eyeballs are located in the areas where different light paths overlap [17,18].

However, for AR systems, since the viewer's eyes are usually positioned to the side of the imaging

optics, additional optical components such as waveguides or holographic films are needed to

redirect the projected light toward the viewer [19]. The waveguide's input coupler is then placed

in the overlapping region of different optical paths to couple all the light into the waveguide.
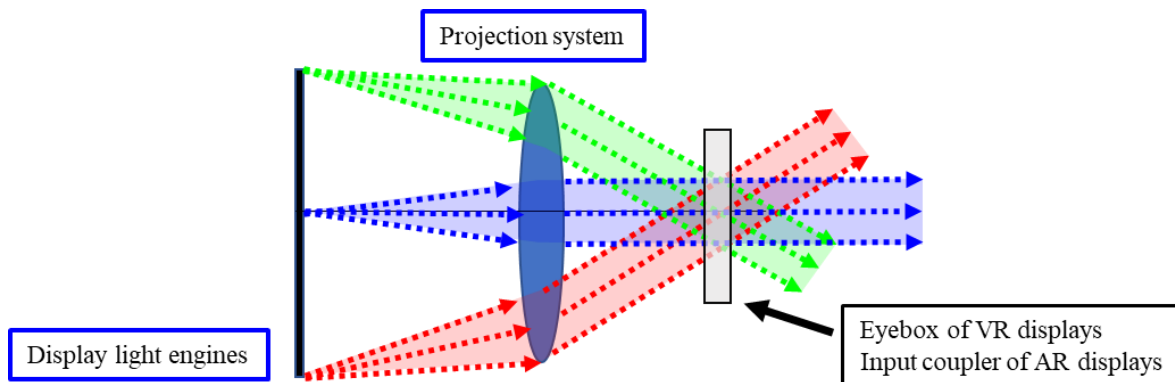
Figure 1-2 Schematic layout of a typical near-eye displays system.

1.2 Challenges and motivations

Although several near-eye display products are available commercially, the image quality of

most near-eye displays is far inferior to that of direct-view displays. Both light engine and imaging

optics of near-eye display systems play important roles to the degraded image quality. In addition

to image quality, the limited operation time of near eye displays also impacts user's experience. In

general, there are three major challenges for achieving high image quality and high efficiency near

eye displays:

1. High dynamic range (HDR). In a VR display, the goal is to generate a virtual world for the

   user. However, due to the large dynamic range of the real world scenes, from bright

   sunlight to dark night, the output images of VR displays should also have a high dynamic

   range to mimic the environment scenes [20–22]. For LCD, whose contrast ratio is about

   5000:1. Such a small light leakage from the LC panel results in a grayish background at

4

the dark state [23,24]. Despite the introduction of miniature light-emitting diode (mLED) local dimming backlight to improve the dynamic contrast ratio and bit depth of LCDs, the associated halo artifact remains a tough issue [25,26].

2. Degraded image quality. In addition to the defects of the light engine itself, the degradation of image quality can also come from the imaging optics. One of the most noticeable issues is the loss of resolution after the image magnification process, also known as the screen door effect [27,28]. Additionally, during the projection process, the imaging optics have uneven light collection efficiency on different pixels of the light engines, which can cause uneven brightness and color in AR/VR displays, a phenomenon known as the vignetting effect [29,30]. Moreover, stray light and the aberration of imaging optics can also cause ghosting and resolution loss in AR/VR displays [31,32].

3. Low efficiency display systems. The optical imaging system in AR/VR displays is highly inefficient. For instance, a Pancake-enabled VR display may lose as much as 75% of the light from the optical imaging system [33]. Similarly, diffraction-based waveguide AR displays typically have an optical efficiency of only about 1% [6]. In addition, high-resolution density light engines also suffer from low efficiency. For example, the small aperture ratio of a high-resolution LCD panel reduces the transmittance dramatically [34]. As the LED chip size decreases to support high-resolution densities, the efficiency of micro-LEDs also decreases [35,36]. As a result, the power consumption increases, which in turn reduces the operation time of the AR/VR headsets.

To improve the HDR performance of near-eye display systems, in Chapter 2, we introduce the design guidelines for HDR mLED backlit LCDs without halo artifacts. Then, in Chapter 3, we

describe an image quality evaluation model for VR displays to optimize the requirements of light engine. To improve the light engine efficiency, in Chapter 4 we demonstrate a patterned CLC film for the color-conversion micro-LED displays. It doubles the optical efficiency and enables a wide color gamut. Chapter 5 focuses on improving the efficiency of a VR display system by reducing the efficiency losses during the projection process through matching the etendue of the light engine and the imaging optics. As a result of this optimization, the optical efficiency is boosted by 40% while maintaining a reasonably good image quality.

CHAPTER 2: MINI-LED BACKLIT LCD

The content of this chapter was previously published in [25].

2.1 Background

HDR is a key requirement for next generation display light engines [21]. To achieve HDR performance, three criteria need to be met: 1) true black state and high peak brightness, i.e. high contrast ratio (CR>10^5:1), 2) wide color gamut (≈90% BT2020), 3) more than 10 bits (1024) grayscale [37–39]. However, until now, neither LCD nor OLED displays could meet all the above requirements. The contrast ratio of an LCD is limited by the depolarization effects of the thin film transistor array, LC layer and color filters, and also depends on the LCD mode employed. For multi-domain vertical alignment (MVA) LCDs, it has a CR≈5000:1, while for fringe field switching (FFS) LCDs, it has a CR≈2500:1 [40]. Although OLEDs exhibit unprecedented contrast ratios (CR≈10^6:1), their peak luminance and lifetimes still need to be improved [41,42]. Recently, tandem OLEDs have shown better lifetime and peak luminance, but their higher operating voltages may cause an extra burden to the driving circuit [43]. In addition, the bit depth of OLED devices is also limited by the driving circuit. Local dimming is an effective technique to improve the dynamic contrast of LCD [44,45]. The backlight unit is divided into hundreds to thousands of locally dimmable zones, and each zone can independently adjust the illumination according to the image content. In darker image areas, the corresponding mLED areas can be locally dimmed, while in brighter areas the backlight can be boosted accordingly. Therefore, the dynamic contrast ratio of LCD can be improved significantly. However, one drawback of local dimming technology is the halo effect [46]. Halo artifacts typically appear around the edges of bright objects surrounded

by dark backgrounds. In the edge area, the backlight is partially turned on to provide sufficient illumination for bright objects. Therefore, the luminance of a dark background around a bright object depends on the native contrast ratio of the LCD, which is about 2500:1 (FFS-LCD). On the other hand, turn off the mLED backlight in areas far away from bright objects to show a true dark state. As a result, the relatively high brightness at the edges of bright objects can cause halo artifacts.

According to [26], the halo effect can be reduced by increasing the LCD's native contrast ratio and the number of local dimming zones. However, there are still several unanswered questions regarding the halo effect in mLED backlit LCDs. For instances, firstly, when a display image is received by the human vision system (HVS) [47], the light scattering (glare spread function) inside human eye would spread out the light intensity from bright areas, thereby smearing the halo artifacts. Secondly, whether the halo effect is noticeable depends heavily on the image content itself, but objective methods to evaluate the observability of the halo effect in an image to the HVS have been lacking for a long time. Thirdly, it is unclear how the viewing conditions, such as viewing angle and ambient light intensity, affects the halo effect.

2.2 System modelling

In an mLED backlit LCD system, the light emitted from mLED chips is modulated by some optical films, such as quantum dot enhancement film, optical diffuser, and brightness enhancement film, before reaching the LC panel. Therefore, the light intensity distribution is highly related to the optical design in the backlight unit. Here, we simulate a 15.6-inch 3840×2160 LCD with a mLED backlight unit composed of 20,736 (108×192) LED chips with a pitch of 1.8 mm.

According to [48], we use following Gaussian function to present the light profile of a single mLED:

$$I(x_{LED}) \propto \exp - \left[\frac{(x_{LED} - x_{LED\_c})^2}{2\sigma^2} \right], \tag{2-1}$$

where x_{LED_c} is the locus of the mLED and σ is an expansion characteristic parameter. In our simulation, the ratio of σ to the mLED pitch is 0.6, which provides the backlight with a uniformity larger than 97%. Figure 2-1 illustrates the simulation process based on the point spread function theory for generating HDR mLED LCD images. In this example, the LCD panel has a CR=5000:1 and there are 162 local dimming zones in the backlight unit; each zone contains 12×12 mLEDs. First, the image is divided into several segments according to the number of local dimming zones. The mLED brightness in each zone depends on the maximum brightness in that zone, as shown in Fig. 2-1(a). Next, we apply the point spread function to each zone to calculate the luminance distribution on the LC layer in Fig. 2-1(b). After that, an 8-bit LC panel is used to modulate the luminance of each sub-pixel to achieve the target image content as Fig. 2-1(c) shows. To illustrate the halo effect more clearly, we depict the normalized contrast ratio distribution (the brightness of each pixel divided by the peak brightness of the display image) in Fig. 2-1(d), where the halo artifacts surrounding the chess crown are displayed.
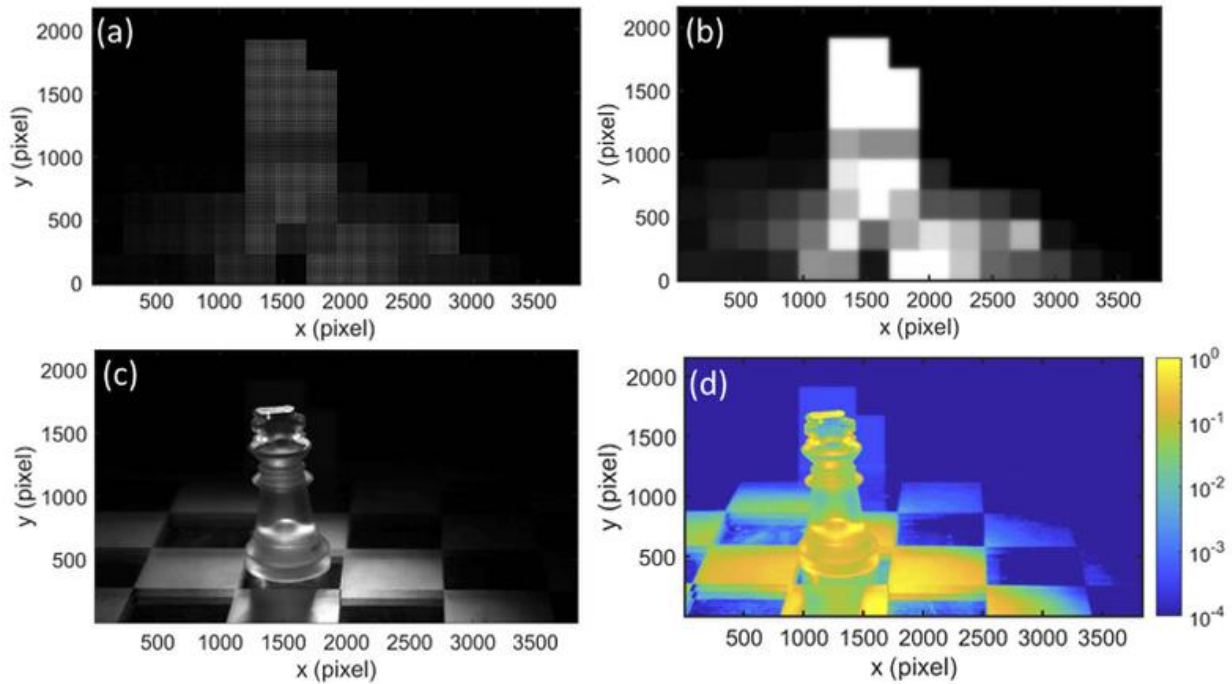
Figure 2-1 Displayed image of a mLED backlit LCD: (a) Intensity profile of the mLED backlight. (b) Luminance distribution of the light incident on LC layer. (c) Displayed image after LCD modulation. (d) Normalized contrast ratio distribution of the image displayed by mLED backlit LCD.

2.3 HVS

So far, we have successfully simulated the image performed by HDR mLED backlit LCD and clearly observed the halo effect in the simulated image. Next, we would address the first unanswered question: How light scattering in the eyeball smears halo artifacts. Considering the light scattering in human eye, it is very important to accurately analyze the halo artifacts perceived by the HVS. Here, we call the image on the display panel as "display image", and that received by the observer through HVS as "retinal image". According to the scattered light of human eye, one pixel will spread the light to adjacent pixel, and at the same time, the light from adjacent pixel will also be scattered to the pixel. To analyze the glare effect of human eye, the glare spread function

10

from the CIE standard is described below to simulate the relative light intensity scattered from one pixel to another:

$$
\begin{aligned}
Relative\_Luminance =[1-0.08\times(\frac{Age}{70})^4]\times & \left[\frac{9.2\times10^6}{\left[1+(\frac{\theta}{0.046})^2\right]^{1.5}}+\frac{1.5\times10^5}{\left[1+(\frac{\theta}{0.045})^2\right]^{1.5}}\right] \\
+[1+1.6\times(\frac{Age}{70})^4]\times & \left\{\left[\frac{400}{1+(\frac{\theta}{0.1})^2}+3\times10^{-8}\times\theta^2\right]+p\times\left[\frac{1300}{[1+(\frac{\theta}{0.1})^2]^{1.5}}+\frac{0.8}{[1+(\frac{\theta}{0.1})^2]^{0.5}}\right]\right\}+2.5\times10^{-3}\times p,
\end{aligned}
\tag{2-2}
$$

where θ is the visual angle between emitting and receiving pixels, Age stands for the observer's age, and p is the observer's pigmentation. To be consistent with our subjective experiment, here we set p=0 (dark eyes) and age=25. According to the visual angle between each pixel, the normalized glare spread function under 550 mm viewing distance is plotted in Fig. 2-2(a). Employing the glare spread function to "display image", we simulate the contrast ratio distribution in "retinal image", as shown in Fig. 2-2(b), including the influence of light scattering from human eye. Since light scattering occurs inside human eye, the light from high brightness pixels will spread to neighboring pixels, which smears the local contrast. As a result, the halo artifacts become blurred and are difficult to distinguish.
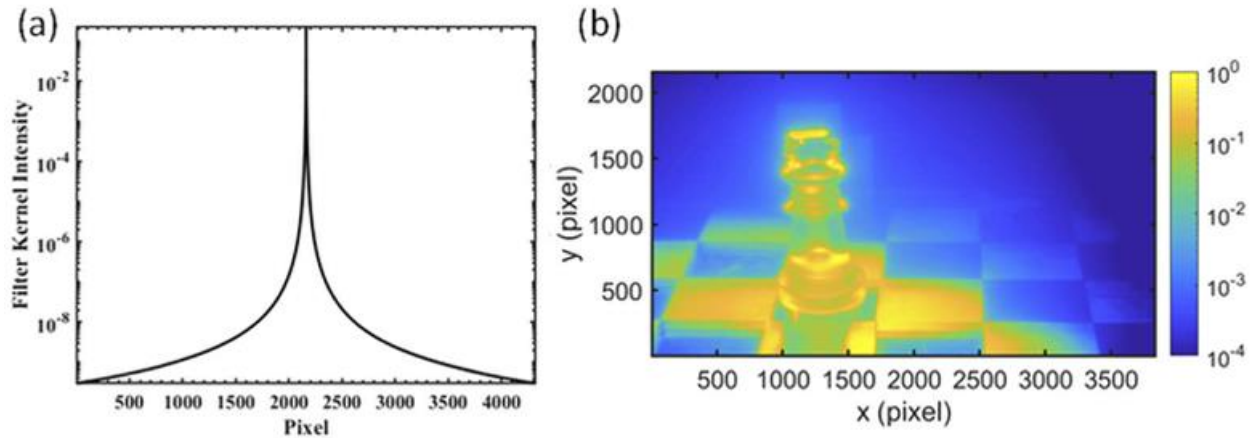
Figure 2-2 (a) The CIE standard glare spread function under the viewing condition in our subjective experiments. (b) Simulated retinal contrast ratio distribution.

<u>2.4 Image content</u>

After considering the impact of the human visual system on halo artifacts, we will address the second question: how to define an objective evaluation metric to evaluate the noticeability of halo artifacts for different image contents. Whether HVS notices the halo effect depends largely on the image content itself. Therefore, the number of local dimming zones required to suppress the halo effect will vary depending on the image content. For a long time, there was no objective method to evaluate such phenomenon. To overcome this problem, we use two factors to evaluate how HVS can observe halo effect in an image: 1) Local contrast ratio. When the local contrast ratio is high, to maintain the local high brightness the backlight should be bright. As a result, the halo effect in the dark area is more serious. 2) Local average luminance. The JND (just noticeable difference) of the human visual system is related to the average brightness [49]. When the local average brightness is low, the JND is also low, so the halo effect can be observed more easily. Therefore, here we propose a new evaluation method called "D-value", which is the ratio of local contrast to

local average brightness in an image, to assess the difficulty for the HVS to observe halo effect. The D-value can be defined as:

$$D-value = \frac{Local\ contrast\ ratio}{Local\ average\ brightness} = \frac{\left[\dfrac{Max(I(i,j)}{Min(I(i,j)}\right]_{\substack{i\in(1,M)\\j\in(1,N)}}}{\left[\dfrac{1}{M\times N}\sum_{i=1}^{M}\sum_{i=1}^{N}I(i,j)\right]} \qquad (2\text{-}3)$$

where M and N represent the numbers of pixels in the local area. In the following, we will explain how to define the size of a local area. Based on HVS, when the eccentric angle increases, human vision will be greatly reduced. Foveal vision corresponding to high-resolution areas is usually defined as $< \pm 2.0°$ from the center of fovea [50]. Therefore, we define the size of the local area corresponding to an eccentric angle $\pm 1.2°$. Under our subjective experiment setting, the angle range ($\pm 1.2°$) represents the surface area of 240 pixels $\times$ 240 pixels on the display panel. According to the number of local dimming zones, a local area may contain different numbers of local dimming zones. For example, the 4K2K display panel is divided into 162 local areas according to the local area size. When the number of local dimming zones is 162, 648 or 1458, one local area contains 1, 4, or 9 local dimming zones, respectively. In addition, the location of local area is aligned with the local dimming zones of the mLED backlight. The test image shown in Fig. 2-3(a) is used to illustrate how we define the local area and calculate the corresponding D-value. First, we down sample the image according to the local area size (162 local areas). Because one local area may contain more than one local dimming zones, the brightness of the local area is determined by the maximum brightness of the local dimming zones inside the local area, as shown in Fig. 2-3(b). As mentioned above, halo artifacts usually appear on the edges of bright objects surrounded by dark backgrounds. Therefore, there are two conditions for the halo artifacts to appear in local areas: 1)

13

in the local area, any local dimming zone is in a high brightness state, and 2) the local dimming zone of the adjacent local area is turned off, i.e., dark background. In order to find local areas that may have halo artifacts, we first find local areas with gray levels greater than 150 (bright objects). After that, 8 adjacent local areas surrounding the bright local areas are evaluated. If there are more than 3 adjacent areas with gray levels below 150, we say that the bright local area is surrounded by a darker background. Finally, we find the edge where the brightness changes sharply, as shown in Fig. 2-3(c). In Fig. 2-3(d), we have outlined five local areas, where the highest D-values are represented by red lines, and their corresponding D-values are listed inside the boxes. In Fig. 2-3(d), based on the D-value method, we predict the local areas with a larger D value should have more severe halo artifacts. If we compare the local areas plotted in Fig. 2-3(d) with halo artifacts shown in Fig. 2-1(d), the plotted local area has a good match with the region where halo artifacts occur. Therefore, we verify that our D-value method can reflect where the halo artifacts occur.
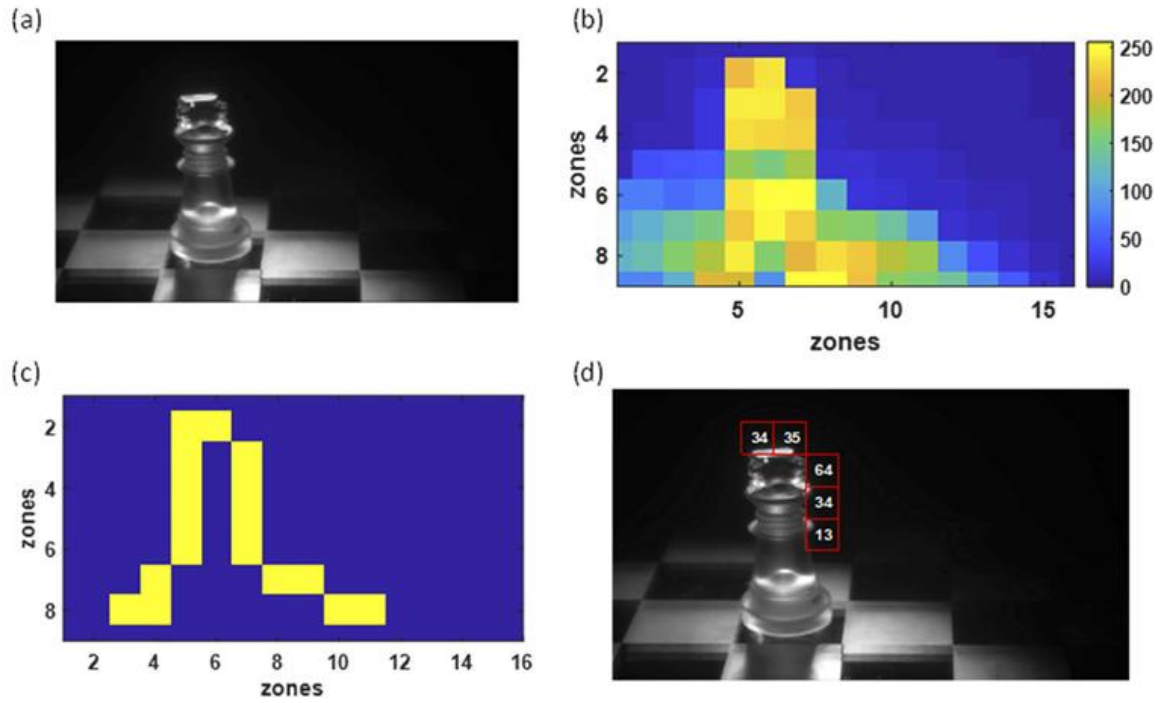
Figure 2-3 (a) The test image; (b) The down sampled image according to HVS; (c) The local area may have halo artifacts; (d) The top five D-values in the local area may have halo artifacts.

By applying the D-value evaluation method to a target image, the local area where the HVS is easier to detect the halo artifacts is found. To quantitatively analyze the halo effect in these local areas, an evaluation metric called peak signal-to-noise ratio (PSNR) is applied. Here, the PSNR in these local areas is called LocalPSNR, which is defined as:

$$LocalPSNR = 10 \times \log_{10} \left[\frac{(I_{max})^2}{\frac{1}{M \times N} \sum_{i=1}^{M} \sum_{j=1}^{N} (\Delta I(i,j)^2)} \right], \tag{2-4}$$

where M and N represent the number of pixels in the local area (240×240), Imax is the difference between black and white, and ΔI is the brightness difference between simulated retinal image and target retinal image. Unlike the PSNR of an entire image that considers all pixels in the image, the

advantage of LocalPSNR is that we can exclude pixels that are far away from areas where halo artifacts occur. Taking the 4K2K images as an example, there are approximately 8-million pixels in each image. However, only pixels at the edge of bright objects surrounded by a dark background will be affected by the halo artifacts. Therefore, compared to the PSNR of entire image, LocalPSNR can reflect the degraded image quality by halo effect more accurately.

Let us take the test image shown in Fig. 2-3(a) as an example. Through the model described above, we simulated the retinal image of a mLED backlit LCD system with seven different local dimming zone numbers (18, 162, 648, 1458, 5832, and 23328) and four LC contrast ratios (1000:1, 1588:1, 2500:1 and 5000:1). To further explain the function of LocalPSNR, we plot the normalized contrast ratio distribution of OLED display in Fig. 2-4(a), and mLED backlit LCD system with 162 and 648 local dimming zones in Figs. 2-4(b) and 2-4(c) for comparison. The boundary of local areas defined by the D-value method is outlined by red color. First, we can clearly observe that as the number of local dimming zones increases, the halo artifacts inside the local area decreases. Therefore, the image of mLED backlit LCD inside the local areas becomes more comparable to that of OLED display. This image quality improvement is also reflected by the higher LocalPSNR in Fig. 2-4(d). As a result, for discussing the image quality degradation results from the halo artifacts, we think analyzing the image quality inside these local areas is convincing and more efficient. The LocalPSNR of all simulated images are calculated and shown in Fig. 2-4(d). In line with our expectation, a higher contrast ratio and more local dimming zones help eliminate halo artifacts, thereby improving the image quality of the mLED backlit LCD.

16
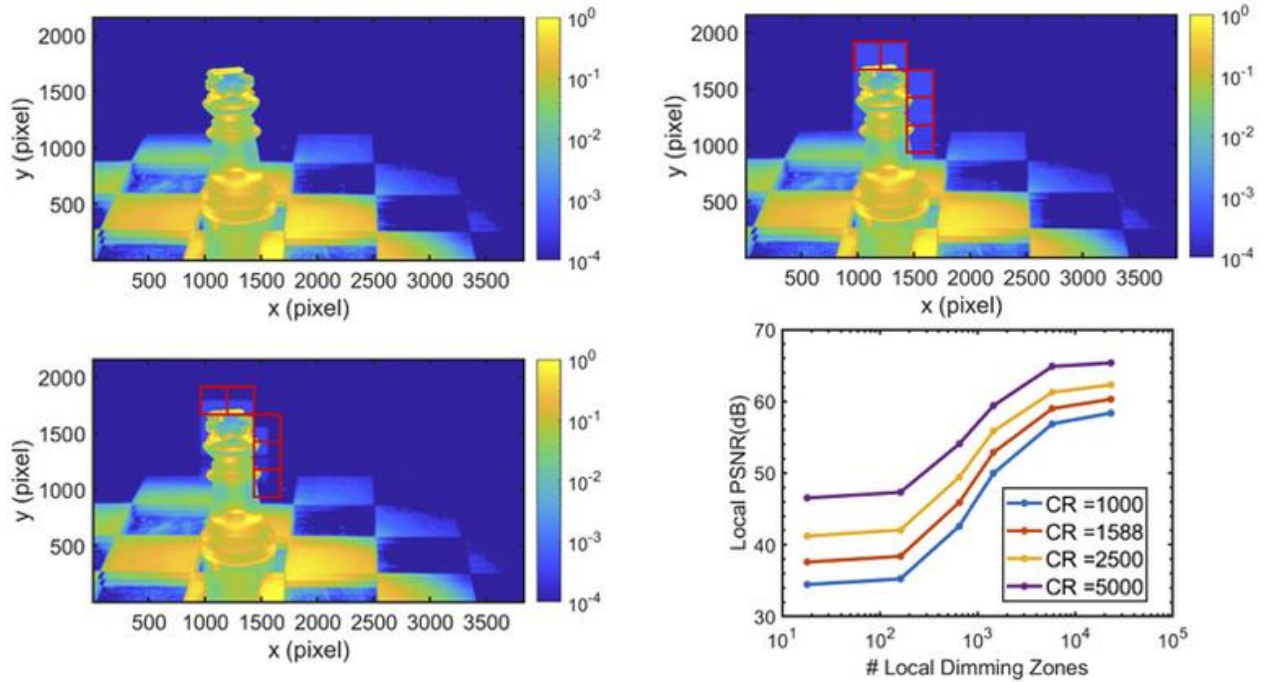
Figure 2-4 Normalized contrast ratio distribution of the image generated by (a) OLED display, (b) mLED backlit LCD with 162 local dimming zones, and (c) mLED backlit LCD with 648 local dimming zones. (d) Simulated LocalPSNR of target images.

2.5 Viewing environment effect

In this section, we discuss the third issue: how the viewing environment affects the halo artifacts. In the above discussion, the viewing environment is completely dark, and the viewing angle is in the normal direction. However, in practical applications, the viewing environment has a significant impact on the halo effect of mLED backlit LCD. When displaying images under ambient light conditions, the total brightness received by the human eye consists of two parts: displayed signal and ambient light reflected from the display surface. Here, we conduct an experiment to measure the ambient light reflected from the display (OLED laptop Dell XPS15) as shown in Figs. 2-5(a) and 2-5(b). Two floor lamps and two ceiling lamps were used to generate four levels of ambient lighting conditions, namely 0 lux, 100 lux, 300 lux and 500 lux. The

17

corresponding reflected ambient luminance measured by the luminance meter was 0 nit (below the measurement capability), 0.46 nit, 1.26 nit, and 2.47 nit, respectively. The corresponding surface reflectivity is about 1.5%. A simple image with a white dot in the center and surrounded by dark background was used to analyze the ambient light effect on halo artifacts. Through adding the reflected ambient luminance to the displayed image and including the glare effect of HVS, the retinal image comparison between the OLED display and the mLED (162 zones) is shown in Fig. 2-6(a). In addition, in Fig. 2-6(b) we also plot the comparison with 4% surface reflectivity, which is the normal value for commercial touch panels. We can clearly observe that the halo artifacts in the adjacent areas of the central bright spot are washed out by the reflected ambient light. As a result, as the ambient light brightness increases, the number of local dimming zones required for an mLED backlit LCD to maintain the same image quality as an OLED display decreases. The subjective experiments in the following section will further verify this phenomenon.
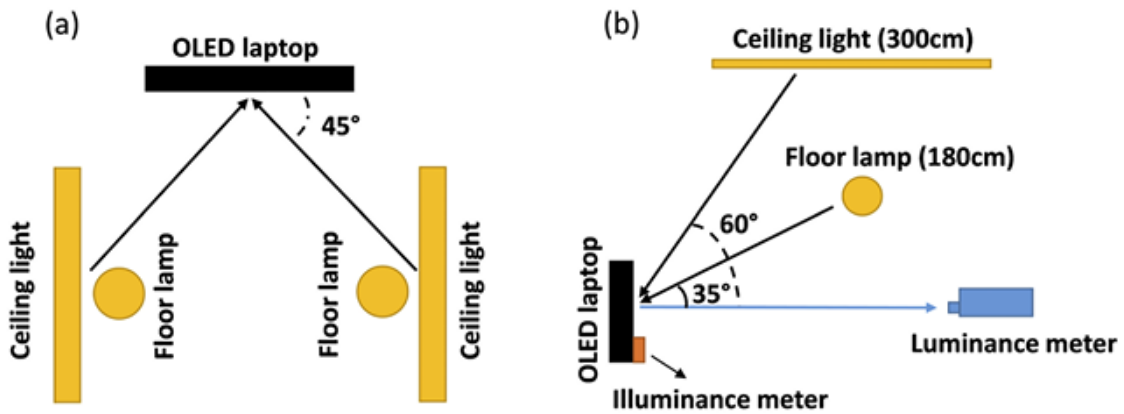
Figure 2-5 (a) The ambient light source arrangement (bird view) and (b) measurement condition (side view) in the ambient light experiment.
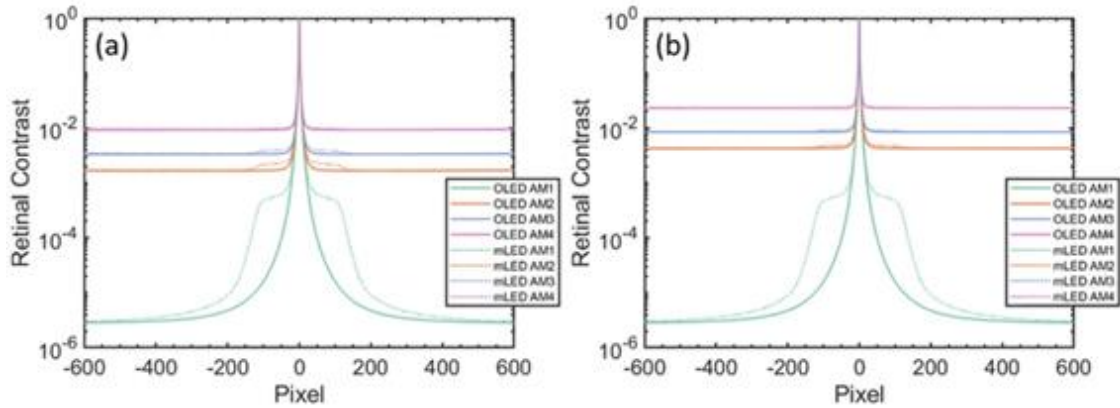
Figure 2-6 The contrast ratio of retinal image generated by an OLED display and a mLED backlit LCD under different ambient illuminances and surface reflectivity (a) 1.5%, and (b) 4%. The ambient (AM) 1 to 4 corresponds to 0 lux, 50 lux, 100 lux, and 300 lux, respectively. The peak brightness of mLED backlit LCD and OLED display is 400 nits.

<div align="center">2.6 Subjective experiment</div>

After answering all the questions about halo artifacts by optical simulation methods, we further conduct subjective experiments to verify our results and establish the correlation between subjective responses to the proposed evaluation metrics. For example, based on the optical simulation process described above, we proposed a quantitative D-value to evaluate the difficulty of HVS to distinguish halo effect with various image contents. After that, LocalPSNR is applied to reflect the local area image quality where the halo artifacts appear. However, it is necessary to further define the minimum LocalPSNR value (perceptual limit) so that HVS cannot distinguish the halo artifacts in an mLED backlit LCD. In addition, by adding reflected ambient light to the displayed image, we find that the halo artifacts could be washed out by the ambient light. However, perception limit in various ambient conditions is still unknown. Therefore, in this section, a subjective experiment is designed to find the local dimming zone number required to display images with indistinguishable halo effects under different image contents and different ambient

light conditions. As shown in Fig. 2-7, five images are used in our subjective experiment. Ten people with normal or corrected vision participated in the subjective experiment. Half of them is display experts with basic knowledge of halo effect, and the rest are ordinary people without relevant knowledge. Four different ambient light illuminances are used to study the impact of ambient lighting. The ambient light setting is the same as Fig. 2-5(a), and the background behind the monitors is a white painted wall. One thing that should be mentioned is that the floor lamp is on the left and right behind the observer, so there is no direct light from the illuminator to the observer. Two OLED panels (Dell XPS 15 laptop, panel size 15.6-inch, resolution 3840×2160) are employed as the image sources and placed 55-cm away from the observer. One of the OLED panels displays a simulated image of mLED backlit LCD with different local dimming zone numbers and contrast ratios. The other OLED panel displays the control image. Observers are asked to determine whether they can find the difference (halo artifacts) between a pair of displayed images. In one test image, 112 pairs (7 different numbers of local dimming zones, 4 different ambient light illuminances, 4 different LCD contrasts) of images are displayed to each observer. In order to avoid the effects of visual fatigue and prejudice, the observers are required to close their eyes between each pair of images, and the simulated image and the control image will be randomly displayed on one of the laptops. In addition, the interval between each ambient light is 15 minutes to ensure correct visual adaptation.
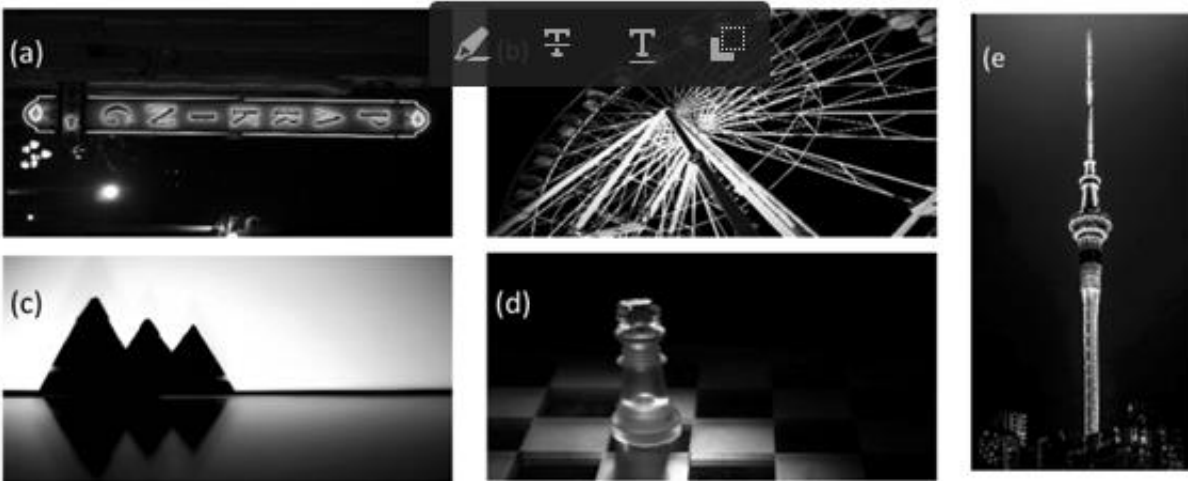
Figure 2-7 HDR target images for the subjective experiments: (a) Parking sign, (b) Ferris wheel, (c) Mountains, (d) Chess, and (e) Tower.

Four types of ambient condition are taken into consideration in our subjective experimental results, the required zones number of mLED backlit LCD to eliminate the halo artifacts is shown in the Fig. 2-8. In most images shown in Figs. 2-8(a), 2-8(b), and 2-8(d), as the ambient light increases, the halo artifacts are washed out and thereby fewer zone number can achieve same image quality. However, in Fig. 2-8(e), the D-value of this image is the largest among all the five images evaluated: the D-value for Parking sign is 50.05, Ferris wheel is 8.63, Mountains is 2.33, Chess is 34.44, and Tower is 75.78. As mentioned above, a large D-value indicates that the halo effect in the image is easy to recognize by HVS. Thus, even if we increase the contrast ratio of the LCD panel or ambient light illuminance, the required local dimming zones number is still high. On the other hand, in Fig. 2-8(c), the D value of this image is the lowest among all test images so the halo effect in the image is hard to distinguish by HVS. The observers cannot see the halo artifacts even though the zone number is only 18. The benefit of making more local dimming zones is limited. In these two extreme cases, local dimming cannot provide great improvement in image quality.
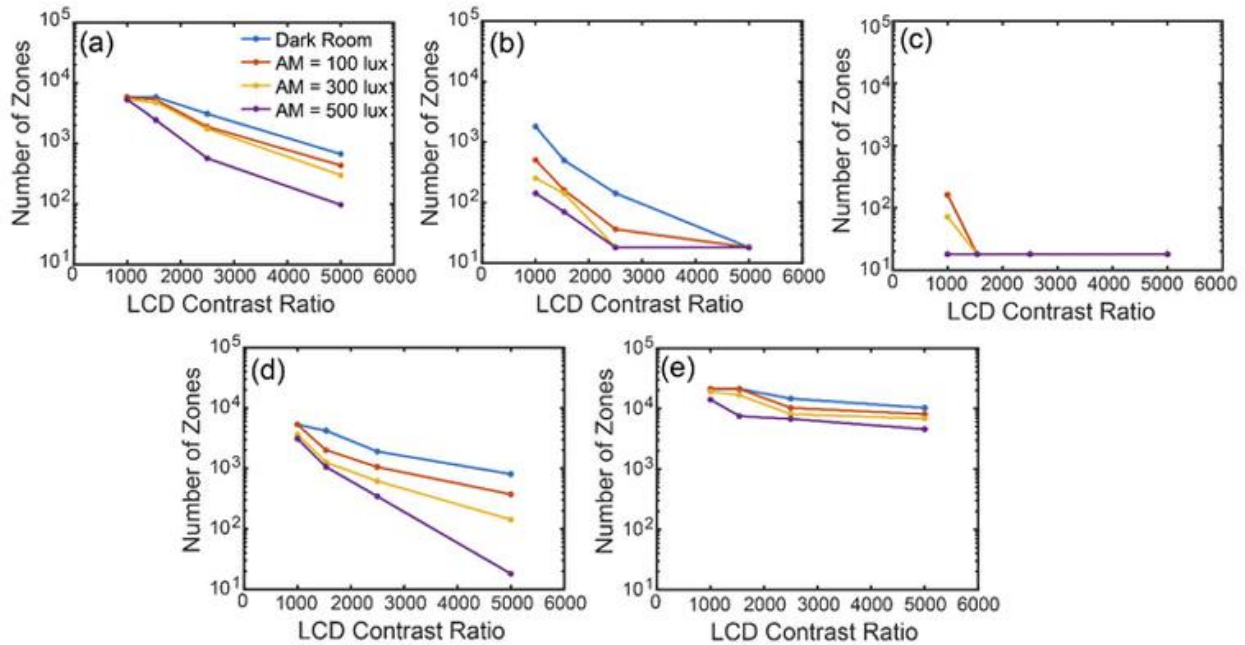
Figure 2-8 Required local dimming zone number to suppress the halo effect under different ambient lighting: (a) Parking sign, (b) Ferris Wheel, (c) Mountains, (d) Chess, and (e) Tower.

In the following discussion, as we define a suitable local dimming zone number for different ambient light conditions, we focus on the images whose quality can be improved by the local dimming method. The average zone number from these images under different ambient conditions is shown in Fig. 2-9. According to our subjective experiment, as the ambient light gets brighter, the halo effect is alleviated. Thus, an mLED backlit LCD can obtain comparable image quality to OLED with a fewer local dimming zone number. In addition, the LCD panel with a high native contrast ratio leads to weak halo artifacts, which is easier to be washed out by the ambient light. For example, for an mLED backlit LCD with CR=1000, the required zone number is reduced from 4500 to 2800 when the ambient light increases from 0 to 500 lux. However, in the same ambient light range, when the LCD's CR=5000, the required zone number drops from 500 to 40.
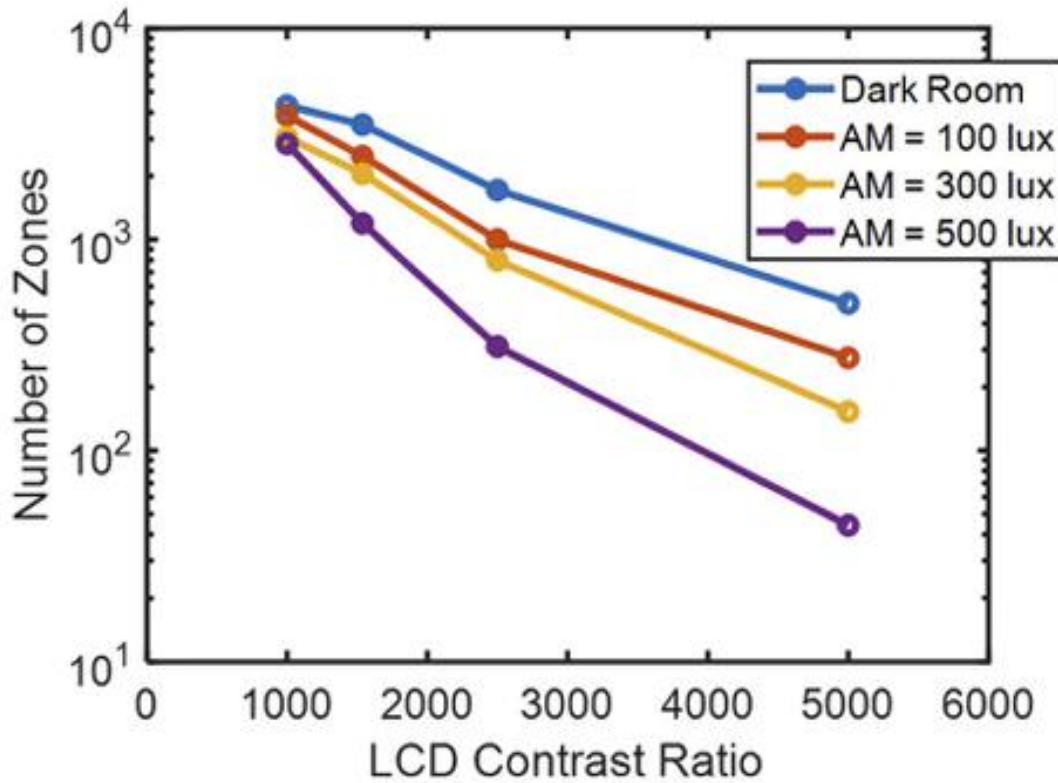
Figure 2-9 Required local dimming zone number to achieve indistinguishable halo effect under different ambient lighting conditions. Here, we only consider those image contents that can be improved through local dimming.

<u>2.7 Summary</u>

While mLED-backlit LCDs can widen the dynamic range and enhance the contrast ratio through local dimming technology, the accompanying halo artifact severely degrades the image quality. In this chapter, we focus on analyzing and mitigating the halo artifacts of mLED-backlit LCDs. We build an optical simulation model to analyze the root cause of halo artifacts of an mLED backlit LCD. Moreover, since all displayed images are perceived by the HVS, we further take the HVS effect into account and find that the light scattering in the HVS helps to smear halo artifacts. Furthermore, we propose an objective metric (D-value) to evaluate the noticeability of halo artifacts under different image contents. Our results show that if the D-value is too large (75.78)

23

or too small (2.33), the image quality cannot be noticeably improved by the local dimming method. Additionally, the D-value metric can identify the local areas where halo artifacts are most noticeable. The PSNR values of these local areas are further defined as Local PSNR to reflect the severity of halo artifacts. Then, we also evaluate the halo artifacts of mLED-backlit LCDs under different viewing conditions, including various ambient lighting conditions and viewing angles. Further visual experiment is conducted and find that as the ambient illuminance increases from 0 (dark room) to 500 lux, the dimming zones required to suppress the halo effect are reduced by ~10x.

CHAPTER 3: OPTIMIZING LIGHT ENGINES FOR VR DEVICES

3.1 background

The HDR standard has always been the pursuit of both direct view displays and head-mounted displays. Chapter 2 provides a detailed analysis of how to design a HDR mLED backlit LCD without halo artifacts. In this chapter, we focus on of how to design HDR head-mounted displays. In a VR device, the image from display light engines is first magnified by the imaging optics and then received by the human visual system. In the past, the requirements of a display light engine are designed based on the visual acuity and dynamic range of HVS. The magnified image after imaging optics should support visual acuity of 60 pixels per degree (ppd) and sufficient dynamic range. Therefore, display light engines with high resolution density and high dynamic range are required [22,51].

From the perspective of high-resolution density, according to the focal length of the imaging optics (40 mm) and the target visual acuity (60 ppd), the required resolution density for the display light engine is calculated to be about 2200 ppi [52]. Moreover, the required resolution density is inversely proportional to the focal length of the imaging optics. Therefore, an advanced catadioptric imaging optics, known as pancake lens, helps shorten the focal length (< 30mm) to obtain a more compact form factor, but it requires a higher resolution density display light engine (>3000 ppi). The major challenge of a high-resolution density LCD is its relatively low optical efficiency, and a white OLED display light engine is its increased electrical and optical crosstalk [53]. On the other hand, from high dynamic range viewpoint, light leakage from an LCD panel reduces the contrast ratio. To increase contrast ratio and dynamic range, LCDs with dual light modulation layers have been developed. The first light modulation layer is the LC panel, and the

second layer can be a 2D mLED array, a lower resolution density LCD panel, or a laser beam scanning system. The details of 2D local dimming mLED backlit LCD for direct-view displays have been discussed in Chapter 2. Here, we focus on the mLED backlit LCDs for VR applications [54,55]. Some VR products equipped with a mLED backlight have been released. However, to mitigate halo artifacts, mLED backlight with thousands of local dimming zones is not uncommon; each local dimming zone corresponding to 0.41° viewing angle (i.e., 2.43 zones per degree), when the native LCD contrast ratio is 2000:1 [26]. With the same local dimming zone density, to achieve 100° field of view (FOV) in a VR headset, we need 243×243 local dimming zones for a 2-inch display light engine. The corresponding local dimming zone size is only about 150µm, which is challenging to fabricate. Therefore, when implementing mLED backlit LCDs for VR devices, the density of local dimming zones is often much lower than that of direct-view displays. Self-emissive displays, such as organic light-emitting diode (OLED) and micro-LED displays, are regarded as outstanding display light engine candidates because of their excellent dark state. However, in practical applications, the small pixel size restricts the design of compensation driving circuits, thereby degrading the image quality. Based on the above discussion, for all types of display light engines, it is extremely difficult to meet the HVS requirements. But do we really need to design a display light engine to meet all the demanding HVS requirements remains a good question to be explored.

3.2 Pancake lens design

As shown in Fig. 3-1(a), in this study, for simplicity, we use a single-lens VR imaging optics in the system. Details of the lens design have been reported earlier [56,57]. The front surface of

26

this pancake lens is a half mirror. The back surface of the pancake lens is a reflective circular polarizer that reflects one circular polarization while transmitting the opposite one. Let us assume it reflects righthanded circularly polarized (RCP) light and transmits the lefthanded circularly polarized (LCP) light. Such a reflective circular polarizer consists of a half-wave ($\lambda/2$) plate, a $\lambda/4$ plate, and a multilayer reflective polarizer. The optical axis of the $\lambda/2$ plate and the $\lambda/4$ plate is at 15° and 75°, respectively, to form a broadband quarter-wave plate. Regarding the reflective polarizer, multilayer films with central wavelengths of 0.42, 0.46, 0.50, 0.55, 0.60, 0.65, 0.70, 0.76, and 0.82 µm are used for broadband applications [58]. While more complex optical designs such as two- or three-lens designs and multi-twisted $\lambda/4$ plates [59] could further improve the PSF and suppress the stray light for the pancake VR devices. However, some of these designs are costly and have alignment issues, and some cause more surface reflections (stray light). The goal of this work is to establish the display requirements based on the optical performance of the VR imaging optics. To keep in mind that a different VR imaging optics leads to different display requirements. The measurement system consists of an ideal lens with 4-mm aperture and a receiver located at the focal plane of the ideal lens. When a collimated light impinges the lens at a different angle, it is focused at an off-axis position. Meanwhile, as long as the incident light is not perfectly collimated, the focus on the receiver is blurred.

As mentioned above, the PSF of the imaging optics consists of the effects from aberrations and stray light. In this paragraph, let us first focus on the impact of aberrations on image quality, so we turn off the raytracing of stray light in the optical simulation model. Figure 3-1(b) shows the ray paths of point sources at different x-axis positions. The point source at the center corresponds to the normal viewing angle. As the point source moves from the center to the positive x-axis on

the microdisplay, the image is formed in the negative x-axis of the receiver. As shown in Fig. 3-1(b), the corresponding viewing angle of each point source can be calculated through L_1 and L_2, where L_1 is the distance between the lens and the receiver, and L_2 is the distance between the center of receiver and the imaging point. Different point source corresponds to various L_2 on the receiver and different viewing angle. Figure 3-1(c) depicts the intensity distribution of different point source within the 20° FOV and the corresponding viewing angle is also marked in the figure. Here, we focus on the analysis within 20° FOV, which is a typical eye rotation range. For the FOV larger than 20°, the users often turn their heads. It appears that a point source located far from the center results in a lower peak intensity and a wider spot size. In other words, the resolution of the lens drops sharply. We further align the peak positions of different intensity distributions, as shown in Fig. 3-1(d), to illustrate that the intensity distribution broadens with increasing viewing angle. Aberrations widen the intensity distribution, which in turn lowers the maximum resolvable density of light engines. This is different from ideal resolution density based on the human visual acuity, which is 60 pixels per degree. However, after considering the aberration of VR imaging optics, the targeted resolution density of light engines should be determined by the resolving power of imaging optics, rather than HVS.
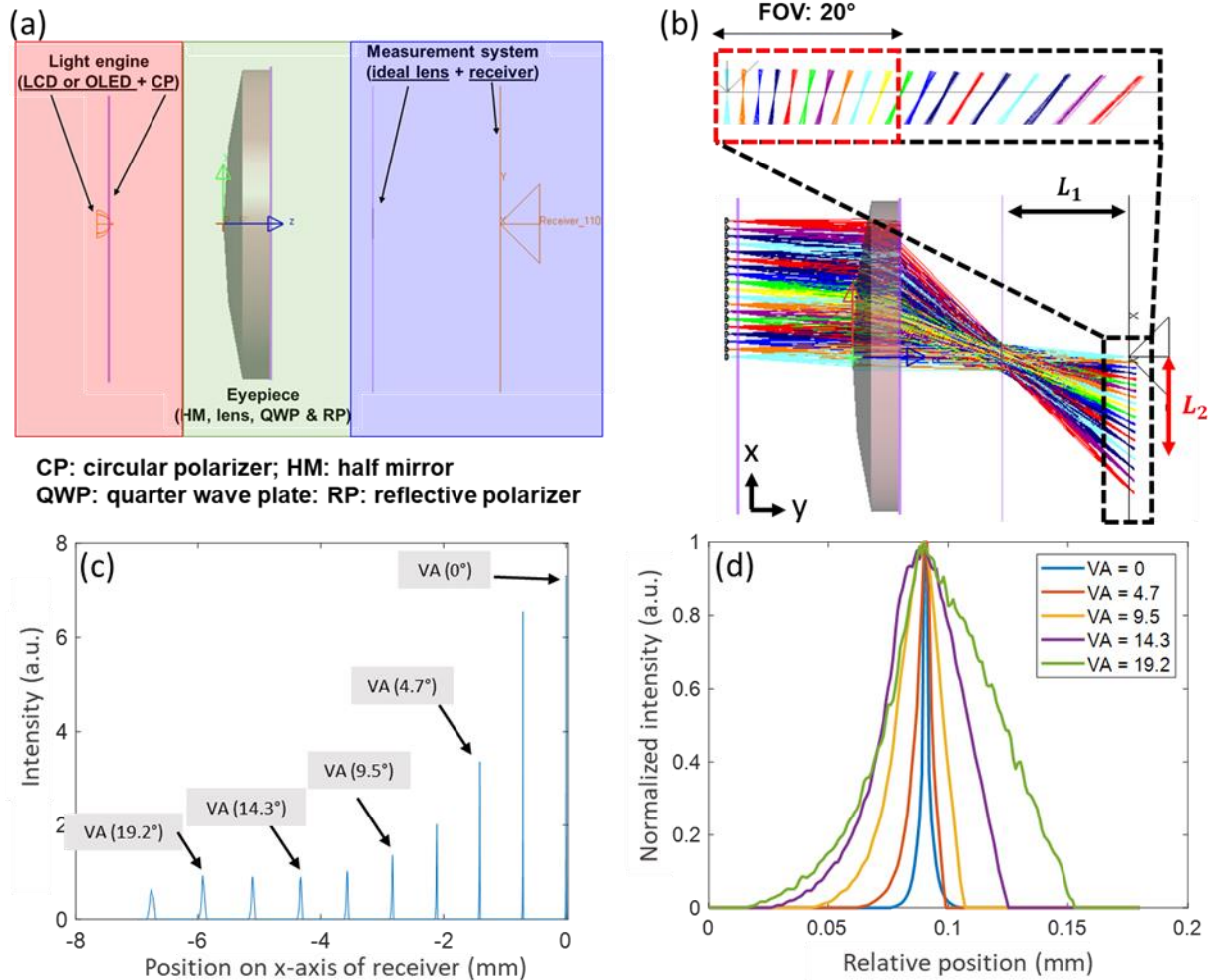
Figure 3-1 (a) Schematic of Pancake VR device in LightTools. (b) The ray path of point source in different positions with 1-mm step. (c) The 1D intensity distribution of each point source. (VA: viewing angle) (d) Normalized intensity distribution of point sources corresponding to different viewing angles, where the peak positions of the different intensity distributions are aligned.

In this paragraph, the effect of stray light on the PSF of the imaging optics is considered. Stray light is caused by the surface reflection and depolarization of imaging optics. The optical path scheme of the pancake imaging optics is shown in Fig. 3-2. The non-ideal reflective polarizer and quarter-wave plate cannot convert the light of different wavelength and incident angle to the desired circular polarization as it propagates through the imaging optics. In common practices, the

polarization is slightly elliptical, which causes stray light to degrade the image contrast in a VR device. Figure 3-2(a)-(c) shows different types of light paths in different colors: signal (green color), stray light: type 1 (orange color), and stray light: type 2 (red color), respectively. To evaluate the stray light effect, we need to trace the stray light whose intensity is much lower than that of the signal beam. Here, we lower the raytracing power threshold to 10^{-5}, which means rays are traced until the power drops below 10^{-5}. Also, to maintain the simulation accuracy, the total number of traced rays is $2\mathrm{x}10^8$, and more importantly, after a ray hits each surface, it is further split into reflected, transmitted, and absorbed rays. Compared to the signal beam passing through the pancake lens three times, type 1 stray light passes through the pancake lens only once. Therefore, it has a shorter optical path in the pancake lens, i.e., it experiences a smaller optical power. This insufficient lens power results in a diverging beam impinging on the ideal lens, and the diverging beam would be focused farther from the intended receiver. By contrast, type-2 stray light is reflected twice by the RP and experiences a stronger lens power than the signal beam. As a result, the ray path is focused in front of the intended receiver. Additionally, Fig. 3-2(d) illustrates the stray light from an off axis point source, where the center of the stray light is separated from the signal beam. In other words, ghost images caused by stray light do not surround the target image point but are separated from it. It is worth mentioning that in Fig. 3-2(d) we only show the signal beam and type 1 stray light, which are the ray paths with maximum power, without including the type 2 stray light, to keep the figure visible. For the point source located at the center of display, the power ratio of stray light to signal ray is about 3.65%. This value is comparable to the result (2%-10%) reported in [60].
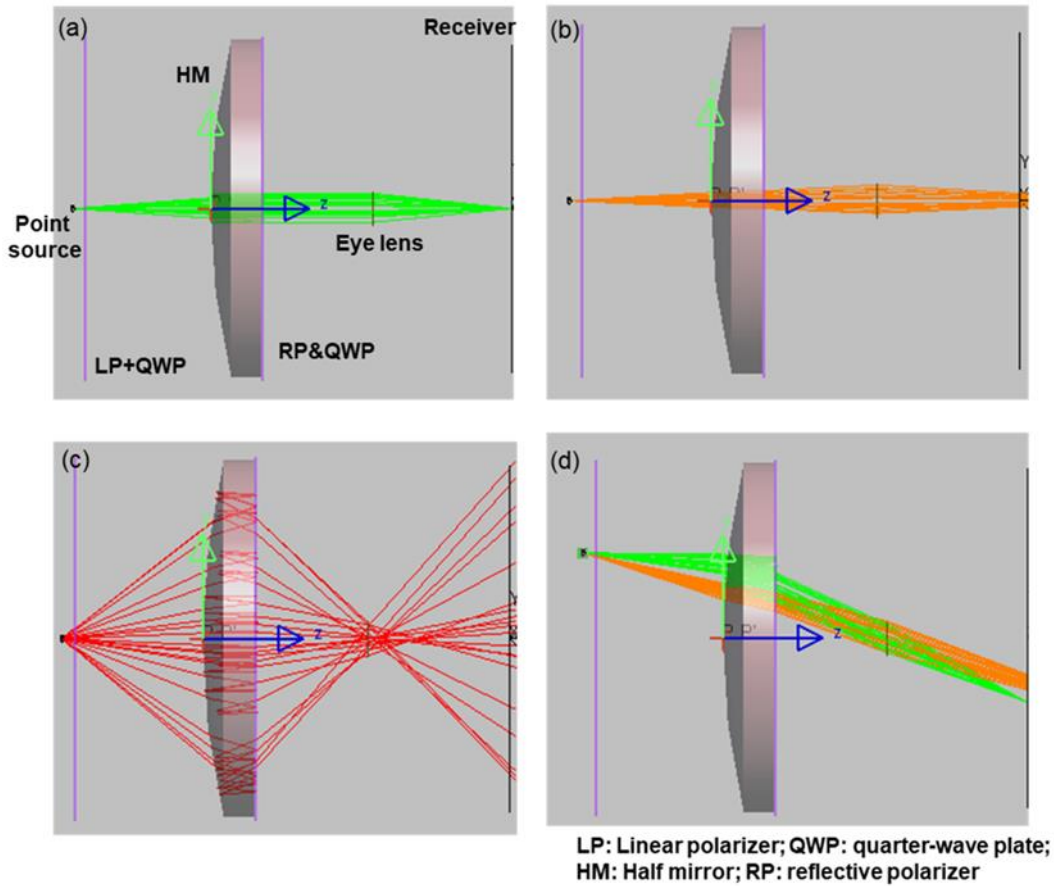
Figure 3-2 The scheme demonstrating the light path for a pancake VR device. The path of (a) signal ray (green color), (b) stray light (type 1; orange color), and (c) stray light (type 2; red color) in the LightTools simulation model. (d) The path of signal ray (green color) and stray light (type 1; orange color) of an off axis point source.

After separately introducing the effects of aberrations and stray light on the PSF of the imaging optics, we take both factors into consideration in the following analysis. Different test patterns as shown in Fig. 3-3(a) are applied to the VR device to evaluate the stray light effect on image contrast. The white image size corresponds to a FOV of approximately 40° (± 20°). In each test pattern, the central black image occupies 2.5°, 7°, and 12° of FOV, respectively. For an ideal imaging optics, the central area should be black (intensity = 0). However, the stray light from adjacent pixels lowers the image contrast, as Fig. 3-3(b–d) shows. Here, the image contrast is

defined by the ratio of average intensity of dark areas to the average intensity of bright areas. The image contrast for the three presented patterns is 108:1 (FOV = 2.5°), 236:1 (FOV = 7°), and 422:1 (FOV = 12°), respectively. Figure 3-3 illustrates that although a perfect microdisplay is applied, the image contrast is severely degraded by the stray light of imaging optics. It is worth mentioning that when the dark area expands to about 12° FOV, the intensity at the center of the dark area is reduced to zero. As a result, we did not continue to increase the dark area size.
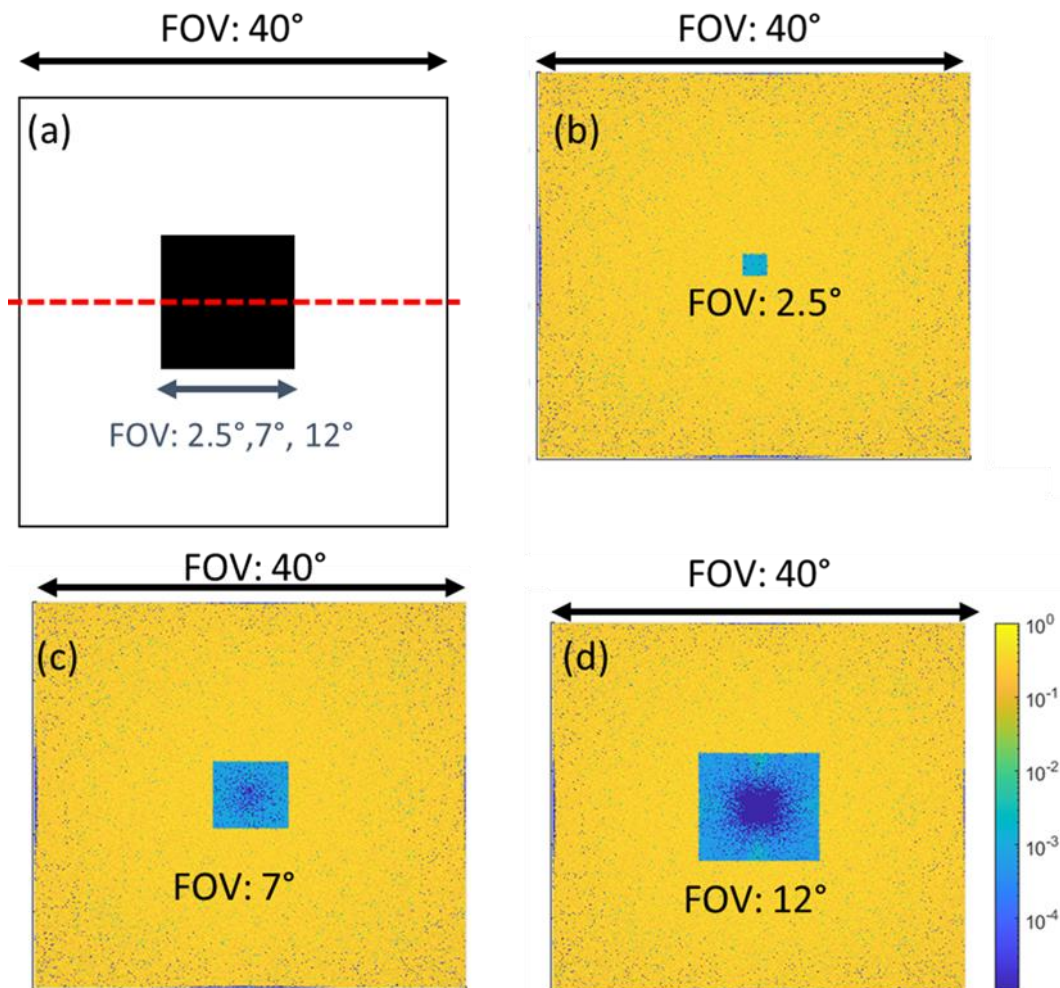
Figure 3-3 (a)The test pattern with different size of dark region (FOV = 2.5°, 7° and 12°). Normalized illuminance distributions of test patterns with dark regions corresponding to (b) 2.5°, (c) 7°, and 12° FOV.

3.3 Display light engines

From the perspective of microdisplays, two types of microdisplays are widely used in VR headsets: LCDs and OLED displays. Due to the limited intrinsic contrast of LCDs (<5000:1), the small light leakage in the dark state cause image artifacts in a VR device. In the following, we evaluate the dark state of a display with a contrast ratio of 500:1, 1000:1, 2000:1, and 106:1 (perfect dark state). Here, OLEDs, mLED backlit LCDs, and micro-LEDs are considered as having a perfect dark state, where the brightness of dark state is zero. The radiation pattern of the display is set to be directional as Fig. 3-4(a) shows.
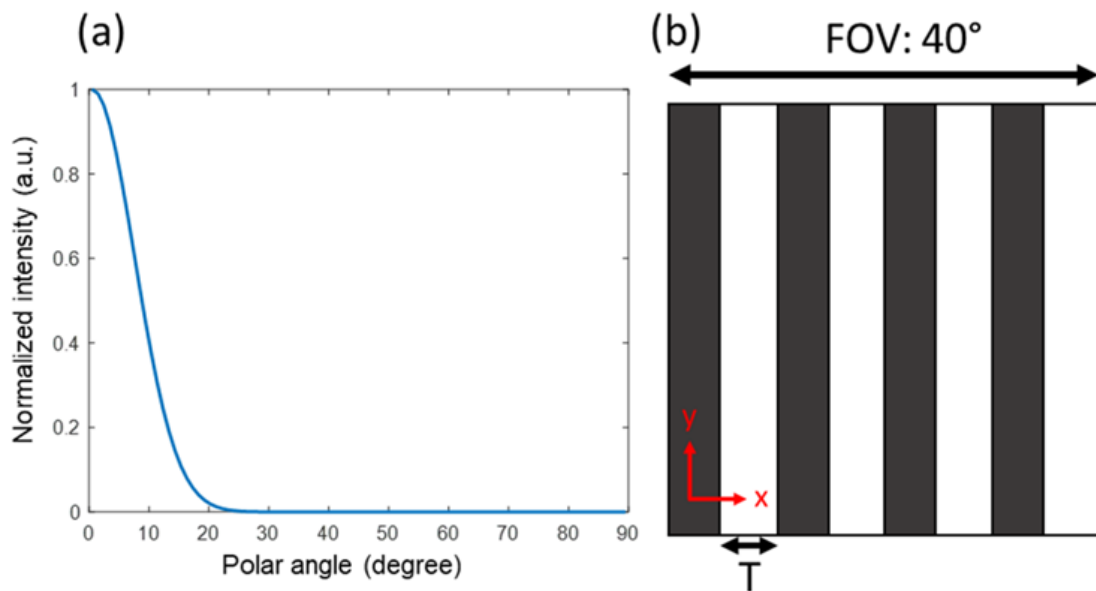
Figure 3-4 (a) Directional radiation pattern of the light engine. (b) Test pattern with various resolution density: T = 500μm, 200μm, 100μm, 40μm, and 20μm, and the size corresponding to 40° FOV.

Moreover, to evaluate the image quality of a VR system, the test patterns with frequency of [0.38, 0.95, 1.9, 4.75, and 9.5] cycles per degree (cpd) is displayed by the light engine. The corresponding linewidth (T) of each resolution pattern on the display is 500μm, 200μm, 100μm,

40µm, and 20µm, respectively, and the pattern size is 40° FOV as Fig. 3-4(b) depicts. To support a 20-µm line width, the resolution density of the microdisplay should be higher than 1270 ppi.

3.4 Results and Discussion

Figures 3-5 and 3-6 illustrate the intensity distribution on the receiver for different test patterns analyzed by the optical model shown in Fig. 3-1(a). Because the test pattern only varies along x-axis but remains uniform along y-axis [Fig. 3-4(b)], the intensity distribution is averaged along y-axis. We plot the average intensity distributions on linear and logarithmic scales in Figures 3-5 and 3-6, respectively. Logarithmic scale images help illustrate the intensity distribution at low intensity levels. Therefore, the effects of stray light are more easily observed. Figure 3-5(a), (b), (c), (d) and (e) correspond to different pattern frequencies. Additionally, the bin ranges on the receiver are -1000 bins and 1000 bins, corresponding to the viewing angle ranges of -10° and +10°. In another word, 2000 bins correspond to a FOV of 20° (one bin: 0.01°). Let us first focus on the results for a perfect dark-state panel (e.g., OLED or micro-LED) whose image degradation is caused only by the imaging optics. For the low frequency test patterns (0.38, 0.95 and 1.9 cpd), the pattern remains clear over the entire receiver area. The image contrast degradation is mainly caused by the stray light from the imaging optics. In these figures, the dark state ranges from 0.001 to 0.003, depending on the location. To clearly demonstrate the dark-state variation, Fig. 3-6(a), (b), (c), (d) and (e) depicts the average intensity distribution on the receiver in a logarithmic scale. This stray light sets the upper limit for the device contrast ratio to be about a few hundreds to one, even when the dark state of display is perfectly black. The contrast variation is mainly determined by the stray light distribution on the receiver. As the test pattern frequency increases (4.75 and 9.5

34

cpd), the patterns from large viewing angles are merged so that the image contrast decreases. Therefore, image contrast gradually decreases with increasing viewing angle. The maximum image contrast in the center view is about 300:1 (4.75 cpd) and 50:1 (9.5 cpd). Under the high-frequency pattern, we notice that the image contrast is mainly determined by the aberration of the imaging optics. At larger viewing angles, the widened PSF caused by aberration severely reduces the image contrast. Under such condition, the stray light no longer makes a significant impact on the image contrast. Overall, for low-frequency target images, the image quality is mainly affected by the stray light from the imaging optics. By contrast, for high-frequency target images, the image quality is mainly degraded by the aberration of the imaging optics.
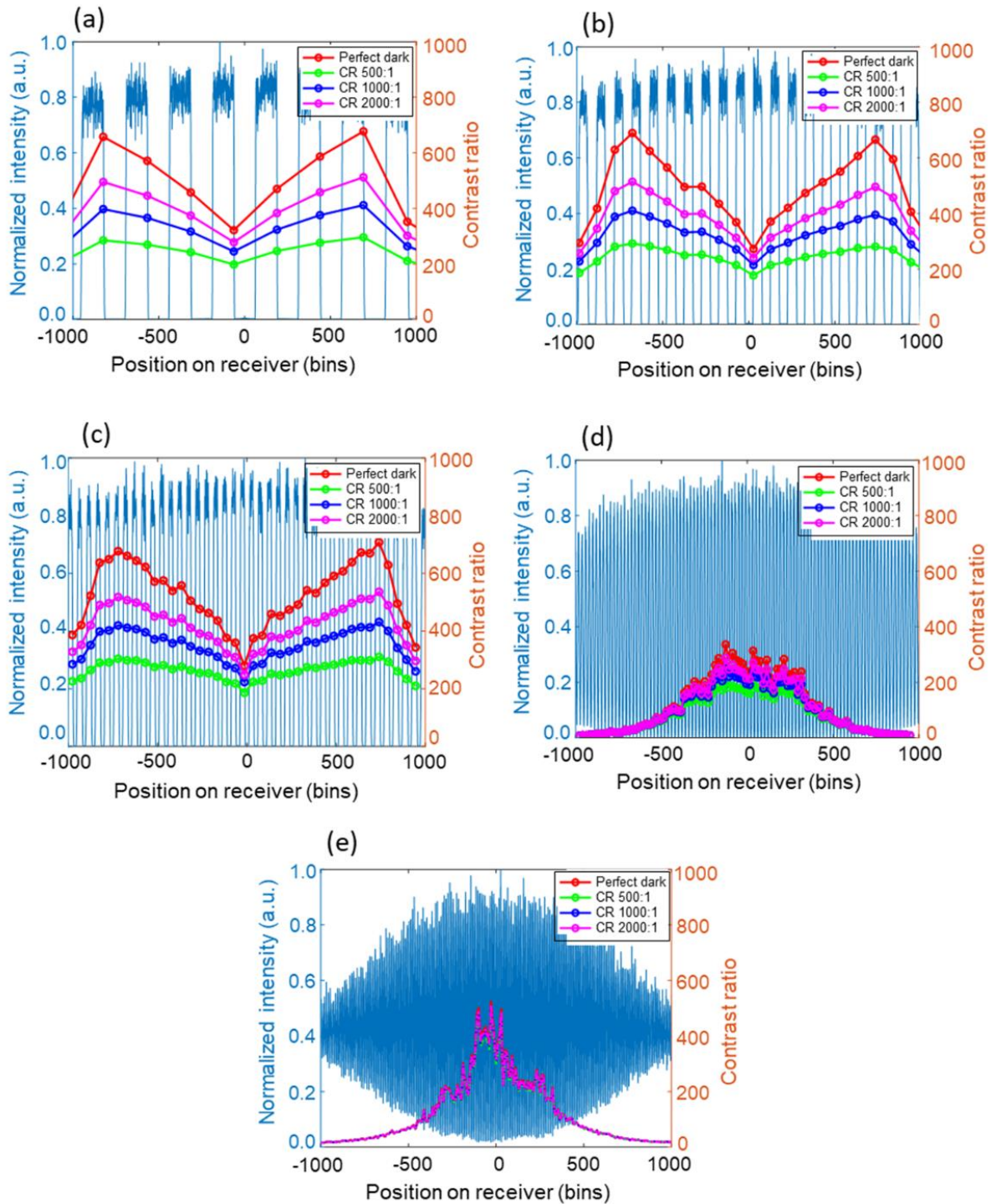
Figure 3-5 Illuminance distributions in linear scales of test patterns with resolutions of (a) 0.38 cpd, (b) 0.95 cpd, (c) 1.9 cpd, (d) 4.75 cpd, and (e) 9.5 cpd. The corresponding contrast ratio distributions of display light engines with various contrast ratios are also plotted.

36
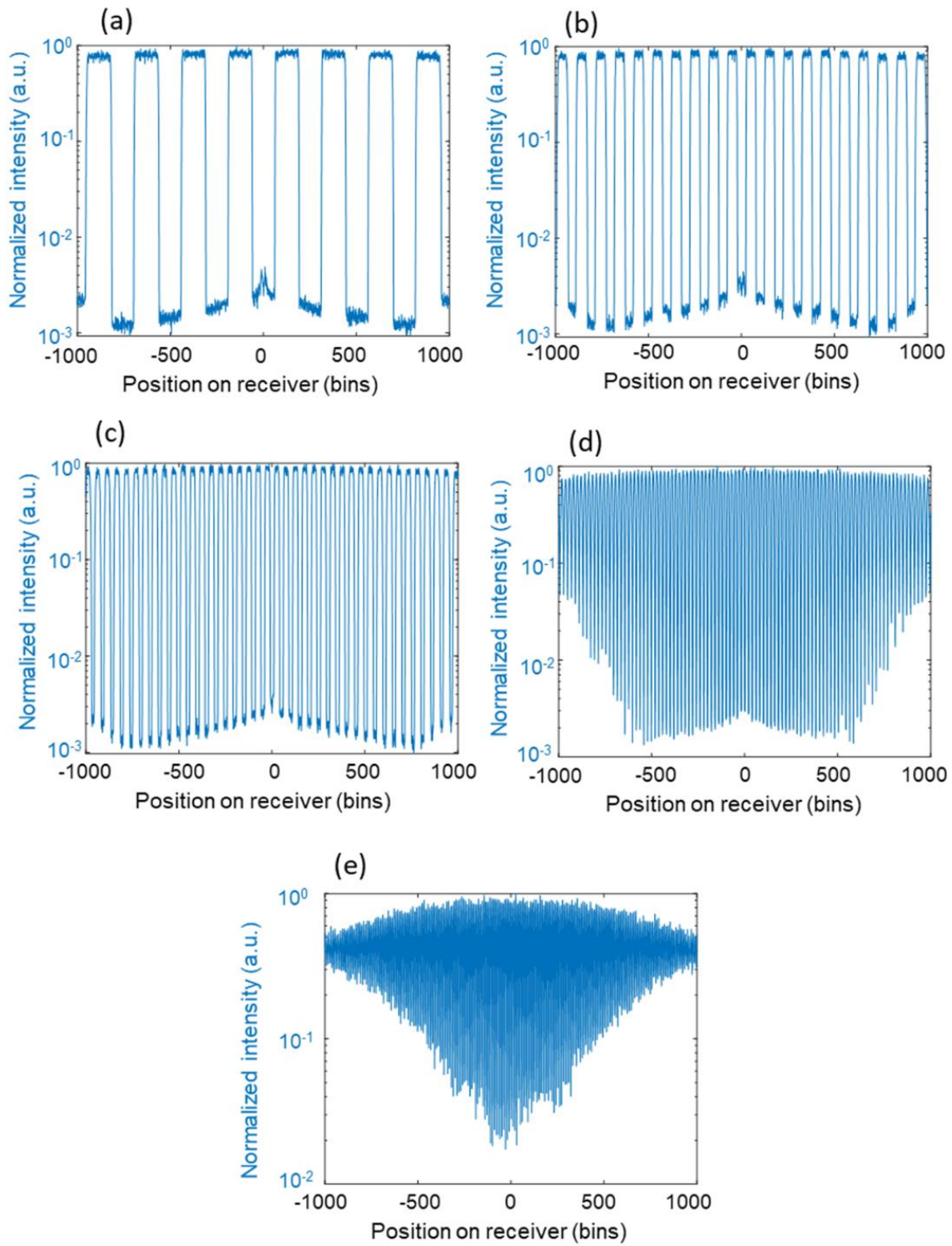
Figure 3-6 Illuminance distributions in logarithmic scales of test patterns with resolutions of (a) 0.38 cpd, (b) 0.95 cpd, (c) 1.9 cpd, (d) 4.75 cpd, and (e) 9.5 cpd.

Display artifacts, such as light leakage from the LCD, are also considered in the simulation. Figures 3-6(a), (b) and (c) illustrate that the light leakage from LCD is comparable to (or even weaker than) the intensity of stray light (0.001 to 0.003). Therefore, compared to an OLED display with a perfect dark state, as shown in Fig. 3-5(a), (b), and (c), the imperfect display contrast only reduces the peak image contrast by [43%, 60%, 80%] for an LCD with CR= [500:1, 1000:1, 2000:1], respectively. Moreover, boosting display contrast by 4x, e.g., from 500:1 to 2000:1, only improves the image contrast by 1.8x. In other words, due to the disturbance of stray light, simply increasing the display contrast cannot achieve the expected high-contrast image, i.e., the benefit of increasing display contrast is limited. For high-resolution patterns, the image contrast degrades severely because the aberration leads to pattern merging as shown in Fig. 3-6(d), and (e). Under this condition, display artifacts do not cause a significant reduction in image contrast. Additionally, the aberration of the imaging optics limits the maximum resolvable density of light engines to ~9.5 cpd, which corresponds to 1270 ppi for the microdisplay. Therefore, the benefit to further increase the display's resolution density is not obvious in our pancake VR device. It is worth noting that the optical resolving power of the VR imaging optics depends on the lens design. Some two-lens or three-lens designs may offer a higher optical resolving power and thus shall require a higher resolution density display.

Recently, using mLED backlight to achieve high dynamic range for LCDs has attracted much attention. However, how to design the number of local dimming zones remains unclear. Here, based on the above analysis, we plot the image contrast under normal view as a function of pattern frequency, as shown in Fig. 3-7. Notably, the lowest pattern frequency is as low as 0.0475 cpd. Same as the above analysis, for high-frequency patterns (>5 cpd), the aberration of the VR device

is the dominant factor affecting the image contrast. Regardless of the display performance, the image contrast is almost the same because the aberration of the VR device results in pattern merging. For the frequency ranging from 0.1 cpd to 5 cpd, stray light is a major contributor to the decreased image contrast and there is no noticeable gain in increasing the display contrast. For low-frequency patterns (<0.1 cpd), the intrinsic contrast of the microdisplay becomes the dominant factor affecting the image contrast. A high contrast microdisplay significantly improves the image contrast of a VR device. From a mLED backlight design perspective, the smaller local dimming zone size support a higher frequency pattern with a higher display contrast. On the other hand, a larger local dimming zone size only support lower frequency modes with a high display contrast. Based on above discussion, it is not helpful to apply extremely small-sized local dimming zones to support high-frequency test patterns with a high display contrast. This is because the image contrast of a VR device for high-frequency image contents is primarily determined by the optical properties of the imaging optics (stray light and aberration of imaging optics). A high display contrast helps improve the VR image contrast when the pattern frequency is low. As Fig. 3-7 shows, when the test pattern frequency is between 0.1 cpd and 0.0475 cpd (pink region), a higher display contrast ratio makes a more noticeable contribution to the VR image contrast. The 0.1-cpd and 0.0475-cpd test pattern frequency corresponds to 2-mm and 4-mm width in the microdisplay, respectively. Therefore, considering a 40-mm x 40-mm microdisplay supporting a 100° FOV, the desired local dimming zone number is about 400 (20×20) to 100 (10×10), depending on the intrinsic LCD contrast. For an LCD with CR≥2000:1, the image contrast is comparable to an OLED display with a perfect dark state, even with test patterns frequencies as low as 0.1 cpd. Therefore, we only require about 100 (10×10) local dimming zones to see a significantly improved

image contrast when the frequency is below 0.1 cpd. On the other hand, for an LCD with CR = 500:1, the image contrast at a frequency of 0.1 cpd is noticeably different from that of an OLED display. Thus, about 400 (20×20) local dimming zones would be required to improve the image contrast of test pattern with 0.1-cpd frequency. This value is close to that of commercial product such as Meta Quest Pro, which has about 500 mLED local dimming zones.

Further subjective experiments or human visual models which take the contrast sensitivity function of HVS into consideration are essential to determine the indistinguishable image contrast difference. In the above simulation, the test pattern has an average picture level (APL) of 50% (half the pixels on and half off) and a size range of 40° FOV. In practice, the severity of stray light depends on the APL of the image content. When more pixels are turned on, the adjacent pixels receive more stray light, which in turn reduces the image contrast. Moreover, the birefringence of the lens is not considered in our simulations [61]. Therefore, further comparisons between the simulation results and physical experimental results are necessary.
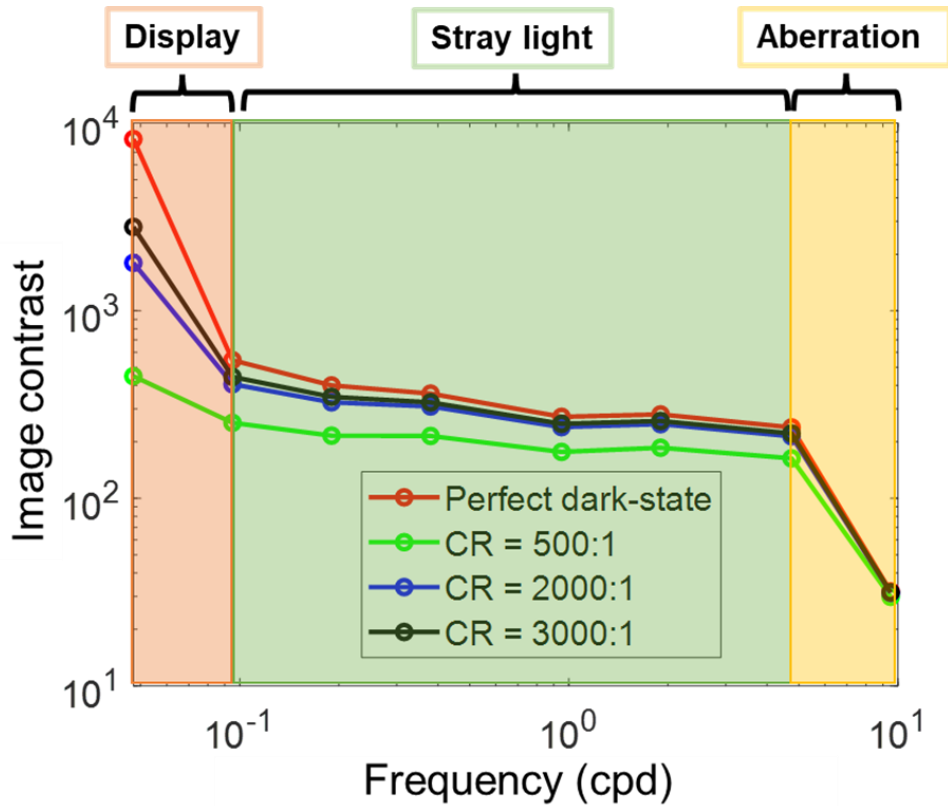
Figure 3-7 Simulated image contrast of a VR device of test pattern with different frequency (0.0475 cpd to 9.5 cpd). Aberrations, stray light, and display contrast mainly determine image contrast for high-frequency (>5 cpd), mid-frequency (>0.1 cpd and <5 cpd), and low-frequency (<0.1 cpd) image content, respectively.

3.5 Summary

In this chapter, we evaluate the image degradation of VR devices caused by both imaging optics and the light engine and found that the stray light and aberrations of imaging optics lead to non-negligible image degradation. The image contrast of fringe patterns at different frequencies is used as an evaluation metric. In a VR system, the aberration of imaging optics limits the maximum resolvable density of light engines, and the existence of stray light, although undesirable, sets the upper limit for the device contrast ratio. Furthermore, because enhancing the display contrast only significantly improves the image contrast of low-frequency contents (<0.1cpd), when applying

mLED backlight to the LCD light engine, the size of the local dimming zone does not need to be very small. It just needs to be properly sized (around 2-mm to 4-mm wide, depending on the intrinsic LCD's contrast ratio) to improve the image contrast of low-frequency patterns. Overall, our system analysis suggests that to prevent excessive design, the requirements of light engines should not be designed according to the HVS, but rather based on the employed imaging optics of the VR devices.

CHAPTER 4: HIGH-EFFICIENCY QD-µLED LIGHT ENGINE

The content of this chapter was previously published in [62].

4.1 Background

Micro-LED (µ-LED) with a perfect dark state and high peak brightness has become a promising light engine candidate for HDR near-eye displays [63,64]. However, because of the high-resolution density requirements, the conventional mass transfer methods used for direct view red, green, and blue (RGB) micro-LED large screen displays are not suitable [65–67]. To improve the resolution density of µ-LED displays, two methods have been proposed to assemble the backplane driver circuitry and LED array: flip-chip bonding and wafer bonding [68,69]. For flip-chip bonding, the µ-LED is fabricated on the LED substrate, and the metal bonding ball is prepared on the complementary metal-oxide semiconductor (CMOS) substrate. Two wafers are then aligned and bonded using thermal-compression method, but the pixel size is limited to around 10 µm with this method. For the wafer-bonding type, the LED epi is firstly bonded to the silicon driver and µ-LED is directly fabricated on the CMOS wafer, eliminating the need for alignment during the bonding process. The pixel size can be reduced to less than 5 µm. While these methods can achieve high-resolution densities, the displays are usually monochromic. To obtain full-color displays, an x-prism or other optical design is required to combine the RGB colors from three separate micro-LED panels. However, additional optical elements increase the size of the light engine and are not suitable for the compact near-eye displays.

To address these problems, assembling a blue µ-LED array with a color conversion layer has been proposed. The blue light emitted by the µ-LED array excites the color conversion materials,

such as phosphors, quantum dots (QDs), or perovskite nanocrystals, to produce vivid colors [70–72]. However, the blue light leakage, low color-conversion efficiency (CCE), and optical crosstalk are still problematic [62,73–75].

4.2 Color-converted micro-LED display

Figure 4-1 shows the device structure of the proposed color-converted micro-LED display. It consists of a blue micro-LED array at the bottom, an adhesion layer, a patterned color-conversion film, a patterned CLC film, and a top color filter array to form RGB sub-pixels. The blue LED array is protected and planarized by black photoresist to prevent lateral leakage of blue light [76,77]. The blue light emitted from the top passes through the adhesion layer and is down-converted into green and red lights by the QD or perovskite material. Afterward, the leaked blue light is recycled by the patterned CLC to improve color conversion efficiency. Here, a CLC film with opposite handedness is assembled to recover the unpolarized leakage light from blue micro-LED. Finally, the color filters are aligned with the RGB sub-pixels to absorb the rest blue light and prevent ambient light excitation. To evaluate the improvement resulting from adding a patterned CLC film to the display system, the device performance without such a CLC film is also analyzed below. In the following, we set the sub-pixel size as 100 μm×200 μm and the LED chip size as 50 μm×100 μm. To analyze the severity of optical crosstalk, the employed adhesion layer is in the 20 μm to 60 μm range.
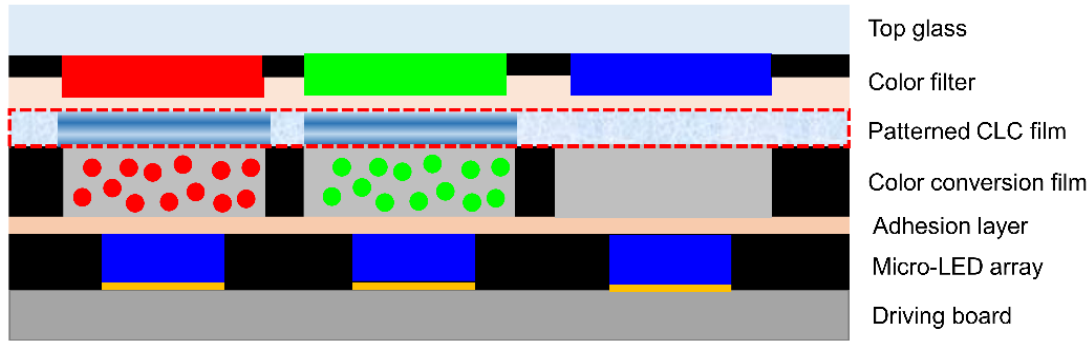
Figure 4-1 Device configuration of the proposed color-converted micro-LED display.

We use ray tracing software (LightTools) to simulate the performance of our proposed display system. The emission spectrum of the blue LED is shown in Figure 4-2(a), and its optical performance will be analyzed later. The photoluminescence characteristics of QD are simulated by Advanced Physics Module in LightTools. The absorption and emission spectra of green perovskite nanocrystals and cadmium-based red QDs are also plotted in Fig. 4-2(a) [78,79]. In our model, the mean free path is the average length of ray propagation before impacting QD particles, which is used to express the concentration of the color conversion film. Due to the photolithographic fabrication process, the color conversion film thickness is limited to 5-9 µm [80]. A thicker QD film would reduce the blue light leakage, but the self-absorption effect is also more pronounced. The photoluminescence quantum yield (PLQY) of our perovskite film is 0.7, and the refractive index of the color conversion film is 1.5. In addition, two types of color filters (CFs) are used in our simulation, and their transmission spectra are shown in Fig. 4-2(b). Compared to CF1, CF2 provides a wider color gamut, but at the expense of lower optical efficiency.
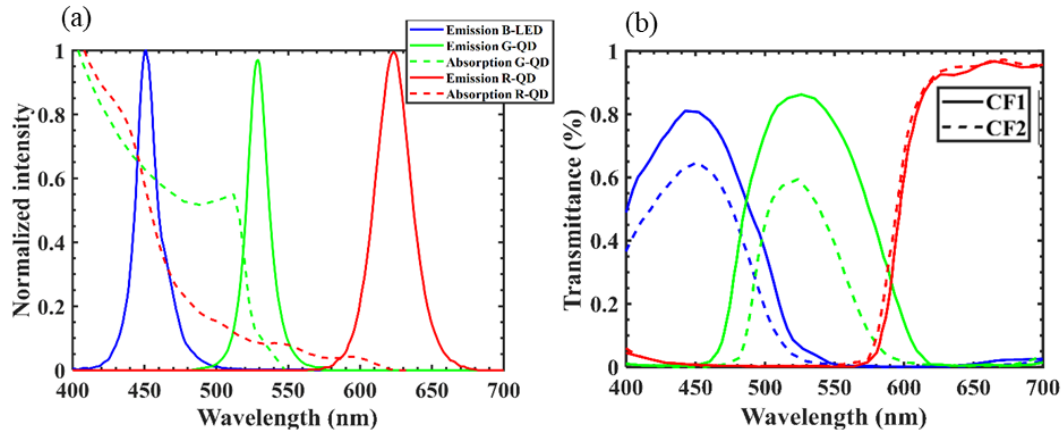
Figure 4-2 (a) Emission spectrum of the blue micro-LED; absorbance (dashed lines) and photoluminescence spectra of green perovskite nanocrystal and red QD. (b) Transmission spectra of color filters CF1 and CF2.

4.3 Patterned CLC polymer film

The fabrication process of patterned CLC film is illustrated in Fig. 4-3. In experiment, we prepared a CLC precursor consisting of 92.95 wt.% reactive mesogen RM257 (from HCCH) as LC monomer, 2.8 wt.% S5011 or R5011 chiral dopants (from HCCH), 4 wt.% of photo-initiator Irgacure 651 (from BASF), and 0.25 wt.% of surfactant Zonyl 8857A (from DuPont). First, we spin-coated a thin Brilliant Yellow (BY) photo-alignment layer on a clean glass substrate, and then illuminated it by a blue laser (λ=450nm) to create the alignment pattern. Next, we spin-coated the CLC precursor on top of the BY layer to replicate the alignment. In our design, in order to reflect blue light, the helical pitch length of the CLC is set at ~298 nm and the film thickness is about 8 helical pitches to establish Bragg reflection. Then, we conducted the patterned UV curing process to create two different textures on the CLC film. The photo-polymerization process was only carried out in the transparent area to form a stable polymer film (P-CLC). After that, the sample was heated to 140°C, and the CLC material in the unexposed area (FC-CLC) became isotropic.

46

Last, the cooling process and UV curing were performed simultaneously. During the cooling process, the LC changed from isotropic back to cholesteric, and the arrangement was completely random.
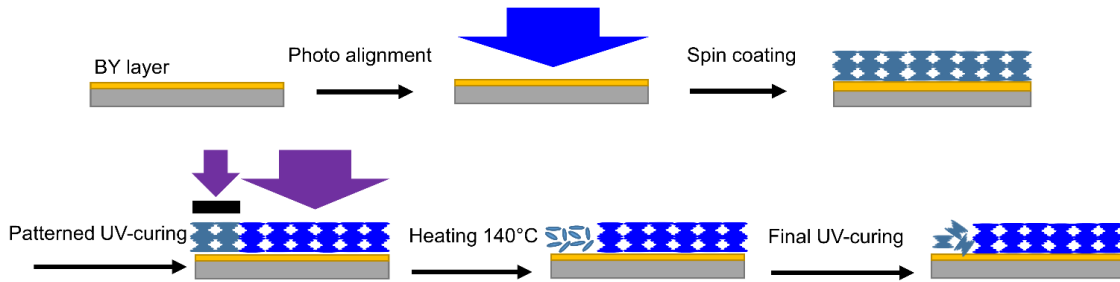
Figure 4-3 Fabrication process of the proposed patterned CLC film.

Figure 4-4(a) depicts the transmission spectrum of the film's planar and focal conic texture measured by a circularly polarized light having the same chirality as the CLC film. In addition, several kinds of patterned CLC films with different feature sizes were produced to prove that they can meet different display applications. Figure 4-4(b) shows some photomicrographs of patterned CLC films with feature sizes of 10 µm, 20 µm, 40 µm, and 80 µm.
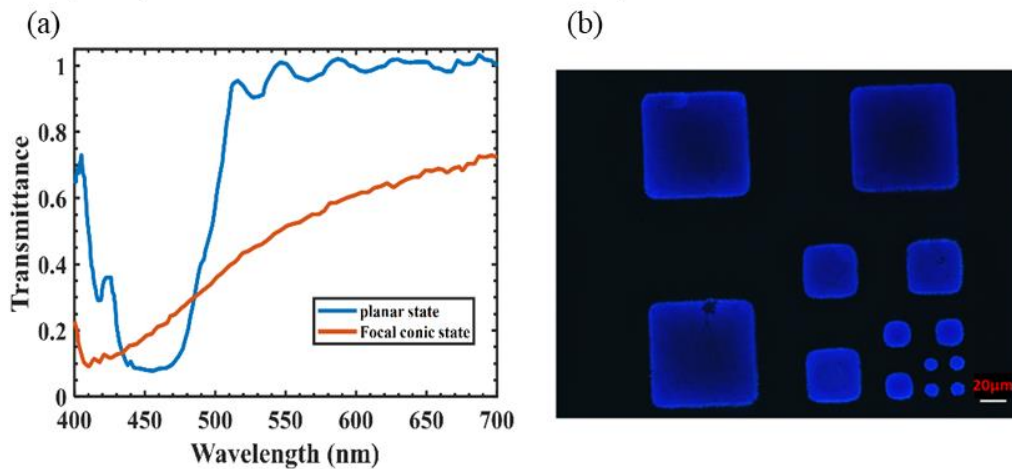
Figure 4-4 Measured transmission spectra of the planar state and the focal-conic texture on a patterned CLC film. (b) Microscope images showing a patterned CLC film with 10-µm, 20-µm, 40-µm, and 80-µm feature sizes.

In addition, we also simulated the optical performance of the patterned CLC films [81] fabricated using a high birefringence (Δn) LC monomer (for example, Merck RMS16/091, $\Delta n = 0.3$ at $\lambda=450$ nm). Such a high Δn material helps to broaden the reflection band of the P-CLC film. Here, we name the film made with $\Delta n = 0.3$ as the wide-band (WB) CLC film, and the film made with RM257 LC monomer as the narrow-band (NB) CLC film. The average reflectance of the P-CLC film in the blue spectral region can be calculated by the following formula:

$$R_\theta = \frac{\int S_{LED}(\lambda) \times R_{CLC}(\lambda,\theta)d\lambda}{\int S_{LED}(\lambda)d\lambda}$$

$$(4\text{-}1)$$

where S_{LED} is the spectral power density of blue light emitted by the micro-LED, and R_{CLC} is the reflection spectra of CLC film at different incident angles.

Based on Eq. (1), the average reflectivity of the WB- and NB-CLC films as a function of incident angles is plotted in Fig. 4-5(a). On the other hand, in the FC-CLC segment, the tiny multi-domain CLCs with random distribution scatter the incident light. The total transmittance is about 95%, and its angular transmission profile is plotted in Fig. 4-5(b). Unlike the reflection band of P-CLC, which exhibits a strong polarization selectivity, the scattering property of FC-CLC is polarization independent. The measured optical properties of the patterned CLC film will be further applied in our LightTools model to evaluate the display performance of color-converted micro-LED display integrated with the CLC film.
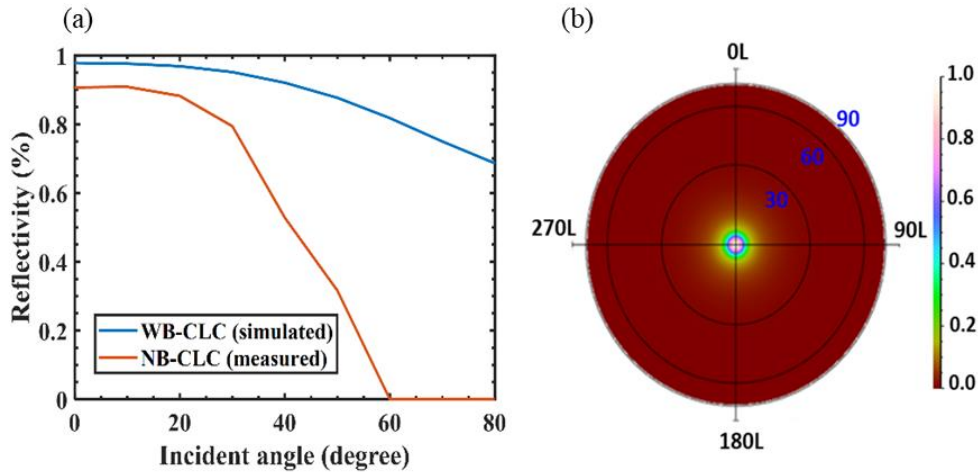
Figure 4-5 (a)Average reflectivity of WB and NB P-CLC films in the blue light spectrum (micro-LED) at different incident angles (in air). (b) Measured angular transmission profile of the focal conic CLC film at normal incidence.

4.4 Blue micro-LED array

The device structure of the thin-film flip-chip LED is shown in Fig. 4-6(a). It consists of a metal mirror with high reflectivity, a p-GaN layer (about hundreds of nanometers), a multiple quantum well (MQWs) layer (about 100 nm) and an n-GaN layer (about a few microns). For the emission source, due to the valence band characteristics of GaN, anisotropic InGaN emission with the dipole axis parallel to the crystal C plane (only in-plane dipole) is considered [82]. The light intensity of the TM component is much smaller than that of the TE component [83]. The direction of light emission and the polarization vector can be represented by the azimuthal angle φ and the polar angle θ shown in Figure 4-6(b). The electric field of p is in the same plane as the c-axis and the direction of emitting ray. On the other hand, the electric field of s oscillates vertically to this plane and the electric field of p. The main TE component produces a light source consisting of s-polarized component and $\cos^2 \theta$ of the p-polarized component, as shown in Fig. 4-6(c) and 4-6(d) [84].

49
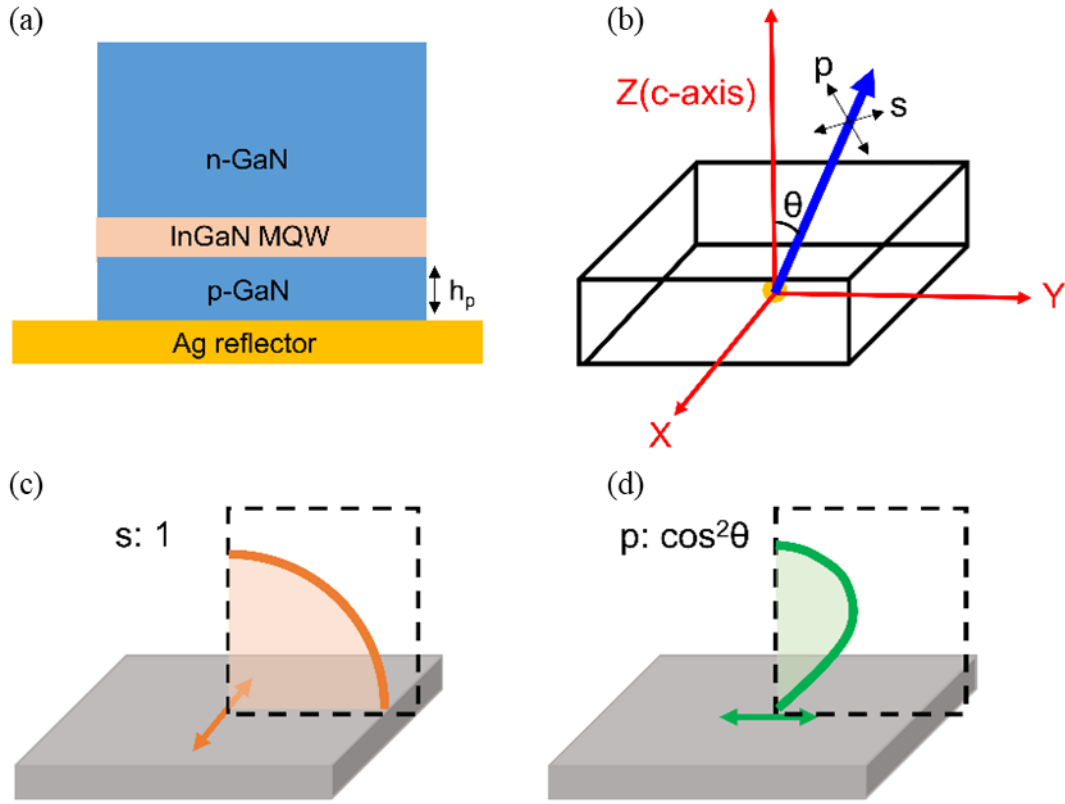
Figure 4-6 (a) Schematic design of micro-LED chips considered in this study. (b) Schematic diagrams of coordinate system in simulation and measurement. The angular distributions of (c) s-polarized component and (d) cos²θ of the p-polarized component.

Since the emitted MQW layer is close to the bottom mirror, the interference between the dipole source and the reflected light from the bottom mirror will form a high and low intensity area. The radiation pattern inside the LED chip varies with the thickness of the p-GaN layer. Here, the radiation pattern is simulated by the FDTD method and the theoretical interference numerical equation. In both methods, the half-cavity approximation is applied [85]. The refractive index of GaN is 2.45, and Ag is 0.14 + 2.47i, so the reflectivity between p-GaN and Ag is about 90%.

Based on the interference theory, the radiation pattern can be described as:

$$\left| E_{total} \right|^2 = E_0^{\ 2} + E_r^{\ 2} + 2E_0 E_r \cos(\Phi_1 + \Phi_2) \tag{4-2}$$

where E_0 is the amplitude of the emitted light, E_r is the amplitude of the reflected light, Φ_1 is the phase shift due to optical path difference, and Φ_2 is the phase shift resulting from mirror reflection.

According to the light polarization (*s* or *p* polarization) and the material's refractive index, the phase shift at a specular reflection can be calculated by the Fresnel reflection theory. On the other hand, the phase shift caused by the optical path difference can be obtained by the following formula:

$$\Phi_1 = 2\pi \times \frac{(2 \times h_p \times \cos(\theta))}{\lambda_n}$$

(4.3)

where h_p is the thickness of p-GaN, θ is the polar angle, and λ_n is the effective wavelength.

For the FDTD method, the simulated LED structure is shown in Figure 4-7(a). Two dipoles aligned along *x* and *y* axes, corresponding to the s and p polarizations are simulated, respectively. In Figure 4-7(b), the radiation pattern of p-GaN with a thickness of 100 nm simulated by the FDTD model is shown as dotted lines, and the radiation pattern calculated by the theoretical interference equation is drawn with a solid line. The agreement between these two methods is very good. In the following paragraph, the influence of p-GaN thickness on optical crosstalk will be analyzed.
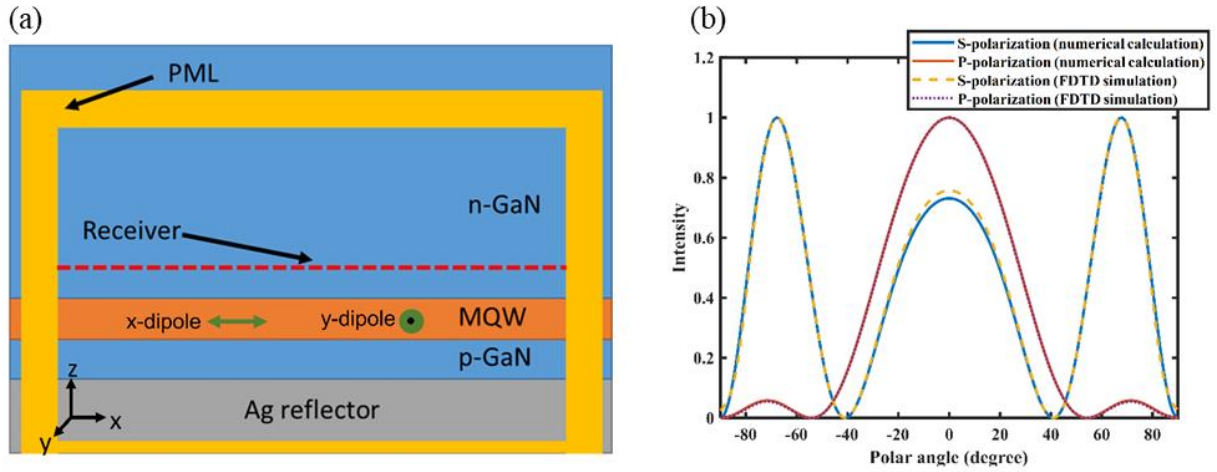
Figure 4-7 (a) Schematic diagram of the simulated LED structure in FDTD simulation (half-cavity approximation is applied). (b) Simulated angular distribution inside the GaN LED by the FDTD model and by the interference theory (h_p = 100nm).

4.5 Simulation results and discussion

Based on the above methods, we analyzed the radiation patterns of thin-film flip-chip LEDs with various p-GaN thicknesses (175 nm, 200 nm, 210 nm, 225 nm, 250 nm and 275 nm) and results are shown in Fig. 4-8. Then, the angular distribution is imported into the ray tracing model in Monte Carlo LightTools to analyze the light extraction efficiency (LEE) of the blue LED array. Since the LED chip is surrounded by a black photoresist with a refractive index of 1.5, the light extraction cone (±38°) is limited to the top surface of the LED. Figure 4-8 illustrates that with various thickness of p-GaN layer, the radiation pattern and LEE is changed periodically. The relatively high LEE region ($\geq$ 30%) occurs when the p-GaN thickness is at 210 nm, 225 nm, and 250 nm.

52
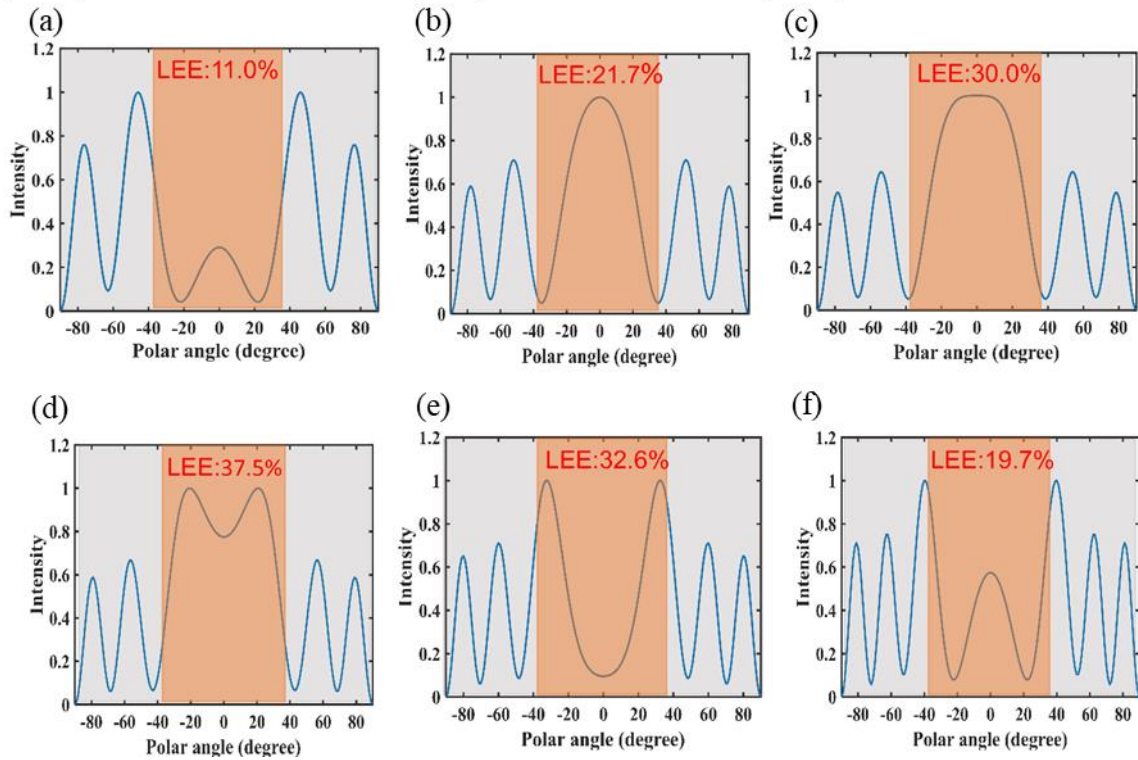
Figure 4-8 The angular distribution inside the GaN LED by the interference theory (a) $h_p =$ 175nm, (b) $h_p = $ 200nm, (c) $h_p = $ 210nm, (d) $h_p = $ 225nm, (e) $h_p = $ 250nm, and (f) $h_p = $ 275nm.

In addition to efficiency, optical crosstalk which could reduce the image quality is another key factor for micro-LED color conversion displays. Therefore, it is important to apply an appropriate thickness of p-GaN to achieve high LEE and small optical crosstalk. The angular distribution of the blue LED light incident on the color conversion film depends on the radiation pattern inside the LED and the light extraction cone at the interface between the LED and the resin. For example, when the thickness of p-GaN is 250 nm, the radiation pattern inside the LED has a peak intensity near the critical angle. Therefore, after the emitted light is refracted at the interface between the LED and the resin, the angular distribution inside the resin will have a strong intensity in large angle, which will cause severe optical crosstalk. Based on the device structure shown in Fig. 4-1, when the adhesion layer is 20μm, Figure 4-9 shows the optical crosstalk of micro-LED color

conversion displays with various p-GaN thicknesses (210nm, 225nm and 250nm). To assess how much blue light passing through adjacent pixels, we place the receiver on top of the adhesive layer (at the entrance of color conversion material). From Fig. 4-9(a), we can see that when the p-GaN thickness is 210nm, the smallest optical crosstalk occurs. In addition, a thicker adhesion layer also increases the optical crosstalk. Fig. 4-9(b) shows the optical crosstalk ratio as a function of adhesion layer thickness. Three micro-LEDs with p-GaN thickness (210nm, 225nm and 250nm) are analyzed. Taking the relatively large LEE (30.0%) and small optical crosstalk into consideration, the 210nm p-GaN thickness micro-LED is used in the following analysis.
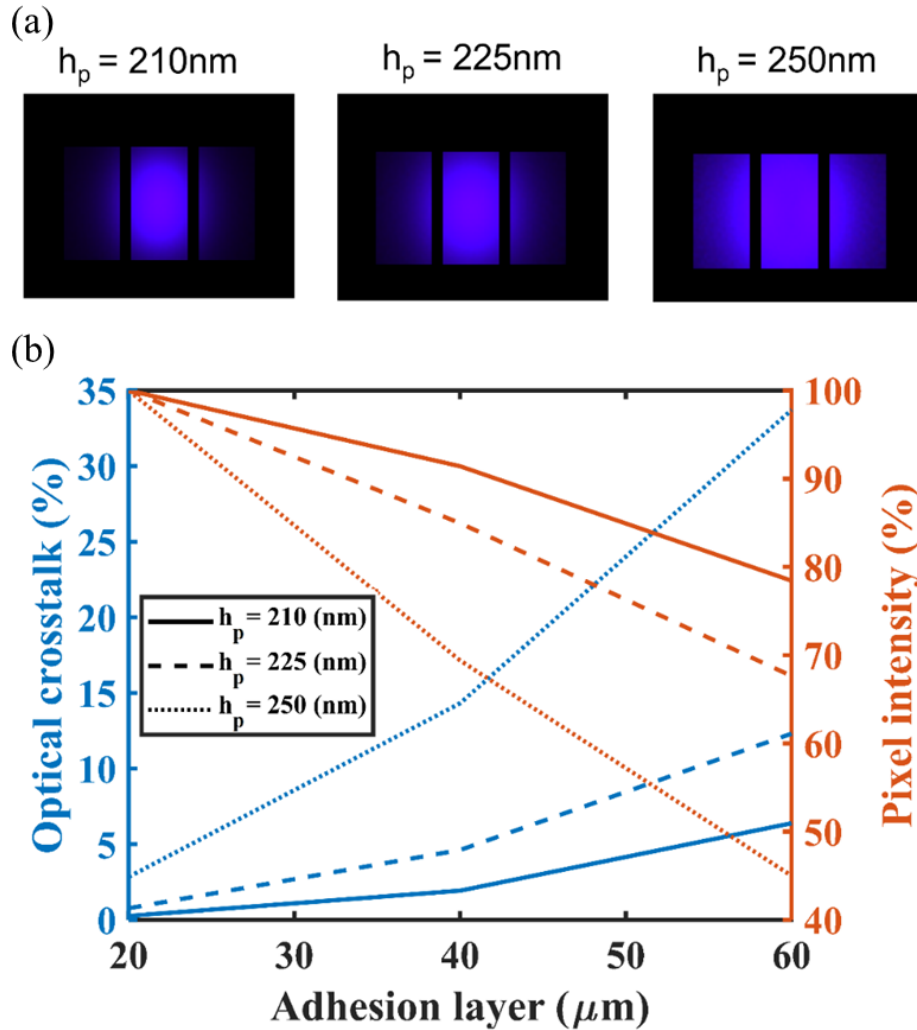
Figure 4-9 (a) Simulated color image at the top of adhesion layer (20µm). (b) Simulated optical crosstalk ratio as a function of adhesion layer thickness.

In this section, we evaluate the improvement in CCE and color gamut of our proposed patterned CLC film system relative to the control system. Four types of display systems are analyzed: 1) CF1 color filter only (control system), 2) CF2 color filter only (lower efficiency but wider color gamut), 3) Color filter (CF1) + CLC film (narrow-band), and 4) Color filter (CF1) + CLC film (wide-band). As described above, the P-CLC film can reflect the leaked blue light back to the color

conversion film, thereby increasing CCE. Generally, the more blue light leaks, the greater the improvement of the P-CLC film. Therefore, it is important to make the blue light leakage rate close to the practical value. Based on [86], we found that the blue light leakage rate of most QDCFs is ~20% to 40%. In our simulation model, we use these numbers to analyze the CCE enhancement caused by the patterned CLC film. Figure 4-10 depicts the spectral power distribution and display color gamut of four types of display systems when the blue light leakage rate is 40%. We first focus on the comparison of color conversion efficiency between different display systems. As described above, CF2, which has a lower transmittance than CF1, reduces the color conversion efficiency. In addition, for display systems with P-CLC films, narrow-band and wide-band CLC films lead to a CCE improvement of approximately 16% and 30%, respectively. Compared to the narrow-band CLC film, as shown in Fig. 4-5(a), the wide-band CLC film with a larger reflection band has better blue light recycling ability.

In terms of color performance, the narrower emission spectra of green perovskite nanocrystals and red QD materials are expected to provide a wider color gamut. However, due to the blue light leakage in the blue-green crosstalk area of CF1, the display color gamut is reduced to 77% of Rec. 2020. To solve this problem, a color filter (CF2) with less crosstalk between the blue and green channels can be applied to expand the color gamut. Compared to CF1, CF2 can expand the color gamut from 77% to 92% Rec. 2020. However, the average transmittance of CF2 in the emission spectrum of perovskite nanocrystals is only 54.5%. Such a low transmittance greatly reduces the CCE of the display system. On the other hand, the wide-band CLC film has a wider reflection band (410-490nm), which helps not only recycle the leaked blue light, but also reduce the crosstalk between the green and blue color filters. Thus, the color gamut coverage is expanded. In addition,

the wide-band CLC film can maintain high transmittance in the emission spectrum of the perovskite nanocrystals. As a result, by combining a high transmittance color filter (CF1) with a wide-band CLC film, a wide color gamut (89.5% Rec. 2020) and high CCE can be achieved simultaneously. In comparison with CF2, our newly proposed device structure can achieve a similar color gamut (around 90% Rec. 2020) but with a twice CCE. Table 4-1 summarizes the overall color conversion efficiency and color coverage of the four types of display systems.
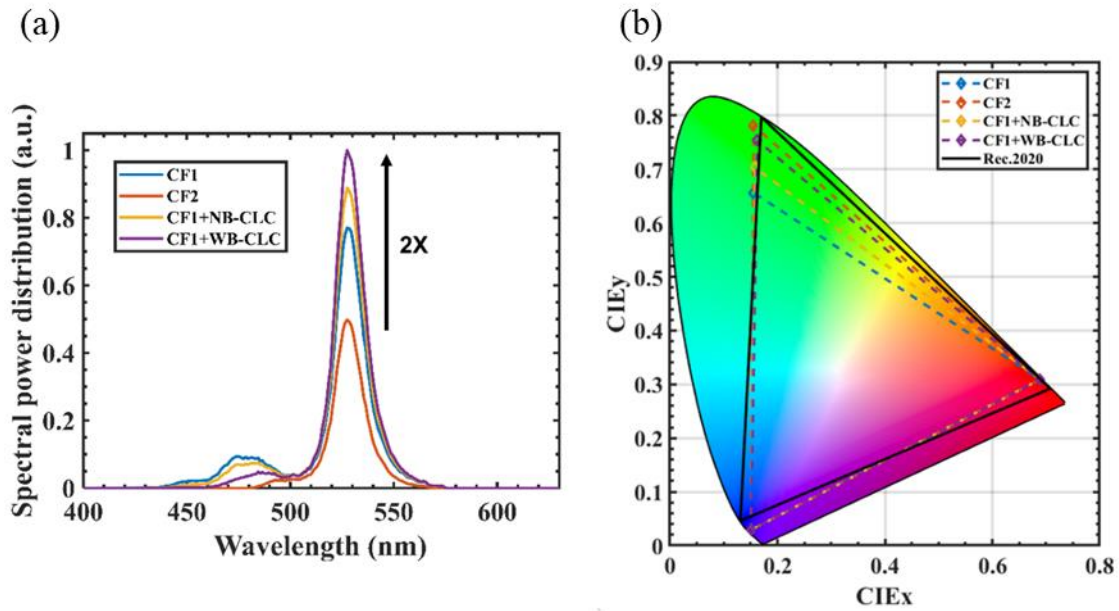
Figure 4-10 (a) Comparison of the spectral power distribution of the four specified display systems. (b) Simulated color gamut of the four display systems in Rec.2020 color space.

Table 4-1 Summary of normalized color conversion efficiency and color coverage of the four display systems studied.

	Intensity	Color coverage
	(Color converted)	(Rec. 2020)
CF1	77%	77.46%
CF2	50%	92.70%
CF1+NB-CLC	89%	83.22%
CF1+WB-CLC	100%	89.50%

4.6 Proof of concept experiments

Figure 4-11(a) illustrates the setup of our proof-of-concept experiment. In order to recycle the leaked blue light, two CLC films with opposite handedness is laminated on top of a CsPbBr3-polystyrene perovskite-polymer. Due to the limitations of our manufacturing equipment, in this experiment, the micro-LED array is replaced by an LED array. However, there are some differences between these two device structures. For example, the backward reflector at the bottom of the micro-LED, and the black photoresist to prevent lateral emission is not applied in the LED array. The radiation pattern of the LED array was measured by a goniometer (RiGO801 TechnoTeam Vision) and plotted in Figure 4-11(b). In addition, as shown in Figure 4-11(c), a CsPbBr3-polystyrene perovskite-polymer composite film with a center wavelength of 520 nm and a full width at half maximum (FWHM) of 21 nm was prepared by the swelling microencapsulation method [87]. A control measurement based on a glass substrate was also prepared to evaluate the effectiveness of the CLC film, and the blue light leakage rate of display system without CLC film

was measured to be 60%. Comparing the normalized emission spectra received by the fiber-optic spectrometer (Ocean Optics HR2000CG-UV-NIR) drawn in Figure 4-11(d) from the device structure with and without the CLC film, the CLC film improves the CCE of the color conversion film by about 43% (under 60% blue light leakage). In the measurement, a long pass filter (cut-off wavelength of 500 nm) was used as a color filter. It is worth noting that although the optical fiber can only receive the light emitted near the normal angle, according to the isotropic emission of the perovskite nanocrystal, the intensity increase ratio should be the same at all angles.
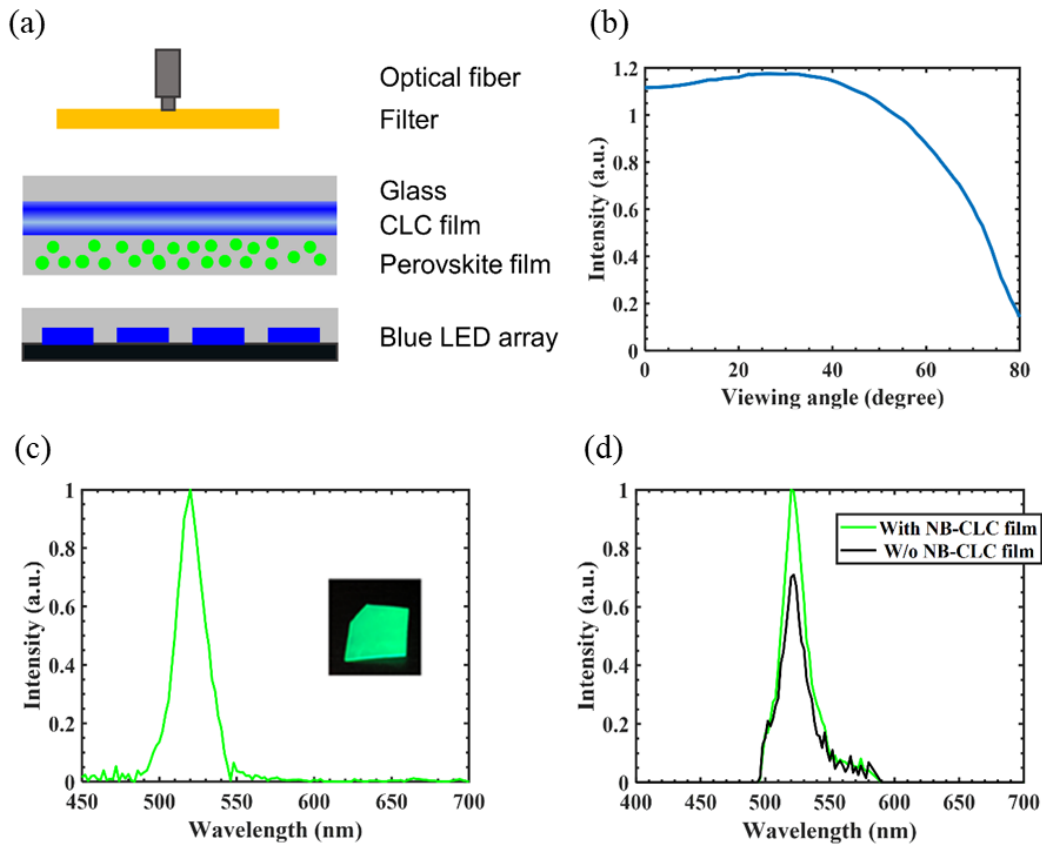
Figure 4-11 (a) Schematic diagram of the experimental setup. (b) Measured radiation pattern of the LED array. (c) Measured emission spectrum of the CsPbBr3 perovskite film. Inset: CsPbBr3 perovskite film under 365 nm UV light. (d) Measured emission spectrum of down-converted green light with and without the CLC film (filtered by the long pass filter with 500 nm cutoff wavelength).

Here, we only compared the results of the display system with and without NB-CLC film. The reflection band of the CLC film (not the WB-CLC film) was not optimized. In addition, as mentioned above there are some differences between the device structure of LED array and micro-LED array. Also, the insulating bank in not applied in the color conversion film. All these factors will affect the absolute improvement of CCE by adding CLC film. However, in this proof-of-concept experiment, we still observed that by assembling CLC films with opposite hands, the CCE of the color conversion micro-LED display system can be improved.

4.7 Summary

In this chapter, we have optimized the device structure of μ-LEDs to modulate the radiation pattern so that most of the emission light illuminates the targeted subpixels and reduces the optical crosstalk between subpixels. Additionally, we have proposed a patterned CLC film to recycle the leaked blue light and reduce the crosstalk of the color filters. We fabricated patterned CLC films without a vacuum fabrication process, with feature sizes ranging from 10 μm to 80 μm. For microdisplay applications (<5 μm), high-resolution photo-alignment equipment is required to further reduce the feature sizes. With above improvements, we have doubled the CCE of the display system and expanded the color gamut coverage to 90% Rec. 2020 compared to traditional color conversion μ-LED displays. We have also conducted a proof-of-concept experiment to verify the functionality of the patterned CLC film. Finally, our proposed methods, including patterning CLC thin films and optimizing LED device structure, can be extended to all kinds of color-conversion display systems, including color-converted μ-LED light engines for head-mounted displays.

CHAPTER 5: HIGH OPTICAL EFFICIENCY VR DEVICES

The content of this chapter was previously published in [30].

5.1 Background

High optical efficiency VR devices are critical for extending the operation hours so that the users do not need to frequently charge the device or connect a power cord while using it. The efficiency of a VR device mainly depends on two factors: the efficiency of the light engine and the coupling efficiency between the light engine and the imaging optics [30]. Numerous studies have been conducted to improve the light engine efficiency, such as enhancing the external quantum efficiency (EQE) of self-emissive displays [88,89], the CCE of color-converted displays [90,91], and the transmittance of light-modulating displays [92]. However, only a few studies have focused on the coupling efficiency of VR devices, and even fewer have considered both factors simultaneously. The coupling efficiency of a VR device indicates the ratio of the light emitted by the light engine to the light ultimately received by the viewer. Figure 5-1 illustrates the schematic of a VR display system. The light emitted from the display panel is initially refracted by a magnifying eyepiece and then reaches the eyebox. Due to its small etendue, only a small portion of the display light can reach the eyebox (highlighted in green), while the rest is either wasted or becomes stray light in the optical system (highlighted in gray) [93].
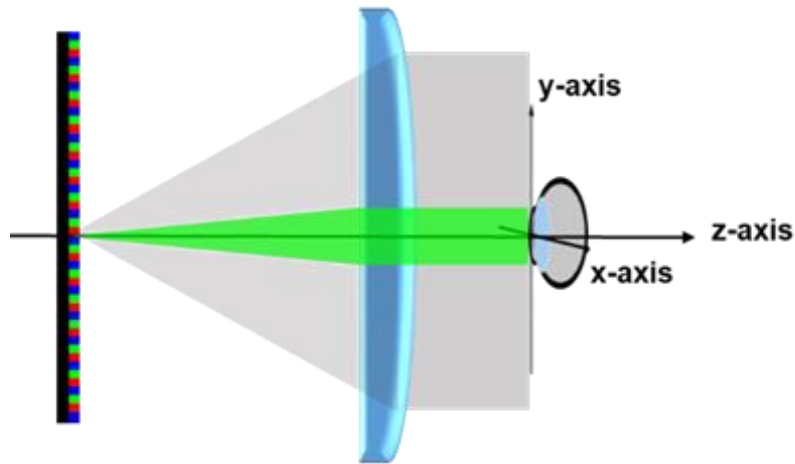
Figure 5-1 Schematic of VR devices consisting of a display panel, imaging optics and eye pupil.

A straightforward approach to improving the coupling efficiency of a VR device is to use a directional display, but it can have unintended side effects such as vignetting on projected virtual images and reduced optical efficiency on light engines. As shown in Figs. 5-2(a) and 5-2(b), because different pixels of the light engine have varying emission cone angles that can reach the eye pupil, the angular-dependent light leakage, intensity distribution, and emission spectrum of light engine cause both uneven brightness and color projected virtual image. Moreover, additional optical components, such as microlens arrays and prism films for LCDs and stronger microcavities for OLEDs, are required for generating directional emission displays, which typically reduce the optical efficiency of the light engine itself [94–96]. Therefore, it is essential to optimize the light engine structure for improving the optical efficiency of VR display without compromising the image quality.
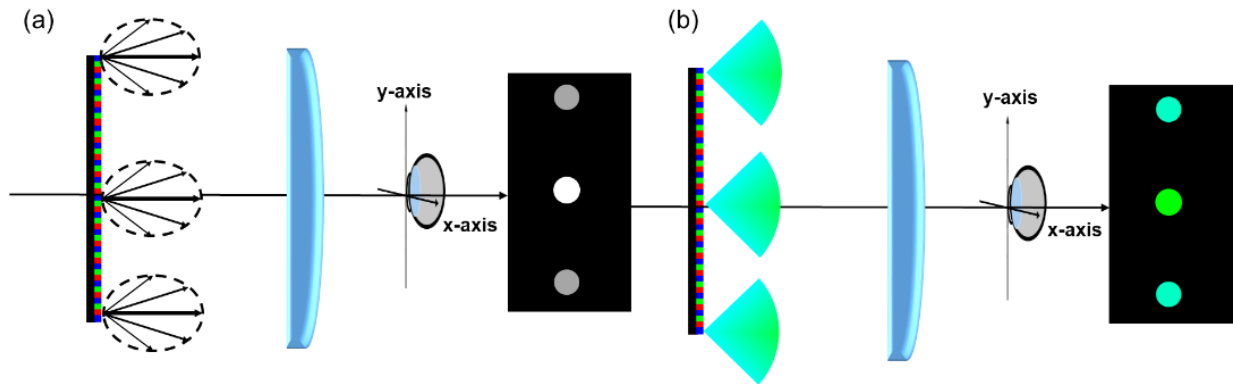
Figure 5-2 Schematic of (a) field brightness non-uniformity and (b) field color non-uniformity in VR. According to the pixel position (top, center, and down), three circles on the right of the figure represent the image received by the eye, respectively.

5.2 Device structure

Here, we focus on the lightweight VR system with a Fresnel lens [97]. The system consists of a flat panel display (OLED display or LCD), a Fresnel lens, and a receiver (circular eye pupil with a diameter of 4 mm). The raytracing model in the LightTools software is illustrated in Fig. 5-3(a). In the model, the Fresnel lens diameter is ~45 mm, the eye relief is ~15 mm, and the distance from display to the lens is ~35 mm. For the display, point sources are used to represent the pixels in the display panel. In addition, according to the circular symmetry of the VR system, we can simplify the display system in one direction. Therefore, 28-point sources with 1-mm pitch are built along the y-direction to represent the entire display system. In each point source, the total emission cone (polar angle (θ): $0°$ to $90°$; azimuthal angle (φ): $0°$ to $360°$) is divided into 91 units by the polar angle, with an interval of $1°$. Then, we sweep the polar angle of each point source from $0°$ to $90°$ to define the angular power collection efficiency of each cone unit. Results are plotted in Fig. 5-3(b). Again, the angular power collection efficiency ($C(\theta, y)$) is the ratio of power emitted from the point source to the power received by the receiver (eye pupil). As Fig. 5-3(b) shows, when the

point source is in the central area (y-position = 0), only the emission cone with a small polar angle

can reach the eye pupil. On the other hand, the emitted light from edge pixels reaches the eye pupil

through the emission cone with a larger polar angle.
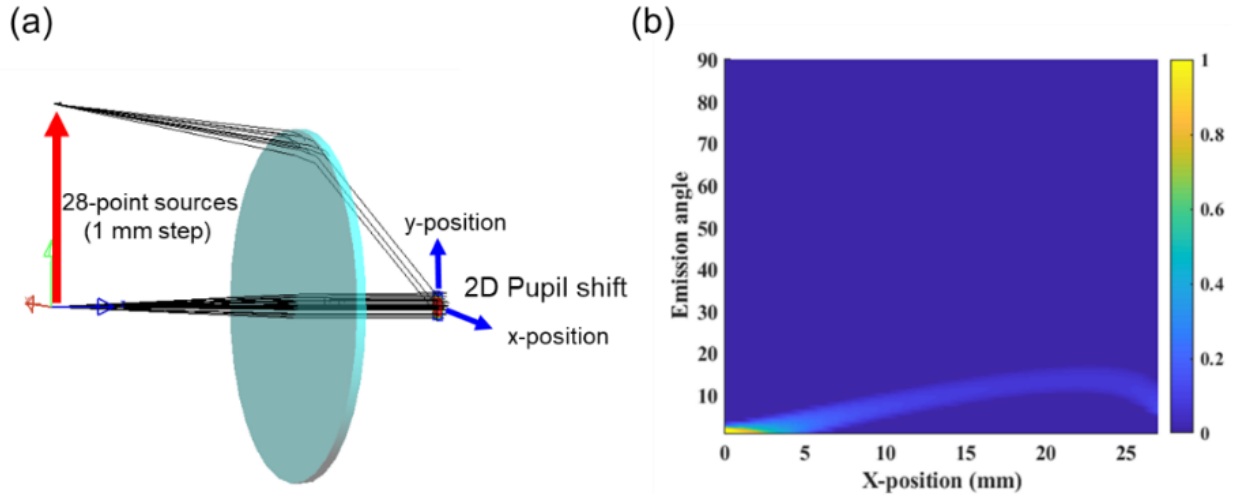
Figure 5-3 (a) Schematic of Fresnel VR system in LightTools. (b) Simulated angular power collection efficiency of the 28- point source in an VR system.

Based on the radiation pattern of the display and angular power collection efficiency of the

VR system, the power received by the eye pupil from different pixels can be defined as:

$$P_y = \int_{\theta=0}^{\theta=90} I(\theta) \times \Omega(\theta) \times C(\theta, y) d\theta, \tag{5-1}$$

and the optical system efficiency (OSE) of the VR system which is the ratio of total power received

by the eye pupil to the total power emission from the display can be further defined as:

$$OSE = \frac{\int_{y=0}^{y=27} \int_{\theta=0}^{\theta=90} I_{display}(\theta) \times \Omega(\theta) \times C(\theta, y) d\theta dy}{\int_{y=0}^{y=27} \int_{\theta=0}^{\theta=90} I_{display}(\theta) \times \Omega(\theta) d\theta dy}. \tag{5-2}$$

64

In Eq. (5-1) and Eq. (5-2), $I(\theta)$ is the angular distribution of the emission pixel, $\Omega(\theta)$ is the unit solid angle, and C (θ, y) is the angular power collection efficiency function of the VR system.

From Eq. (5-1), an effective method to improve the optical efficiency is to match the radiation pattern of each pixel with the angular power collection efficiency function of the VR system. Since the angular power collection efficiency function is concentrated in a small polar angle range, directional displays are widely used to improve the optical efficiency of the VR system. To generally explain the total light efficiency improvement in displays with various radiation patterns, we first use a point source with Lambertian radiation pattern and its exponentiation $I(\theta) = \cos^n(\theta)$ in the simulation model. In Sec. 5-3 and 5-4, when we optimize the OLED display and LCD, a realistic radiation pattern of the display will be applied. Here, the OSE of the VR system with various radiation patterns is normalized to the Lambertian emission panel. As Fig. 5-4 shows, the directional display can indeed improve the OSE of the VR system. However, in a real display panel, modulating the radiation pattern usually brings up some side effects. Taking an OLED display as an example, applying a strong microcavity to achieve a narrower radiation pattern may cause severe angular color shift and lower out-coupling efficiency. In addition, concentrating the backlight emission toward the normal angle may also lose the overall power efficiency of the LCD. Another side effect of applying directional display in an VR system is the uneven OSE in each pixel. As shown in Eq. (5-1), the OSE varies at different pixel positions. Therefore, a directional emission display may cause a large OSE difference between the center and the edge pixels, resulting in a vignetting effect.
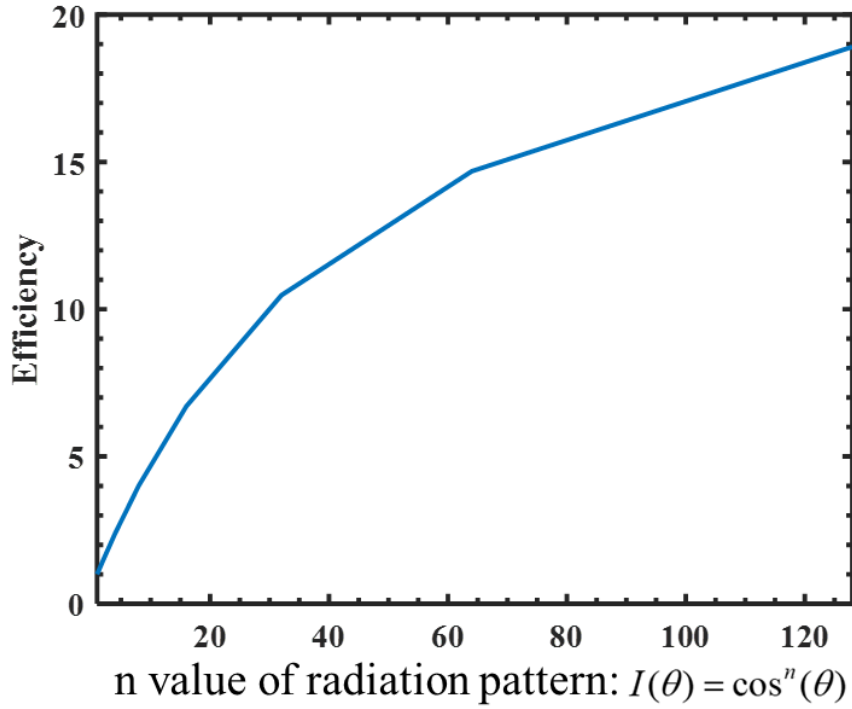
Figure 5-4 Normalized OSE of a display with various radiation pattern in a VR system.

The second and third metrics are related to color performance: one is field color gamut coverage, and the other is field color non-uniformity. As illustrated in Fig. 5-2(b), the angular power collection efficiency of different pixel positions will also affect the received emission spectrum, which can be further defined as:

$$Spectrum_y = \int_{\theta=0}^{\theta=90} S_\theta(\lambda) \times \Omega_\theta \times C_{(\theta,y)}, \tag{5-3}$$

where $S(\theta)$ is the angular emission spectrum of the display, and the definitions of other parameters have been given in Eq. (5-2). Based on Eq. (5-3), we can define the received emission spectrum of each emission pixel. Here, we use the pixel in the center of the display to define the field color

gamut coverage of the VR system. In addition, the field color non-uniformity is further defined by the color difference between adjacent pixels and the center pixel of the display.

5.3 LCD light engine

A transmissive LCD consists of a backlight unit and an LC panel. The backlight provides lots of freedom to modulate the radiation pattern of the display. The radiation pattern and color gamut of an LCD is mainly determined by the backlight unit, while the angular color shift and dark state light leakage are mainly caused by the LC panel. In our simulation, we use the parameters of a low viscosity LC material reported in [98] in the short-range lurch control in-plane switching (SLC-IPS) mode [99] in order to achieve a fast response time for VR display applications. As shown in Fig. 5-5(a), the electrode area is shown by green color, the dead zone gap marked by the red dashed lines with space W = 2.3 μm, and the subpixel pitch L = 8 μm for a high-resolution-density [>1000 PPI (pixel per inch)] display panel. The on-state voltage is set at 7V to drive in the fast response area. The obtained average gray-to-gray response time is 2.74 ms. The optical properties of such an LC panel compensated by the +A and -A plates as described in [100] are simulated by a commercial LCD simulator (Techwiz LCD 3D) and results are plotted in Fig. 5-5(a-d), including 2D transmittance distribution, VT curve, angular color shift, and isocontrast contours.

In an LCD, the emitted backlight is further modulated by the LC panel to control the brightness pixel by pixel. Therefore, its radiation pattern can be defined as:

$$I_{display} = I_{backlight} \times T_{LC}(\theta, \varphi, \lambda, g) \times T_{CF}, \qquad (5\text{-}4)$$

where $I_{display}$ and $I_{backlight}$ is the radiation pattern of the LCD and backlight unit, T_{LC} is the transmittance of LC panel with different incident angle (θ, and φ), wavelength (λ), and gray level

(g), and T_{CF} is the transmittance of color filters (CFs). For simplicity, we set $T_{CF} = 0.33$ for the employed white light source. In addition, in practical application, the thin film transistor (TFT), data line, and gate line also occupy part of pixel area and block the backlight. Therefore, the LC aperture ratio should be further considered when the layout of the LC panel has been defined.

Here, a backlight unit with a Lambertian radiation pattern is implemented in the LCD, and the corresponding display radiation pattern is obtained from Eq. (5-4). The angular light leakage and color shift of the displays cause uneven field brightness and field color in the VR system. However, as shown in Fig. 5-5(c), due to the wide viewing angle of IPS LCD, the angular color shift of the LC panel can be ignored within the 20° polar angle range, corresponding to the upper limit of the angular power collection efficiency function. Figure 5-5(e) shows that the worst field color unevenness of the three primary colors is about 0.0005, which is much smaller than the just noticeable color difference of 0.02. In addition, as shown in Fig. 5-5(d), the light leakage of the LC panel is better compensated in the horizontal view than in the vertical direction, so the contrast ratio is widely expanded in the horizontal direction. Considering the influence of the VR imaging lens, the light leakage rate of each emitting pixel is shown in Fig. 5-5(f). In a VR system, pixels located at the edge of the display in the x-direction will have more serious light leakage.
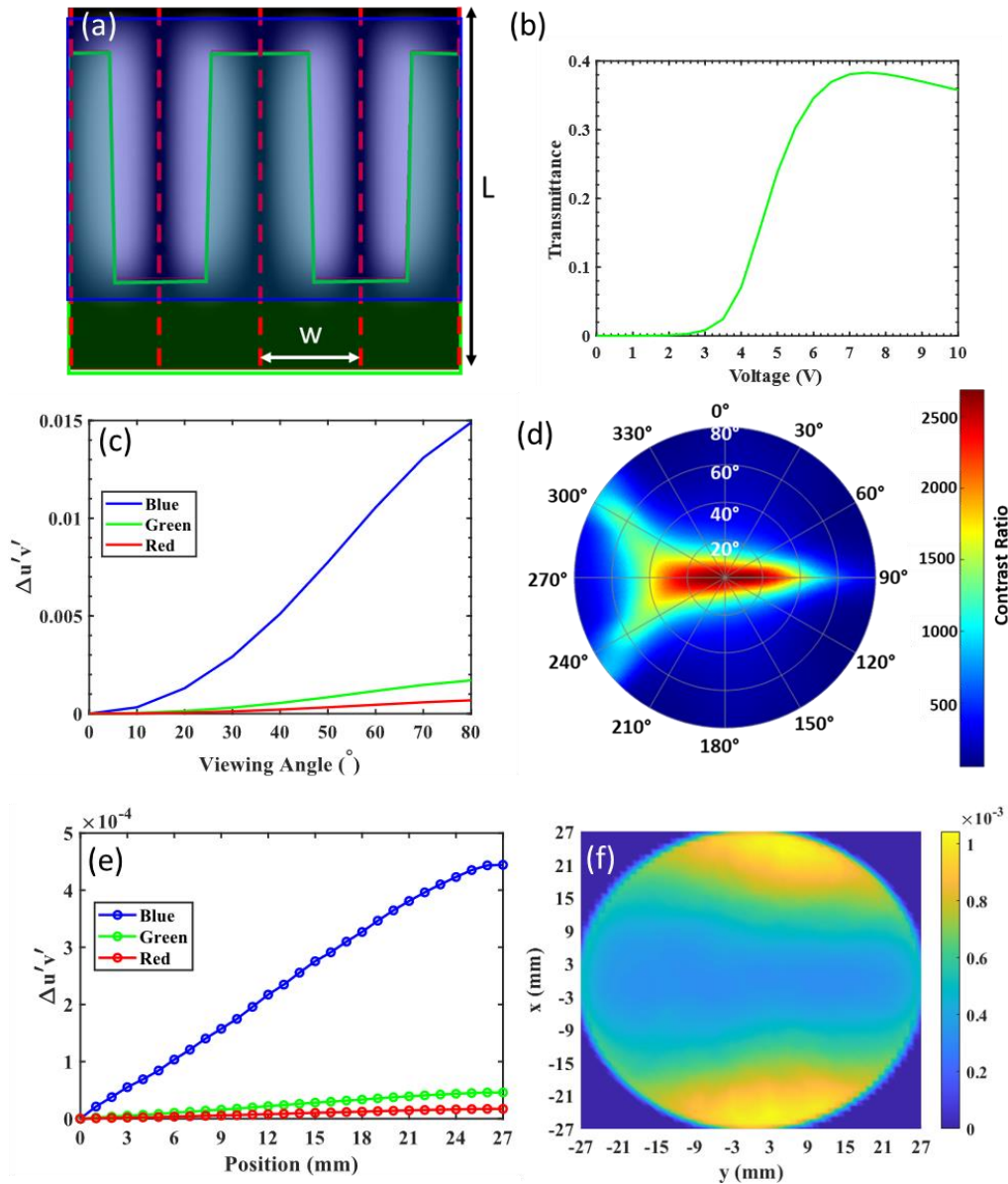
Figure 5-5 (a) The 2D transmittance distribution of SLC-IPS under on-state driving voltage; W = 2.3 μm, and L = 8 μm (b) Simulated voltage–transmittance curves of the SLC-IPS at λ= 550 nm; The 100% transmittance is normalized to the transmittance of two parallel polarizers and 100% aperture area of fast response region. The simulated (c) angular color shift and (d) isocontrast contour of the SLC-IPS with compensation films. Under Lambertian backlight source, (e) the field color non-uniformity and (f) the dark state light leakage ratio of the LCD based VR system.

In addition to the LC panel, by using patterned prisms with different base and apex angles, the radiation pattern of the backlight unit can be locally modulated. As shown in Fig. 5-6(a), the mLED backlit LCD consists of a backplane reflector (specular reflector: R=90%), a mLED array (Lambertian emission source), a diffuser (Lambertian diffuser), and two crossed brightness enhancement films (BEFs; apex angle=90°; base angle=45°; width=50 µm). Firstly, we set the refractive index of the BEF to vary from 1.4 to 1.7 and plot the corresponding angular intensity distribution after crossing the BEFs in Fig. 5-6(b). When the refractive index of BEF increases from 1.4, 1.5, 1.6, to 1.7, although the total output power of backlight unit drops from 100%, 87.5%, 72.5%, to 56.43%, the light intensity at normal direction increases from 58%,67%, 83%, to 100%. Considering the angular power collection function of the VR system, the larger intensity in normal view may achieve a higher field intensity in the center area of the display panel. To verify our inference, we calculate the radiation pattern of the on-state LCD by Eq. (5-4) and import the results to the optical simulation model in LightTools to get the TLE distribution of the VR system. Here, the TLE is the ratio of power received by the eye pupil to the power emitted from the LED devices. All the losses in backlight unit, LC panel, color filters, and VR system are considered. Figure 5-6(c-f) shows the results of LCD backlight unit with a BEF, whose refractive index ranges from 1.4 to 1.7. The TLE of pixels at the center of the display panel (x = 0, y = 0) is raised from 0.011%, 0.014%, 0.016%, to 0.018% as the refractive index of BEF increases from 1.4, 1.5, 1.6 to 1.7, respectively. However, the TLE uniformity between the center and margin pixels (the ratio of TLE_{margin} to TLE_{center}) also changes from 74%, 74%, 77%, to 43%. This uneven TLE may further cause the vignetting effect in the VR system.
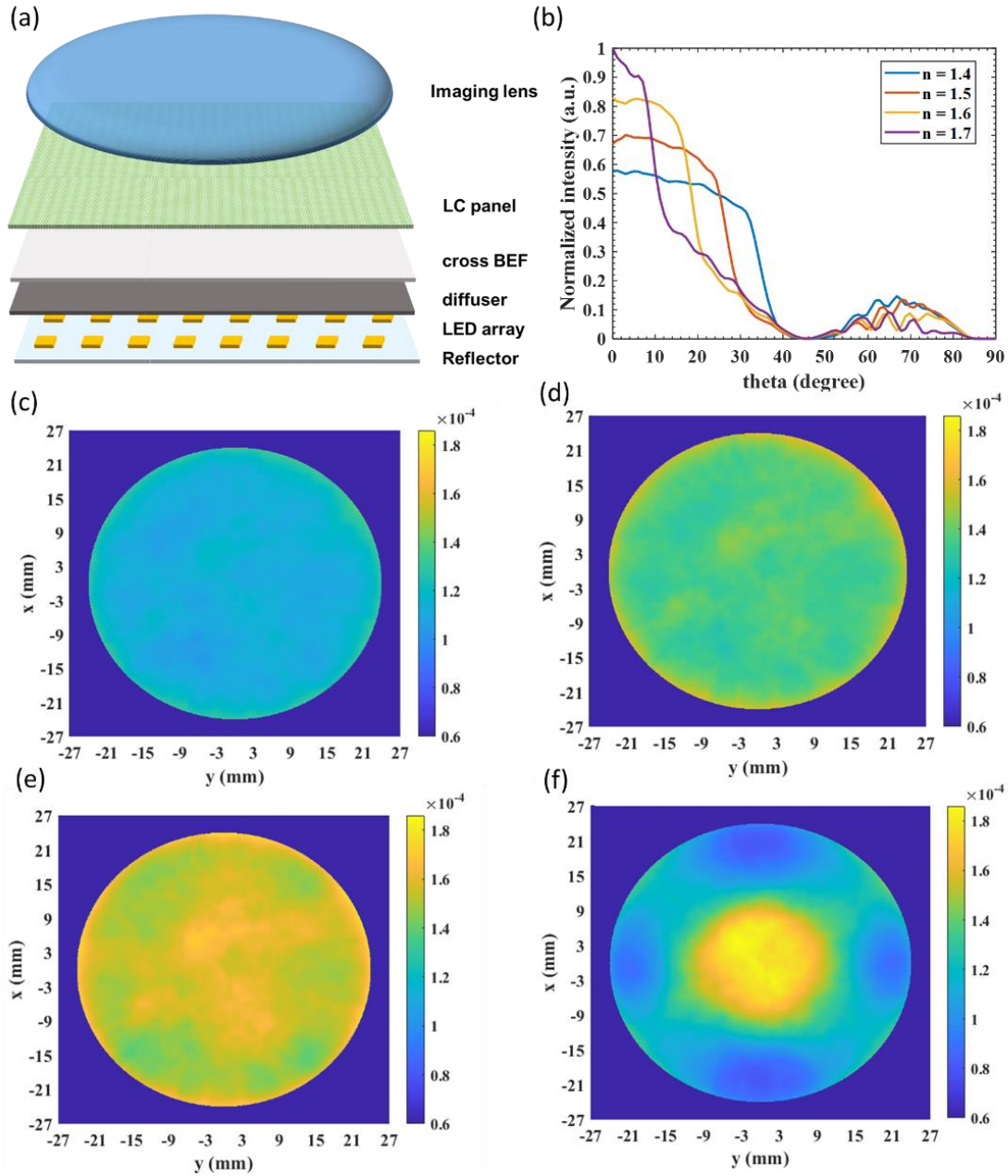
Figure 5-6 (a) Schematic of the LCD based VR system. (b) The angular intensity distribution of backlight unit with BEF (n = 1.4 to n = 1.7). The TLE distribution of each pixel in the LCD based VR system with BEF having various refractive index: (c) n = 1.4, (d) n = 1.5, (e) n = 1.6, and (f) n = 1.7.

To further improve the TLE and solve the vignetting issue of the VR system, the panel is evenly divided into 9 uniform zones, that means the zone width is 1/3 of the panel width. In each

zone, the unit cell which is an inverted prism ($n=1.4$) with an apex angle $\beta=30°$, a base angle $\alpha=60°$, and a width $w=50$ µm is implemented on the top of the crossed BEF to locally modulate the radiation pattern of the LCD backlight as shown in Fig. 5-7(a). The angle between the prism axis and the y axis is different in each zone, ranging from 0° to 315°, with an interval of 45° from zone 1 to zone 8. Regarding to the symmetric structure from zone 1 to zone 8, here we only illustrate the radiation pattern of zone 1 to zone 3 in Fig. 5-7(b) to Fig. 5-7(d). Finally, the field intensity distribution of the VR system based on the LCD backlight with 2D inverted prisms is shown in Fig. 5-7(f). Compared to the result in Fig. 5-6(f), the inserted 2D inverted prism further increases the TLE of the VR system from 0.012% to 0.017% and improves the TLE uniformity from 43% to 77%.
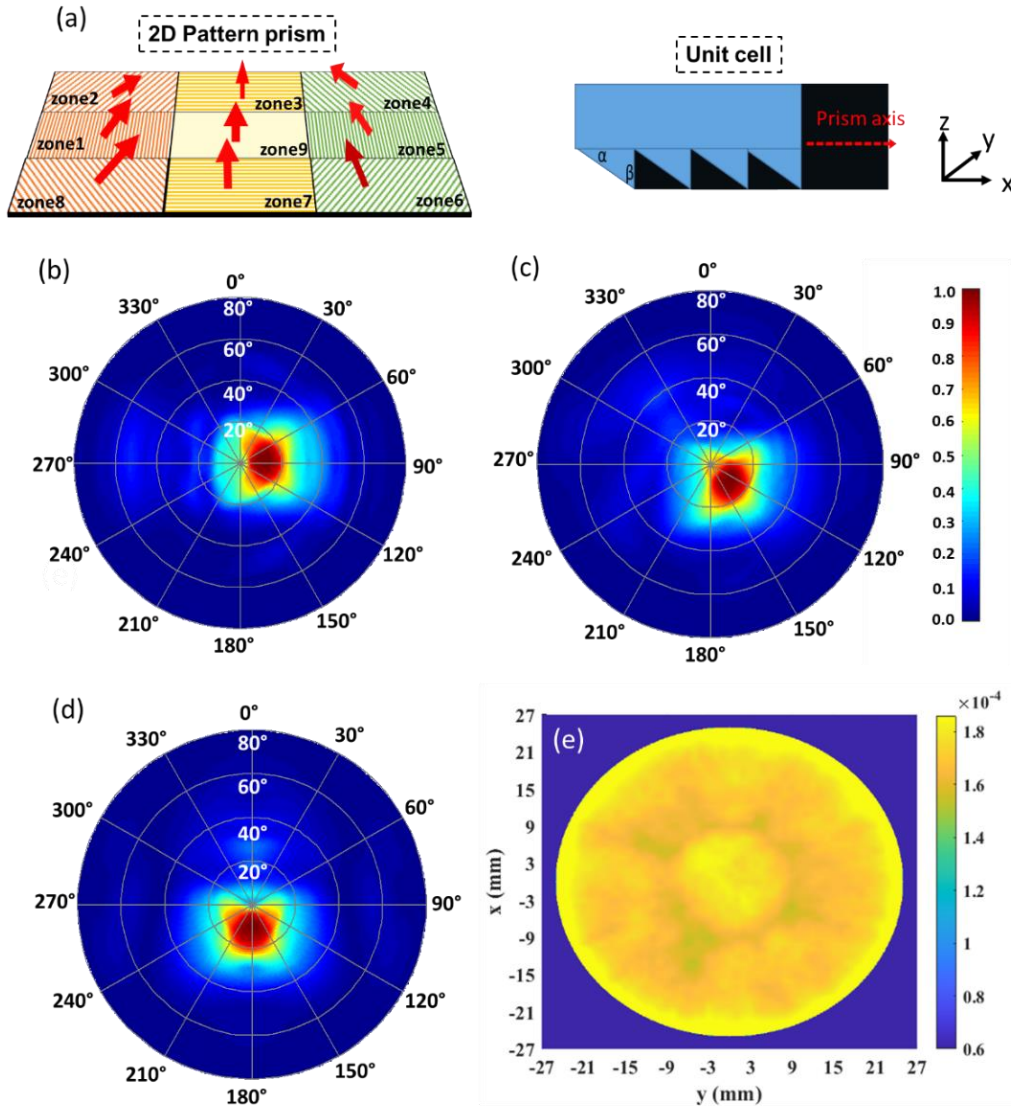
Figure 5-7 (a) Schematic of 2D patterned prism. The backlight radiation pattern in local (b) zone 1, (c) zone 2, and (d) zone 3. (e) The TLE distribution of each pixel in an LCD-based VR system with 2D patterned prism. BEF: n = 1.7.

5.4 OLED light engine

In this paragraph, we optimize the device structure of OLEDs for VR devices to achieve high OSE, indistinguishable field color nonuniformity, and vivid color performance. Due to the functional difference between direct view displays and projection displays, the optimized OLED

device structure should be different for each system. More specifically, compared to a direct-view OLED display, an additional eyepiece is used in the VR system to produce a magnified virtual image. As shown in Fig. 5-4, matching the display radiation pattern with the light acceptance angle of the eyepiece can significantly improve the optical system efficiency of the VR headset. Therefore, the display with directional radiation pattern is generally preferred. In OLED devices, a stronger cavity effect is usually used to achieve a more directional radiation pattern, but it also leads to a larger angular color shift, which is unacceptable in direct-view display applications [101,102]. However, it should not be a problem in VR applications, because the relatively small light receiving angle of the eyepiece significantly alleviates the color non-uniformity of the displayed virtual image. In a VR system, users observe the OLED panel through a magnifier lens. Meanwhile, different pixels have different light acceptance angles, which will cause a slight color non-uniformity in the generated virtual image. The color non-uniformity of virtual image can be calculated by Eq. (5-3). Here, a red top-emitting OLED shown in Fig. 5-8(a) is used as an example to illustrate the difference of microcavity structure between the optimized direct-view OLED display and the OLED for VR display. At the beginning, the cathode thickness is set at 10 nm (silver), while the HTL thickness varies from 5 nm to 300 nm, which is used to modulate the resonance wavelength of the OLED microcavity. In the optimization process, two critical points deserve special mention. First, when the HTL is 210 nm, the OLED device exhibits the highest EQE. The other is that when the HTL is 180 nm, the maximum intensity of the OLED device occurs at normal angle. The normalized radiation patterns of these two structures are plotted in Fig. 5-8(b). In addition, the emission spectrum as a function of viewing angle is also plotted in Fig.

5-8(c) and (d). It is commonly known that by detuning the resonance wavelength of the OLED device, maximum EQE can be obtained, but the tradeoff is increased angular color shift.
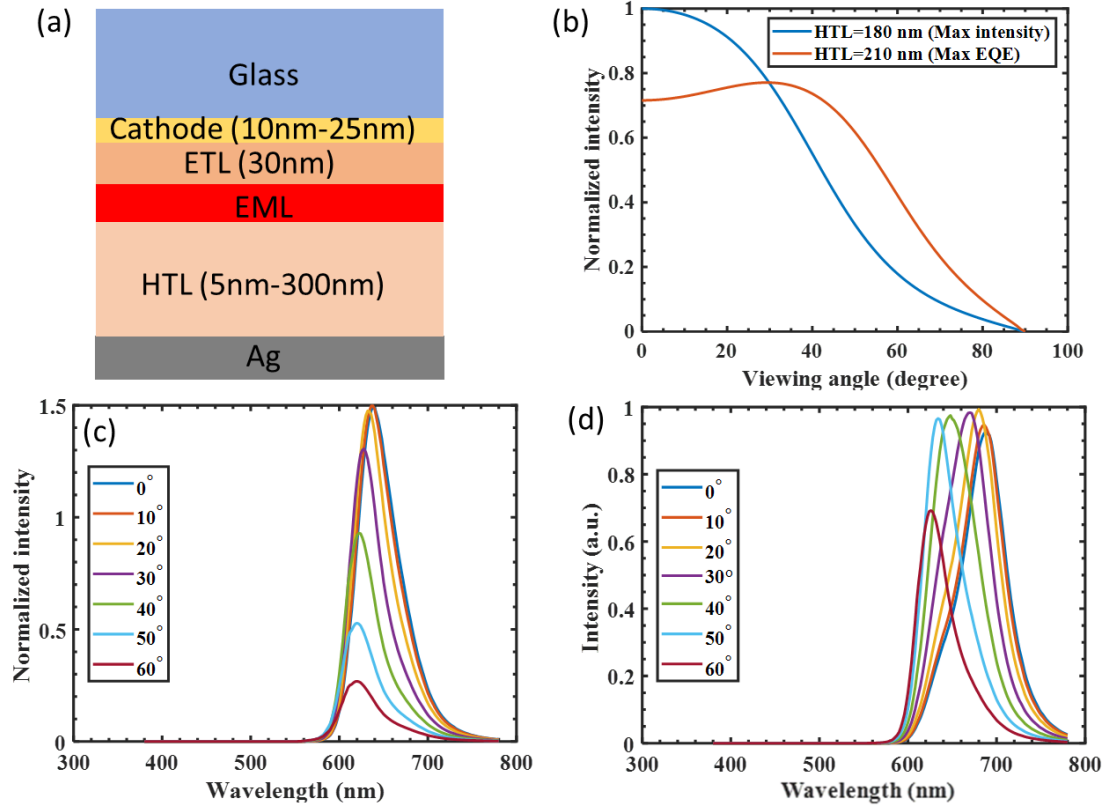
Figure 5-8 (a) Layer structure of a red OLED device. (b) Normalized radiation patterns of the two critical OLED devices. Simulated angular spectral shift of the OLED device with (c) maximum normal intensity and (d) maximum EQE.

Next, we further modify the microcavity strength by adjusting the silver film thickness [103]. As shown in Fig. 5-9, when the thickness of the top semi-transparent cathode increases from 10 nm to 25 nm, the reflectance of the corresponding semi-transparent cathode at λ=630 nm increases from 25%, 43%, 58%, to 69%, respectively. In addition, the angular color shift ($\Delta u'v'$) between 0° and 60° viewing angles also increases from 0.066, 0.0933, 0.1126, to 0.1289, as shown in Fig. 5-9(b) and (c). As mentioned above, because the light acceptance angle is relatively small, such an

angular color shift is not a problem in the VR system. The corresponding image color non-uniformity is calculated using Eq. (5-3) and results are depicted in Fig. 5-9(d). In other words, in a VR system, there is no strict limit on the angular color shift of the OLED device, and we can more freely optimize the OLED microcavity to achieve a higher optical efficiency and narrower full-width at half-maximum (FWHM). The emission spectrum and system efficiency of the OLED display (as a function of Ag thickness) in the VR system are summarized in Fig. 5-9(e) and (f), respectively. Obviously, the stronger cavity effect narrows the FWHM of the emission spectrum. On the other hand, in Fig. 5-9(f), the blue and orange lines illustrate the EQE of the OLED devices and the system efficiency of OLED displays in VR applications as a function of Ag thickness, respectively. This shows that if we take the EQE of the OLED device as the sole optimization objective without considering the collection efficiency of the VR system, we could choose the OLED device with a 15-nm-thick Ag layer. However, in a VR headset, the OLED device with 25-nm-thick Ag can increase the system efficiency by about 10%, in comparison with that of 15-nm-thick Ag. This difference is due to the more directional radiation pattern of the microcavity OLED device with a stronger cavity effect, which leads to a higher collection efficiency of the VR system. If we further consider the human eye's responsivity to light, the efficiency difference could exceed 30%, as shown by the yellow line in Fig. 5-9(f). This can be explained by the emission spectrum plotted in Fig. 5-9(e). A stronger microcavity concentrates the emitted power at a wavelength below 650 nm, which in turn contributes to a higher luminous efficiency.
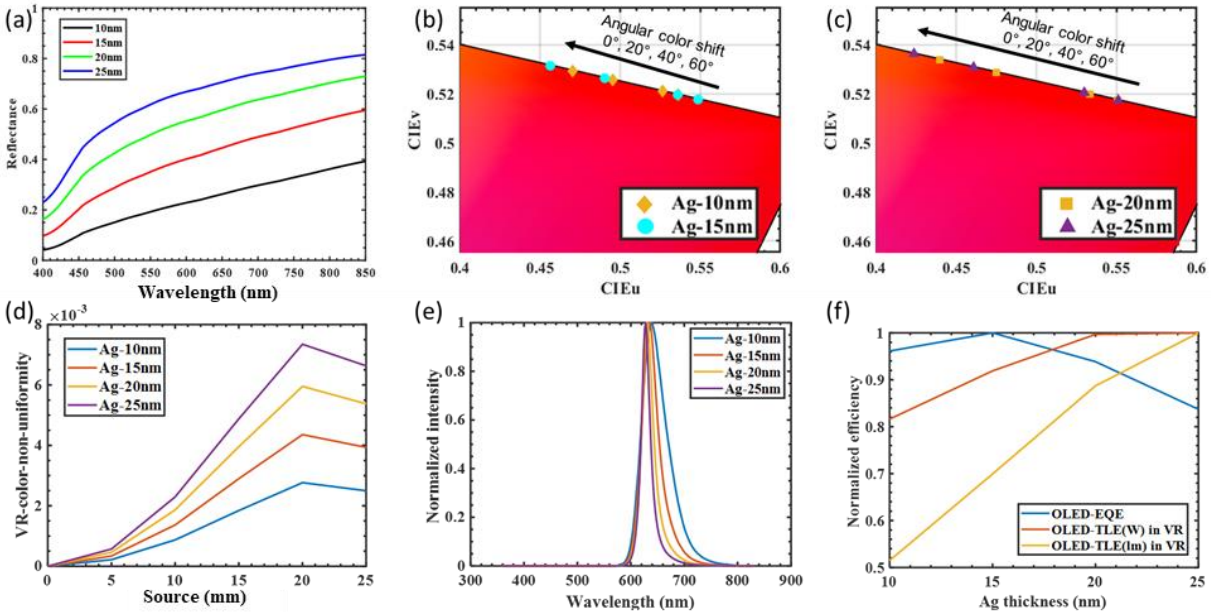
Figure 5-9 (a) Simulated reflectance of the semi-transparent cathode at 4 specified thicknesses. Angular color shift of OLED devices with (b) 10-nm and 15-nm, and (c) 20-nm and 25-nm Ag semi-transparent cathodes. (d) VR color non-uniformity of OLED devices with 4 specified cavity strengths. (e) Simulated emission spectra of OLED devices with different cavity strengths, and (f) Simulated EQE and TLE of OLED devices with different cavity strengths.

5.5 Summery

In this chapter, novel device structures for LCDs and OLED displays are proposed and optimized based on three proposed VR system metrics: total light efficiency, field brightness non-uniformity, and field color non-uniformity. These metrics are used to evaluate the efficiency and image quality of VR devices. The proposed light engines seek to increase the total light efficiency while maintaining good image quality without serious vignetting effects. For LCD-based VR systems, a 2D patterned prism film is applied on top of a directional backlight unit to increase the total light efficiency by 41% and reduce the brightness non-uniformity by 34%. For OLED-based VR systems, a stronger microcavity is applied to increase the directionality of emitted light,

resulting in 30% higher total light efficiency compared to the reference device used in direct-view displays. Although the optimized OLED displays stronger angular color shift, it does not seriously affect the color uniformity of virtual images due to the small acceptance cone of the VR device. This optimization method is proven to be effective in designing next-generation display devices for VR systems.

CHAPTER 6: CONCLUSION

In this dissertation, we aim to solving two major challenges faced by current VR display systems, namely degraded image quality and relatively low optical efficiency. To address these issues, we propose novel design rules and device structures for the light engine, which not only enhance the performance of the light engine itself but also facilitate an effective integration with VR imaging optics, thereby improving the image quality and efficiency of a VR display system.

For the HDR light engines, mLED backlit LCD is a strong candidate, but it suffers from halo artifacts that significantly degrade the image quality. To mitigate this issue, we firstly developed an optical simulation model to analyze the impact of HVS, image content, and viewing conditions on the severity of halo artifacts in mLED backlit LCDs. The results show that light scattering in the eye (also known as eye halo) smears out the halo artifact and reduces its visibility in HVS. Additionally, an objective metric, D-value, is proposed to evaluate the correlation between image content and the noticeability of halo artifacts. Based on our test images, a good correlation is further verified. Then, we evaluate the noticeability of halo artifacts under different viewing conditions, including various ambient lighting and viewing angles and found that the reflected ambient light also smears out the halo artifacts of mLED backlit LCD. As a result, increasing ambient illuminance from 0 (dark room) to 500 lux reduces the dimming zones required to suppress the halo artifacts by approximately 10 times. Our established guidelines are useful to optimize the mLED backlit HDR LCDs and to avoid image degradation due to halo artifacts.

In VR devices, it is important to evaluate the overall image quality of the entire display system, rather than just the light engine. In Chapter 3, we describe an optical simulation model to evaluate the image quality of VR devices, with the image contrast of fringe patterns at different frequencies

serving as an evaluation metric. Our results reveal that the stray light and aberrations of imaging optics are key factors that affect the image contrast for high (>5 cpd) and mid-frequency (>0.1 cpd and <5 cpd) image contents, respectively. In our pancake lens design, the aberration of imaging optics limits the maximum resolvable density of light engines to 1270 ppi, and the existence of stray light, although undesirable, sets the upper limit for the device contrast ratio. More importantly, our study shows that the contrast ratio of the light engine mainly affects the low-frequency image contents (<0.1cpd). Therefore, when applying local dimming technology to LCD light engines, the size of the local dimming zone does not need to be very small. It just needs to be properly sized (around 2-mm to 4-mm wide, depending on the intrinsic LCD's contrast ratio) to improve the image contrast of low-frequency patterns. Overall, our system analysis indicates that light engines should be designed based on the VR imaging optics, rather than relying solely on the HVS characteristics.

In AR devices, a self-emissive, compact-size μ-LED panel with high peak brightness is an outstanding light engine candidate. To achieve high resolution density, a color-converted μ-LED display with a pixelated quantum dot (QD) array has gained significant attention. In Chapter 4, we present a novel device structure to enhance the efficiency and color performance of color-converted μ-LED light engine. The high efficiency μ-LED light engine is achieved through two steps: first, tailoring the radiation pattern of the μ-LED to concentrate the emitted blue light to targeted subpixels; second, laminating a pixelized CLC film to recycle the leaked blue light back to the color conversion film. With these improvements, we double the CCE of the display system and expand the color gamut coverage to 90% Rec. 2020. After that, a proof-of-concept experiment

was conducted to verify the function of pixelized CLC film. It is worth noting that the developed device structure has potential applications to advance all types of color-converted display systems.

In chapter 5, we reduce the power loss during imaging projection by tailoring the radiation pattern of light engines to match the etendue of the VR display system. Moreover, we also consider the potential side effects such as vignetting effect and non-uniformity on the projected image. We proposed novel device structures for LCDs and OLED display light engines to enhance the VR system efficiency without compromising the image quality. For an OLED based VR system, the optimized OLED device exhibits a 30% higher total light efficiency. More importantly, due to the small acceptance cone of VR devices, the color uniformity of virtual images is less affected by the angular color shift of the light engine. As a result, the stronger angular color shift exhibited by our optimized OLED does not significantly impact the color uniformity of projected images. For LCD-based VR systems, a 2D patterned prism film is applied on top of a directional backlight unit to locally modulate the radiation pattern of light engine. By locally matching the emission cone of the light engine with the acceptance cone of the imaging optics, the proposed light engine can increase the total light efficiency by 41% and reduce the brightness non-uniformity by 34%. Our optimization method is proven to be effective for designing next generation display light engines for VR applications.

APPENDIX: STUDENT PUBLICATIONS

Journal publications

1. E. L. Hsiang, Z. Yang, Q. Yang, P. C. Lai, C. L. Lin, and S. T. Wu, "AR/VR light engines: perspectives and challenges," Adv. Opt. Photon. **14**, 783-861 (2022).

2. K. Yin, E.L. Hsiang, J. Zou, Y. Li, Z. Yang, Q. Yang, P.C. Lai, C.L. Lin, and S. T. Wu, "Advanced liquid crystal devices for augmented reality and virtual reality displays: Principles and Applications," Light Sci. Appl. **11**, 161 (2022).

3. Z. Yang, E.L. Hsiang, Y. Qian, and S. T. Wu, "Performance comparison between mini-LED backlit LCD and OLED display for 15.6-inch notebook computers," Appl. Sci. **12**, 1239 (2022).

4. M. A. Triana, E. L. Hsiang, C. C. Zhang, Y. Dong, and S. T. Wu, "Luminescent Nanomaterials for Energy Efficient Display and Healthcare," ACS Energy Lett. **7**, 1001-1020 (2022).

5. E. L. Hsiang, Z. Yang, T. Zhan, J. Zou, H. Akimoto, S. T. Wu, "Optimizing the display performance for virtual reality systems," OSA Continuum **4**, 3052-3067 (2021).

6. E. L. Hsiang, Z. He, Z. Yang, Y. F. Lan, S. T. Wu, "Tailoring the light distribution of micro-LED displays with a compact compound parabolic concentrator and an engineered diffusor," Opt. Express **29**, 39859-39873 (2021).

7. J. Xiong, E.L. Hsiang, Z. He, T. Zhan, and S. T. Wu, "Augmented reality and virtual reality displays: emerging technologies and future perspectives," Light Sci. & Appl. **10**, 216 (2021).

8. J. Zou, T. Zhan, E. L. Hsiang, X. Du, X. Yu, K. Li, and S. T. Wu, "Doubling the optical efficiency of VR systems with a directional backlight and a diffractive deflection film," Opt. Express **29**, 20673-20686 (2021).

9. E. L. Hsiang, Z. Yang, Q. Yang, Y. F. Lan, and S. T. Wu, "Prospects and challenges of mini-LED, OLED, and micro-LED displays," J. Soc. Inf. Display **29**, 446-465 (2021).

10. M. Y. Deng, E. L. Hsiang, Q. Yang, B. S. Chen, F.Y. Lin, C. E. Wu, M. H. Lee, S. T. Wu, and C. L. Lin, "Reducing Power Consumption of Active-Matrix Mini-LED Backlit LCDs by Driving Circuit," IEEE Trans. Electron Devices **68**, 2347-2354 (2021).

11. E. L. Hsiang, Y. Li, Z. He, T. Zhan, C. Zhang, Y. F. Lan, Y. Dong, and S. T. Wu, "Doubling the optical efficiency of color-converted micro-light-emitting-diode displays with a patterned cholesteric liquid crystal polymer film," J. Soc. Inf. Display **29**, 288-297 (2021).

12. T. Zhan, E.L. Hsiang, K. Li, and S. T. Wu, "Enhancing the Optical Efficiency of Near-Eye Displays with Liquid Crystal Optics," Crystals **11**, 107 (2021).

13. J. Zou, Q. Yang, E.L. Hsiang, H. Ooishi, Z. Yang, K. Yoshidaya, and S. T. Wu, "Fast-Response Liquid Crystal for Spatial Light Modulator and LiDAR Applications," Crystals **11**, 93 (2021).

14. E. L. Hsiang, Y. Li, Z. He, T. Zhan, C. Zhang, Y. Dong, and S. T. Wu, "Enhancing the efficiency of color conversion micro-LED display with a patterned cholesteric liquid crystal polymer film," Nanomaterials **10**, 2430 (2020).

15. E. L. Hsiang, Q. Yang, Z. He, J. Zou, and S. T. Wu, "Halo effect in high-dynamic-range mini-LED backlit LCDs," Opt. Express **28**, 36822-36837 (2020).

16. Z. He, K. Yin, E. L. Hsiang, and S. T. Wu, "Birefringent light-shaping films for mini-LED backlights," J. Soc. Inf. Disp. **28**, 476-482 (2020).

17. J. Zou, E. L. Hsiang, T. Zhan, K. Yin, Z. He, and S. T. Wu, "High Dynamic Range Head-up Display," Opt. Express **28**, 24298-24307 (2020).

18. Y. Huang, E. L. Hsiang, M.Y. Deng, and S.T. Wu, "Mini-LED, Micro-LED and OLED displays: Present status and future perspectives," Light: Sci. & Appl. **9**, 105 (2020).

19. E. L. Hsiang, Z. He, Y. Huang, F. Gou, Y. F. Lan, and S.T. Wu, "Improving the power efficiency of micro-LED displays with optimized LED chip sizes," Crystals **10**, 494 (2020).

20. Z. He, K. Yin, E. L. Hsiang, and S.T. Wu, "Volumetric light-shaping polymer-dispersed liquid crystal films for mini-LED backlights," Liq. Cryst. **47**, 1458-1463 (2020).

21. F. Gou, E. L. Hsiang, G. Tan, P. T. Chou, Y. L. Li, Y. F. Lan, and S.T. Wu, "Angular color shift of micro-LED displays," Opt. Express **27**, A746-A757 (2019).

22. F. Gou, E. L. Hsiang, G. Tan, Y. F. Lan, C. Y. Tsai, and S. T. Wu, "Tripling the optical efficiency of color-converted micro-LED displays with funnel-tube array," Crystals **9**, 39 (2019).

23. F. Gou, E. L. Hsiang, G. Tan, Y. F. Lan, C. Y. Tsai, and S. T. Wu, "High performance color-converted micro-LED displays," J. Soc. Inf. Disp. **27**, 199-206 (2019).

Conference proceedings

1. <u>E. L. Hsiang</u>, Z. He, Z. Yang, Y. F. Lan, and S. T. Wu, "High Efficiency μLED Light Engine for AR/VR Displays" SID Symp. Digest **53**, 1316-1319 (2022)

2. Z. Yang, <u>E. L. Hsiang</u>, Y. Qian, and S. T. Wu, "Systematic Comparisons on Display Performances including Halo Effect" SID Symp. Digest **53**, 436-439 (2022)

3. J. Zou, T. Zhan, <u>E. L. Hsiang</u>, J. Xiong, K. Li, and S. T. Wu, "Pancharatnam-Berry phase optical elements for VR displays" Proc. SPIE, Advances in Display Technologies XII, **12024**, 1202409 (2022).

4. <u>E. L. Hsiang</u>, Z. Yang, T. Zhan, J. Zou, H. Akimoto, and S. T. Wu, "Analysis and optimization on display performance for virtual reality" Proc. SPIE, Advances in Display Technologies XII, **12024**, 1202405 (2022).

5. <u>E. L. Hsiang</u>, Y. Li, Z. He, T. Zhan, C. Zhang, Y. F. Lan, Y. Dong, S. T. Wu, "Doubling the Optical Efficiency of Color-Converted MicroLED Displays with a Patterned Cholesteric Liquid-Crystal Polymer Film," SID Symp. Digest **52**, 895-898 (2021)

6. <u>E. L. Hsiang</u>, Q. Yang, Z. He, J. Zou, S. T. Wu, "Ambient Light and Human Vision Effects on High-Dynamic-Range Displays," SID Symp. Digest **52**, 646-649 (2021)

7. T. Zhan, <u>E. L. Hsiang</u>, J. Zou, J. Xiong, K. Li, S. T. Wu, "Light-Efficient Virtual Reality Displays," SID Symp. Digest **52**, 1246-1249 (2021)

8. J. Zou, <u>E. L. Hsiang</u>, T. Zhan, K. Yin, Z. He, S. T. Wu, "High-Dynamic-Range HUD with a Polarization Selective Optical Combiner," SID Symp. Digest **52**, 564-567 (2021)

9. E. L. Hsiang, Z. He, Y. Huang, F. Gou, Y.F. Lan, and S.T. Wu, "Optimal chip size for reducing the power consumption of micro-LED displays," Advances in Display Technologies XI **11708**, 117080M (2021).

10. E. L. Hsiang, M. Y. Deng, Y. Huang, F. Gou, Z. He, C. L. Lin, S. T. Wu, "Power consumption of OLED and μLED displays," SID Symp. Digest **51**, 528-531 (2020)

11. E. L. Hsiang, Y. Huang, Q. Yang, S. T. Wu, "High Dynamic Range Mini-LED and Dual-Cell LCDs," SID Symp. Digest **51**, 115-118 (2020)

12. F. Gou, E.L. Hsiang, G. Tan, P.T. Chou, Y.L. Li, Y.F. Lan, and S.T. Wu, High-efficiency micro-LED displays with indistinguishable color shift, Proc. SPIE, Advances in Display Technologies X **11304**, 113040I (2020)

13. Z. He, K. Yin, E. L. Hsiang, M. C. Li, S. L. Lee, K. C. Tien, S. T. Wu, "Birefringent Light-Shaping Film for Mini-LED Backlights," SID Symp. Digest **51**, 239-242 (2020)

14. F. Gou, E. L. Hsiang, G. Tan, Y. F. Lan, C. Y. Tsai, S. T. Wu "High Efficiency Color-Converted Micro-LED Displays," SID Symp. Digest **50**, 22-25 (2019)

REFERENCES

1. J. H. Lee, I. C. Cheng, H. Hua, and S. T. Wu, *Introduction to Flat Panel Displays* 2nd Ed. (John Wiley & Sons, 2020).

2. E. L. Hsiang, Z. Yang, Q. Yang, Y. F. Lan, and S. T. Wu, "Prospects and challenges of mini-LED, OLED, and micro-LED displays," J. Soc. Info Disp. **29**, 446–465 (2021).

3. H. W. Chen, J. H. Lee, B. Y. Lin, S. Chen, and S. T. Wu, "Liquid crystal display and organic light-emitting diode display: present status and future perspectives," Light Sci. Appl. **7**, 17168–17168 (2018).

4. R. Azuma, Y. Baillot, R. Behringer, S. Feiner, S. Julier, and B. MacIntyre, "Recent advances in augmented reality," IEEE Comput. Graph. Appl. **21**, 34–47 (2001).

5. S. K. Feiner, "Augmented Reality: A New Way of Seeing," Sci. Amer. **286**, 48–55 (2002).

6. J. Xiong, E. L. Hsiang, Z. He, T. Zhan, and S. T. Wu, "Augmented reality and virtual reality displays: emerging technologies and future perspectives," Light Sci Appl **10**, 216 (2021).

7. P. Milgram and F. Kishino, "A taxonomy of mixed reality visual displays," IEICE Trans. Information Systems **E77-D**, 1321–1329 (1994).

8. H. Hua, "Enabling Focus Cues in Head-Mounted Displays," Proceedings of the IEEE **105**, 805–824 (2017).

9. B. C. Kress, *Optical Architectures for Augmented-, Virtual-, and Mixed-Reality Headsets* (SPIE Press, 2020).

10. E. L. Hsiang, Z. Yang, Q. Yang, P. C. Lai, C. L. Lin, and S. T. Wu, "AR/VR light engines: perspectives and challenges," Adv. Opt. Photon. **14**, 783–861 (2022).

11. D. K. Yang and S. T. Wu, Fundamentals of Liquid Crystal Devices 2nd Ed. (John Wiley & Sons, 2014).

12. M. N. Ernstoff, A. M. Leupp, M. J. Little, and H. T. Peterson, "Liquid crystal pictorial display," International Electron Devices Meeting 548–551 (1973).

13. C. W. Tang and S. A. VanSlyke, "Organic electroluminescent diodes," Appl. Phys. Lett. **51**, 913–915 (1987).

14. Y. Shirasaki, G. J. Supran, M. G. Bawendi, and V. Bulović, "Emergence of colloidal quantum-dot light-emitting technologies," Nature Photon. **7**, 13–23 (2013).

15. H. X. Jiang, S. X. Jin, J. Li, J. Shakya, and J. Y. Lin, "III-nitride blue microdisplays," Appl. Phys. Lett. **78**, 1303–1305 (2001).

16. J. Ma, "Advanced MEMS-based technologies and displays," Displays **37**, 2–10 (2015).

17. S. Lee, M. Wang, G. Li, L. Lu, Y. Sulai, C. Jang, and B. Silverstein, "Foveated near-eye display for mixed reality using liquid crystal photonics," Sci. Rep. **10**, 16127 (2020).

18. J. Xiong, K. Yin, K. Li, and S. T. Wu, "Holographic Optical Elements for Augmented Reality: Principles, Present Status, and Future Perspectives," Adv. Photonics Res. **2**, 2000049 (2021).

19. D. Cheng, Q. Wang, Y. Liu, H. Chen, D. Ni, X. Wang, C. Yao, Q. Hou, W. Hou, and G. Luo, "Design and manufacture AR head-mounted displays: A review and outlook," Light: Adv. Manuf. **2**, 350–369 (2021).

20. M. D. Fairchild, "Seeing, adapting to, and reproducing the appearance of nature," Appl. Opt. **54**, B107–B116 (2015).

21. H. Seetzen, W. Heidrich, W. Stuerzlinger, G. Ward, L. Whitehead, M. Trentacoste, A. Ghosh, and A. Vorozcovs, "High dynamic range display systems," ACM Trans. Graph. **23**, 760–768 (2004).

22. P. Lincoln, A. Blate, M. Singh, A. State, M. C. Whitton, T. Whitted, and H. Fuchs, "Scene-adaptive high dynamic range display for low latency augmented reality," in *Proc. 21st ACM SIGGRAPH Symposium on Interactive 3D Graphics and Games.* (ACM,San Francisco, CA, 2017).

23. H. Chen, G. Tan, M. C. Li, S. L. Lee, and S. T. Wu, "Depolarization effect in liquid crystal displays," Opt. Express **25**, 11315–11328 (2017).

24. M. Yoneya, Y. Utsumi, and Y. Umeda, "Depolarized light scattering from liquid crystals as a factor for black level light leakage in liquid-crystal displays," J. Appl. Phys. **98**, 016106 (2005).

25. E. L. Hsiang, Q. Yang, Z. He, J. Zou, and S. T. Wu, "Halo effect in high-dynamic-range mini-LED backlit LCDs," Opt. Express **28**, 36822–36837 (2020).

26. G. Tan, Y. Huang, M. C. Li, S. L. Lee, and S. T. Wu, "High dynamic range liquid crystal displays with a mini-LED backlight," Opt. Express **26**, 16572–16584 (2018).

27. G. Tan, Y. H. Lee, T. Zhan, J. Yang, S. Liu, D. Zhao, and S. T. Wu, "Foveated imaging for near-eye displays," Opt. Express **26**, 25076–25085 (2018).

28. J. Y. Wu, P. Y. Chou, K. E. Peng, Y. P. Huang, H. H. Lo, C. C. Chang, and F. M. Chuang, "Resolution enhanced light field near eye display using e-shifting method with birefringent plate," J. Soc. Info Disp. **26**, 269–279 (2018).

29. S. A. Cholewiak, Z. Başgöze, O. Cakmakci, D. M. Hoffman, and E. A. Cooper, "A perceptual eyebox for near-eye displays," Opt. Express **28**, 38008–38028 (2020).

30. E. L. Hsiang, Z. Yang, T. Zhan, J. Zou, H. Akimoto, and S. T. Wu, "Optimizing the display performance for virtual reality systems," OSA Contin. **4**, 3052–3067 (2021).

31. D. Cheng, Q. Hou, Y. Li, T. Zhang, D. Li, Y. Huang, Y. Liu, Q. Wang, W. Hou, and T. Yang, "Optical design and pupil swim analysis of a compact, large EPD and immersive VR head mounted display," Opt. Express **30**, 6584–6602 (2022).

32. Y. Geng, J. Gollier, B. Wheelwright, F. Peng, Y. Sulai, B. Lewis, N. Chan, W. S. T. Lam, A. Fix, D. Lanman, Y. Fu, A. Sohn, B. Bryars, N. Cardenas, Y. Yoon, and S. McEldowney, "Viewing optics for immersive near-eye displays: pupil swim/size and weight/stray light," Proc. SPIE **10676**, 1067606 (2018).

33. B. A. Narasimhan, "Ultra-Compact pancake optics based on ThinEyes super-resolution technology for virtual reality headsets," Proc. SPIE **10676**, 106761G (2018).

34. K. Yoshida, S. Ueda, A. Hachiya, K. Okada, A. Hirai, Y. Kawahira, K. Misaki, H. Furukawa, and H. Katoh SID Senior Member, "Thin and low-reflection metal black matrix for high ppi liquid crystal display," J. Soc. Info Disp. **30**, 413–422 (2022).

35. J. M. Smith, R. Ley, M. S. Wong, Y. H. Baek, J. H. Kang, C. H. Kim, M. J. Gordon, S. Nakamura, J. S. Speck, and S. P. DenBaars, "Comparison of size-dependent characteristics of blue and green InGaN microLEDs down to 1 μm in diameter," Appl. Phys. Lett. **116**, 071102 (2020).

36. P. Li, H. Li, M. S. Wong, P. Chan, Y. Yang, H. Zhang, M. Iza, J. S. Speck, S. Nakamura, and S. P. Denbaars, "Progress of InGaN-Based Red Micro-Light Emitting Diodes," Crystals **12**, 541 (2022).

37. K. Masaoka and Y. Nishida, "Metric of color-space coverage for wide-gamut displays," Opt. Express **23**, 7802–7808 (2015).

38. S. Daly, T. Kunkel, X. Sun, S. Farrell, and P. Crum, "41.1: Distinguished Paper: Viewer Preferences for Shadow, Diffuse, Specular, and Emissive Luminance Limits of High Dynamic Range Displays," Dig. Tech. Pap.- Soc. Inf. Disp. Int. Symp. **44**, 563–566 (2013).

39. J. L. Helman, "I3.4: Invited Paper: Delivering High Dynamic Range Video to Consumer Devices," Dig. Tech. Pap.- Soc. Inf. Disp. Int. Symp. **46**, 292–295 (2015).

40. S. H. Lee, S. L. Lee, and H. Y. Kim, "Electro-optic characteristics and switching principle of a nematic liquid crystal cell controlled by fringe-field switching," Appl. Phys. Lett. **73**, 2881–2883 (1998).

41. S. Scholz, D. Kondakov, B. Lüssem, and K. Leo, "Degradation Mechanisms and Reactions in Organic Light-Emitting Devices," Chem. Rev. **115**, 8449–8503 (2015).

42. J. H. Lee, C. H. Chen, P. H. Lee, H. Y. Lin, M. kit Leung, T. L. Chiu, and C. F. Lin, "Blue organic light-emitting diodes: current status, challenges, and future outlook," J. Mater. Chem. C .**7**, 5874–5888 (2019).

43. M. K. Fung, Y. Q. Li, and L. S. Liao, "Tandem Organic Light-Emitting Diodes," Adv. Mater. **28**, 10381–10408 (2016).

44. B. Zheng, Z. Deng, J. Zheng, L. Wu, W. Yang, Z. Lin, H. Wang, P. Shen, and J. Li, "41-2: Invited Paper: An Advanced High-Dynamic-Range LCD for Smartphones," Dig. Tech. Pap.-Soc. Inf. Disp. Int. Symp. **50**, 566–568 (2019).

45. T. Shirai, S. Shimizukawa, T. Shiga, S. Mikoshiba, and K. Käläntär, "44.4: RGB-LED Backlights for LCD-TVs with 0D, 1D, and 2D Adaptive Dimming," Dig. Tech. Pap.- Soc. Inf. Disp. Int. Symp. **37**, 1520–1523 (2006).

46. H. Chen, T. H. Ha, J. H. Sung, H. R. Kim, and B. H. Han, "Evaluation of LCD local-dimming-backlight system," J. Soc. Info Disp. **18**, 57–65 (2010).

47. J. J. McCann and V. Vonikakis, "Calculating Retinal Contrast from Scene Content: A Program," Front. Psychol. **8**, (2018).

48. Y. Huang, G. Tan, F. Gou, M. C. Li, S. L. Lee, and S. T. Wu, "Prospects and challenges of mini-LED and micro-LED displays," J. Soc. Info Disp. **27**, 387–401 (2019).

49. P. G. J. Barten, *Contrast Sensitivity of the Human Eye and Its Effects on Image Quality* (SPIE Press, 1999).

50. H. Strasburger, I. Rentschler, and M. Jüttner, "Peripheral vision and pattern recognition: A review," Journal of Vision **11**, 13 (2011).

51. L. E. E. Yun-Han, Z. Tao, and W. U. Shin-Tson, "Prospects and challenges in augmented reality displays," Virtual Reality & Intelligence Hardware **1**, 10–20 (2019).

52. C. Vieri, G. Lee, N. Balram, S. H. Jung, J. Y. Yang, S. Y. Yoon, and I. B. Kang, "An 18 megapixel 4.3″ 1443 ppi 120 Hz OLED display for wide field of view high acuity head mounted displays," J. Soc. Info Disp. **26**, 314–324 (2018).

53. L. Penninck, M. Diethelm, S. Altazin, R. Hiestand, C. Kirsch, and B. Ruhstaller, "Modelling crosstalk through common semiconductor layers in AMOLED displays," J. Soc. Info Disp. **26**, 546–554 (2018).

54. Y. E. Wu, M. H. Lee, Y. C. Lin, C. Kuo, Y. H. Lin, and W. M. Huang, "41-1: Invited Paper: Active Matrix Mini-LED Backlights for 1000PPI VR LCD," Dig. Tech. Pap.- Soc. Inf. Disp. Int. Symp. **50**, 562–565 (2019).

55. C. L. Yang, Y. H. Wu, I. A. Yao, Y. S. Tsou, C. H. Tsai, and J. S. Lin, "47-1: Invited Paper: High Resolution HDR VR display using Mini-LED," Dig. Tech. Pap.- Soc. Inf. Disp. Int. Symp. **52**, 636–639 (2021).

56. J. Zou, T. Zhan, E. L. Hsiang, X. Du, X. Yu, K. Li, and S. T. Wu, "Doubling the optical efficiency of VR systems with a directional backlight and a diffractive deflection film," Opt. Express **29**, 20673–20686 (2021).

57. J. A. LaRussa and A. T. Gill, "The Holographic Pancake Window TM," Visual Simulation and Image Realism I **0162**, 120–129 (1978).

58. Y. Li, T. X. Wu, and S. T. Wu, "Design optimization of reflective polarizers for LCD backlight recycling," J. Disp. Technol. **5**, 335–340 (2009).

59. L. Li and M. J. Escuti, "Super achromatic wide-angle quarter-wave plates using multi-twist retarders," Opt. Express **29**, 7464–7478 (2021).

60. Q. Hou, D. Cheng, Y. Li, T. Zhang, D. Li, Y. Huang, H. Chen, Q. Wang, W. Hou, and T. Yang, "Stray light analysis and suppression method of a pancake virtual reality head-mounted display," Opt. Express **30**, 44918–44932 (2022).

61. S. N. Maiti, U. K. Saroop, and A. Misra, "Studies on polyblends of poly(vinyl chloride) and acrylonitrile-butadiene-styrene terpolymer," Polym Eng. Sci. **32**, 27–35 (1992).

62. E. L. Hsiang, Y. Li, Z. He, T. Zhan, C. Zhang, Y. F. Lan, Y. Dong, and S. T. Wu, "Doubling the optical efficiency of color-converted micro-light-emitting diode displays with a patterned cholesteric liquid crystal polymer film," J. Soc. Info Disp. **29**, 288–297 (2021).

63. S. L. Lee, C. C. Cheng, C. J. Liu, C. N. Yeh, and Y. C. Lin, "9.4-inch 228-ppi flexible micro-LED display," J. Soc. Info Disp. **29**, 360–369 (2021).

64. J. Bae, Y. Shin, H. Yoo, Y. Choi, J. Lim, D. Jeon, I. Kim, M. Han, and S. Lee, "Quantum dot-integrated GaN light-emitting diodes with resolution beyond the retinal limit," Nat. Commun. **13**, 1862 (2022).

65. P. Delaporte and A. P. Alloncle, "Laser-induced forward transfer: A high resolution additive manufacturing technology," Optics & Laser Technology **78**, 33–41 (2016).

66. R. S. Cok, M. Meitl, R. Rotzoll, G. Melnik, A. Fecioru, A. J. Trindade, B. Raymond, S. Bonafede, D. Gomez, T. Moore, C. Prevatte, E. Radauscher, S. Goodwin, P. Hines, and C. A. Bower, "Inorganic light-emitting diode displays using micro-transfer printing," J. Soc. Info Disp. **25**, 589–609 (2017).

67. K. Ding, V. Avrutin, N. Izyumskaya, Ü. Özgür, and H. Morkoç, "Micro-LEDs, a Manufacturability Perspective," Appl. Sci. **9**, 1206 (2019).

68. L. Zhang, F. Ou, W. C. Chong, Y. Chen, and Q. Li, "Wafer-scale monolithic hybrid integration of Si-based IC and III–V epi-layers—A mass manufacturable approach for active matrix micro-LED micro-displays," J. Soc. Info Disp. **26**, 137–145 (2018).

69. K. L. Liang, W. H. Kuo, H. T. Shen, P. W. Yu, Y. H. Fang, and C. C. Lin, "Advances in color-converted micro-LED arrays," Jpn. J. Appl. Phys. **60**, SA0802 (2020).

70. Z. Liu, C. H. Lin, B. R. Hyun, C. W. Sher, Z. Lv, B. Luo, F. Jiang, T. Wu, C. H. Ho, H. C. Kuo, and J. H. He, "Micro-light-emitting diodes with quantum dots in display technology," Light Sci. Appl. **9**, 83 (2020).

71. T. Xuan, S. Shi, L. Wang, H. C. Kuo, and R. J. Xie, "Inkjet-Printed Quantum Dot Color Conversion Films for High-Resolution and Full-Color Micro Light-Emitting Diode Displays," J. Phys. Chem. Lett. **11**, 5184–5191 (2020).

72. Y. Yin, Z. Hu, M. U. Ali, M. Duan, L. Gao, M. Liu, W. Peng, J. Geng, S. Pan, Y. Wu, J. Hou, J. Fan, D. Li, X. Zhang, and H. Meng, "Full-Color Micro-LED Display with CsPbBr3 Perovskite and CdSe Quantum Dots as Color Conversion Layers," Adv. Mater. Technol. **5**, 2000251 (2020).

73. S. Han, F. D. Kiselev, and M. Mlejnek, "75-2: Quantum Dots on Color Filter LCD Design Study," Dig. Tech. Pap.- Soc. Inf. Disp. Int. Symp. **50**, 1067–1070 (2019).

74. C. J. Chen, C. C. Lin, J. Y. Lien, S. L. Wang, and R. K. Chiang, "Preparation of quantum dot/polymer light conversion films with alleviated Förster resonance energy transfer redshift," J. Mater. Chem. C **3**, 196–203 (2014).

75. F. Gou, E. L. Hsiang, G. Tan, Y. F. Lan, C. Y. Tsai, and S. T. Wu, "Tripling the Optical Efficiency of Color-Converted Micro-LED Displays with Funnel-Tube Array," Crystals **9**, 39 (2019).

76. S. W. H. Chen, Y. M. Huang, K. J. Singh, Y. C. Hsu, F. J. Liou, J. Song, J. Choi, P. T. Lee, C. C. Lin, and Z. Chen, "Full-color micro-LED display with high color stability using semipolar (20-21) InGaN LEDs and quantum-dot photoresist," Photonics Res. **8**, 630–636 (2020).

77. S. Y. Chu, H. Y. Wang, C. T. Lee, H. Y. Lee, K. L. Laing, W. H. Kuo, Y. H. Fang, and C. C. Lin, "Improved Color Purity of Monolithic Full Color Micro-LEDs Using Distributed Bragg Reflector and Blue Light Absorption Material," Coatings **10**, 436 (2020).

78. J. Y. Lien, C. J. Chen, R. K. Chiang, and S. L. Wang, "39-3: Patternable Color-conversion Films based on Thick-shell Quantum Dots," Dig. Tech. Pap.- Soc. Inf. Disp. Int. Symp. **48**, 558–561 (2017).

79. J. He, Z. He, A. Towers, T. Zhan, H. Chen, L. Zhou, C. Zhang, R. Chen, T. Sun, A. J. Gesquiere, S. T. Wu, and Y. Dong, "Ligand assisted swelling–deswelling microencapsulation (LASDM) for stable, color tunable perovskite–polymer composites," Nanoscale Adv. **2**, 2034–2043 (2020).

80. H. M. Kim, M. Ryu, J. H. J. Cha, H. S. Kim, T. Jeong, and J. Jang, "Ten micrometer pixel, quantum dots color conversion layer for high resolution and full color active matrix micro-LED display," J. Soc. Info Disp. **27**, 347–353 (2019).

81. Y. Huang, T. X. Wu, and S. T. Wu, "Simulations of liquid-crystal Fabry–Perot etalons by an improved 4×4 matrix method," J. Appl. Phys. **93**, 2490–2495 (2003).

82. M. R. Krames, O. B. Shchekin, R. Mueller-Mach, G. O. Mueller, L. Zhou, G. Harbers, and M. G. Craford, "Status and Future of High-Power Light-Emitting Diodes for Solid-State Lighting," J. Disp. Technol. **3**, 160–175 (2007).

83. P. Zhao and H. Zhao, "Analysis of light extraction efficiency enhancement for thin-film-flip-chip InGaN quantum wells light-emitting diodes with GaN micro-domes," Opt. Express **20**, A765–A776 (2012).

84. X. Chen, C. Ji, Y. Xiang, X. Kang, B. Shen, and T. Yu, "Angular distribution of polarized light and its effect on light extraction efficiency in AlGaN deep-ultraviolet light-emitting diodes," Opt. Express **24**, A935–A942 (2016).

85. Y. C. Shen, J. J. Wierer, M. R. Krames, M. J. Ludowise, M. S. Misra, F. Ahmed, A. Y. Kim, G. O. Mueller, J. C. Bhat, S. A. Stockman, and P. S. Martin, "Optical cavity effects in InGaN/GaN quantum-well-heterostructure flip-chip light-emitting diodes," Appl. Phys. Lett. **82**, 2221–2223 (2003).

86. Z. Hu, Y. Yin, M. Umair Ali, W. Peng, S. Zhang, D. Li, T. Zou, Y. Li, S. Jiao, S. jhih Chen, C. Y. Lee, H. Meng, and H. Zhou, "Inkjet printed uniform quantum dots as color conversion layers for full-color OLED displays," Nanoscale **12**, 2103–2110 (2020).

87. Z. He, J. He, C. Zhang, S. T. Wu, and Y. Dong, "Swelling-Deswelling Microencapsulation-Enabled Ultrastable Perovskite−Polymer Composites for Photonic Applications," Chem. Rec. **20**, 672–681 (2020).

88. Y. T. Chen, S. W. Wen, P. H. Liao, W. K. Lee, C. C. Lee, C. W. Huang, Y. H. Yang, K. C. Lin, C. J. Chang, G. D. Su, H. Y. Lin, C. C. Chen, W. Y. Lin, B. L. Kwak, R. J. Visser, and C. C. Wu, "Reflective 3D pixel configuration for enhancing efficiency of OLED displays," Organic Electronics **103**, 106451 (2022).

89. A. R. Anwar, M. T. Sajjad, M. A. Johar, C. A. Hernández-Gutiérrez, M. Usman, and S. P. Łepkowski, "Recent Progress in Micro-LED-Based Display Technologies," Laser Photonics Rev. **16**, 2100427 (2022).

90. Y. M. Huang, J. H. Chen, Y. H. Liou, K. James Singh, W. C. Tsai, J. Han, C. J. Lin, T. S. Kao, C. C. Lin, S. C. Chen, and H. C. Kuo, "High-Uniform and High-Efficient Color Conversion Nanoporous GaN-Based Micro-LED Display with Embedded Quantum Dots," Nanomaterials **11**, 2696 (2021).

91. B. R. Hyun, C. W. Sher, Y. W. Chang, Y. Lin, Z. Liu, and H. C. Kuo, "Dual Role of Quantum Dots as Color Conversion Layer and Suppression of Input Light for Full-Color Micro-LED Displays," J. Phys. Chem. Lett. **12**, 6946–6954 (2021).

92. Y. H. Wu, C. C. Chang, Y. S. Tsou, Y. C. Lo, C. H. Tsai, C. hung Lu, C. L. Yang, and F. M. Chuang, "70-3: Invited Paper: High-Resolution Light-Field VR LCD," Dig. Tech. Pap.- Soc. Inf. Disp. Int. Symp. **53**, 945–948 (2022).

93. T. Zhan, E. L. Hsiang, K. Li, and S. T. Wu, "Enhancing the Optical Efficiency of Near-Eye Displays with Liquid Crystal Optics," Crystals **11**, 107 (2021).

94. K. D. Chang, C. Y. Li, J. W. Pan, and K. Y. Cheng, "A hybrid simulated method for analyzing the optical efficiency of a head-mounted display with a quasi-crystal OLED panel," Opt. Express **22**, A567–A576 (2014).

95. Y. Gao, Z. Luo, R. Zhu, Q. Hong, S. T. Wu, M. C. Li, S. L. Lee, and W. C. Tsai, "A High Performance Single-Domain LCD With Wide Luminance Distribution," J. Disp. Technol. **11**, 315–324 (2015).

96. K. Käläntär, "A directional backlight with narrow angular luminance distribution for widening the viewing angle for an LCD with a front-surface light-scattering film," J. Soc. Info Disp. **20**, 133–142 (2012).

97. M. Mon-Williams, J. P. Warm, and S. Rushton, "Binocular vision in a virtual world: visual deficits following the wearing of a head-mounted display," Ophthalmic Physiol Opt. **13**, 387–391 (1993).

98. J. Rouf Talukder, Y. Huang, and S. T. Wu, "High performance LCD for augmented reality and virtual reality displays," Liq. Cryst. **46**, 920–929 (2019).

99. T. Matsushima, S. Kimura, and S. Komura, "Fast response in-plane switching liquid crystal display mode optimized for high-resolution virtual-reality head-mounted display," J. Soc. Info Disp. **29**, 221–229 (2021).

100. X. Zhu, Z. Ge, and S. T. Wu, "Analytical solutions for uniaxial-film-compensated wide-view liquid crystal displays," J. Disp. Technol. **2**, 2–20 (2006).

101. G. Tan, J. H. Lee, S. C. Lin, R. Zhu, S. H. Choi, and S. T. Wu, "Analysis and optimization on the angular color shift of RGB OLED displays," Opt. Express **25**, 33629–33642 (2017).

102. M. Thomschke, R. Nitsche, M. Furno, and K. Leo, "Optimized efficiency and angular emission characteristics of white top-emitting organic electroluminescent diodes," Appl. Phys. Lett. **94**, 083303 (2009).

103. S. K. Kim, M. J. Park, R. Pode, and J. H. Kwon, "A Deep Blue Strong Microcavity Organic Light-Emitting Diode Optimized by a Low Absorption Semitransparent Cathode and a Narrow Bandwidth Emitter," Adv. Photonics Res. **2**, 2000122 (2021).